Tropospheric Ozone Precursors: Global and Regional Distributions, Trends, and Variability

Yasin Elshorbany[1*], Jerald R. Ziemke[2], Sarah Strode[2,3], Hervé Petetin[4], Kazuyuki Miyazaki[5], Isabelle De Smedt[6], Kenneth Pickering[7], Rodrigo J. Seguel[8], Helen Worden[9], Tamara Emmerichs[10], Domenico Taraborrelli[10], Maria Cazorla[11], Suvarna Fadnavis[12], Rebecca R. Buchholz[9], Benjamin Gaubert[9], Néstor Y. Rojas[13], Thiago Nogueira[14], Thérèse Salameh[15], Min Huang[16]

[*]Correspondence to: elshorbany@usf.edu

[1] School of Geosciences, College of Arts and Sciences, University of South Florida, St. Petersburg, FL, USA

[2] NASA Goddard Space Flight Center, Greenbelt, Maryland, USA

[3] Goddard Earth Sciences Technology and Research (GESTAR II), Maryland, USA

[4] Earth Sciences Department, Barcelona Supercomputing Center, Barcelona, Spain

[5] Jet Propulsion Laboratory, California Institute of Technology, Pasadena CA

[6] BIRA-IASB, Ringlaan 3 Av. Circulaire, 1180 Brussels, Belgium

[7] Dept. of Atmospheric and Oceanic Science, University of Maryland, College Park, MD USA

[8] Center for Climate and Resilience Research, Department of Geophysics, Faculty of Physical and Mathematical Sciences University of Chile, Chile.

[9] Atmospheric Chemistry Observations and Modeling (ACOM), National Center for Atmospheric Research (NCAR), Boulder CO, USA.

[10] Institute of Energy and Climate Research, IEK-8: Troposphere, Forschungszentrum Jülich, Jülich, Germany.

[11] Universidad San Francisco de Quito USFQ, Instituto de Investigaciones Atmosféricas, Diego de Robles y Av Interoceánica, Quito, Ecuador.

[12] Center for Climate Change Research, Indian Institute of Tropical Meteorology, MoES, Pune, India.

[13] Department of Chemical and Environmental Engineering, Universidad Nacional de Colombia, Bogota, Colombia.

[14] University of São Paulo, São Paulo, Brazil.

[15] IMT Nord Europe, Institut Mines-Télécom, Univ. Lille, Centre for Energy and Environment, 59000, Lille, France.

[16] Earth System Science Interdisciplinary Center, University of Maryland, College Park, MD, USA.

Abstract

Tropospheric ozone results from in-situ chemical formation and stratosphere-troposphere exchange (STE), with the latter being more important in the middle and upper troposphere than in the lower troposphere. Ozone photochemical formation is nonlinear, and results from the oxidation of methane and non-methane hydrocarbons (NMHCs) in the presence of nitrogen oxide (NO_x=NO+NO_2). Previous studies showed that O_3 short- and long-term trends are nonlinearly controlled by near-surface anthropogenic emissions of carbon monoxide (CO), volatile organic compounds (VOCs), and nitrogen oxides, which maybe also impacted by the long-range transport (LRT) of O_3 and its precursors. In addition, several studies have demonstrated the important role of STE in enhancing ozone levels, especially in the midlatitudes. In this article, we investigate tropospheric ozone spatial variability and trends from 2005 to 2019 and relate those to ozone precursors on global and regional scales. We also investigate the spatiotemporal characteristics of the ozone formation regime in relation to ozone chemical sources and sinks. Our analysis is based on remote sensing products of the Tropospheric Column of Ozone (TrC-O_3) and its precursors, nitrogen dioxide (TrC-NO_2), formaldehyde (TrC-HCHO), and total column of CO (TC-CO) as well as ozonesonde data and model simulations. Our results indicate a complex relationship between tropospheric ozone column levels, surface ozone levels, and ozone precursors. While the increasing trends of near-surface ozone concentrations can largely be explained by variations in VOC and NO_x concentration under different regimes, TrC-O_3 may also be affected by other variables such as tropopause height and STE as well as LRT. Decreasing or increasing trends in TrC-NO_2 have varying effects on the TrC-O_3, which is related to the different local chemistry in each region. We also shed light on the contribution of NO_x lightning and soil NO and nitrous acid (HONO) emissions to trends of tropospheric ozone on regional and global scales.

1. Introduction

Tropospheric ozone (O_3) is an important air pollutant due to its diverse effects on air quality, ecosystem (Mills et al., 2018), health (Lefohn et al., 2018; Fleming et al., 2018), and climate (Boucher et al., 2013; Myhre et al., 2013; Zanis et al., 2022). O_3 is a photochemical product that results from the oxidation of methane (CH_4) and non-methane hydrocarbons (NMHCs) in the presence of nitrogen oxides (NO_x). Tropospheric ozone burdens can also be affected by stratosphere-troposphere exchange (STE) (Stohl et al., 2003; Zeng et al., 2010; Trickl et al., 2011; Li et al., 2024) and long-range transport (LRT) of ozone (e.g., Hov et al., 1978; Ravetta et al., 2007; Itahashi et al., 2020). O_3 is considered a short-lived climate forcer (SLCF) and is the third-most important greenhouse gas with an effective radiative forcing of ($0.47^{+0.23}_{-0.23}$) W m^{-2}; Forster et al., 2021). Since the mid-1990s, free tropospheric ozone trends based on in situ measurement and satellite retrievals have increased with high confidence (HC) by 1-4 nmol mol^{-1} $decade^{-1}$ across the northern mid-latitudes and 1-5 nmol mol^{-1} $decade^{-1}$ within the tropics (Gulev et al., 2021). In the Southern Hemisphere, with more limited observation coverage compared with the Northern Hemisphere, the tropospheric column ozone shows an increase since the mid-1990s by less than 1 nmol mol^{-1} $decade^{-1}$ with medium confidence at southern mid-latitudes (Gulev et al., 2021, Cooper at al., 2020). Tropospheric O_3 short- and long-term trends are nonlinearly controlled by anthropogenic emissions of carbon monoxide (CO), volatile organic compounds (VOCs), and nitrogen oxides ($NO_x=NO+NO_2$) as well as STE, especially in the midlatitudes (Li et al., 2024). Meteorological parameters such as wind speed and wind direction may also enhance the LRT of O_3, affecting regional ozone burdens, especially in the free troposphere (e.g., Glotfelty et al, 2014; Itahashi et al., 2020). Methane, with an assessed total atmospheric lifetime of 9.1 ± 0.9 years (Szopa et al., 2021), is also a crucial driver of tropospheric ozone (Fiore et al., 2002; Isaksen et al., 2014). Its accelerated growth rate of 7.6 ± 2.7 nmol mol^{-1} yr^{-1} between 2010 and 2019 (Canadell et al., 2021) is largely driven by anthropogenic activities (Szopa et al., 2021). NOAA GML observations of methane (NOAA, 2024) show that methane concentrations in the atmosphere have increased sharply since 2005 (an 8% increase from 2005 to 2023). Future scenarios show that emission control measures can influence future changes to air pollutants. Although the global increases in CH_4 abundance may offset benefits to surface O_3 from local emission reductions (Fiore et al., 2002; Shindell et al., 2012; Wild et al., 2012; Szopa et al., 2021), recent reports (e.g., Itahashi et al., 2020; Zanis et al., 2022), showed the dominant role of precursor emission changes in projecting surface ozone concentrations under future climate change scenarios. In this study, we investigate the relation between ozone trends and the trends of its precursors, with a focus on NO_2, CO, and HCHO.

Coupled Model Intercomparison Project Phase 6 (CMIP6) overestimates observed surface O_3 concentrations in most regions, with larger variability over Northern Hemisphere (NH) continental regions (e.g., Tarasick et al., 2019; Turnock et al., 2020). CMIP6 models simulate large increasing trends of surface concentrations of O_3 and $PM_{2.5}$ in East and South Asia with an annual mean increase of up to 40 ppb and 12 μgm^{-3}, respectively, over the historical periods (1850-2014; Turnock et al., 2020). However, these studies found also that CMIP6 models consistently underestimate $PM_{2.5}$ concentrations in the NH, especially during the winter months, and with larger variability near natural source regions, indicating missing sources (e.g., HONO) of O_3 (e.g., Elshorbany et al., 2014).

Satellite observations have the advantage of large spatial and consistent temporal coverage. Tropospheric columns of ozone (TrC-O_3), in Dobson unit (1 DU=2.69×10^{20} molecules m^{-2}),

are usually used to represent tropospheric ozone levels. The tropospheric column of a species is the species' concentration integrated from the surface to the top of the troposphere, the tropopause. The tropopause height is dynamically changing, and it varies over time, increasing or decreasing as a function of several factors, including tropospheric and stratospheric temperature (warming or cooling). Steinbrecht et al (1998) found that observed tropospheric warming of 0.7 ± 0.3 K per decade leads to an increase in the tropopause high and a decrease (at a rate of 16 DU/decade) in the observed column ozone levels. Similarly, after removing the variations related to major natural forcings, including volcanic eruptions, ENSO (El Niño–Southern Oscillation), and QBO (Quasi–Biennial Oscillation), Meng et al. (2021) concluded that a continuous rise of the tropopause in the Northern Hemisphere (NH) from 1980 to 2020 is evident, which they related mainly to tropospheric warming caused by anthropogenic emissions. Steinbrecht et al (1998) and Meng et al. (2021) calculate the same rate of tropopause increase for the periods 1980-2000 and 1980-2020, respectively. We investigate the trends in TrC-O_3 and ozone precursors at different column depths and determine their relationships.

Global models play a vital role in interpreting the observed trends in ozone precursors, verifying the consistency of emission inventories with observed precursor concentrations, and relating trends in ozone precursor emissions to ozone trends. Because satellite measurements are often sensitive to species concentrations above the surface, models provide additional information on the vertical distribution of ozone precursors needed to relate emissions or surface trends to a column or free tropospheric observations. For example, chemical transport models are used to relate Ozone Monitoring Instrument (OMI) NO_2 columns to surface NO_2 concentrations and their trends over the United States (e.g. Lamsal et al 2008, 2015; Kharol et al, 2015) since they provide vertical information on the NO_2 distribution. Models are also used to infer NO_x emission trends from observations (e.g. Richter et al., 2005; Stavrakou et al., 2008; Miyazaki et al, 2016) or to examine whether simulations driven by state-of-the-art emissions inventories can reproduce observed changes in NO_x (Itahashi et al., 2014; Godowitch et al, 2010). Models also provide insight into the role of background NO_2 versus local sources in relating satellite-observed NO_2 columns to NO_x emissions changes (Silvern et al, 2019). Similarly, global models are vital for understanding trends in CO, since the lifetime of CO allows both local emissions and long-range transport and the global background to influence regional trends of CO and O_3. Duncan and Logan (2008) attributed the decreasing CO in the NH from 1998-1997 to decreasing European emissions and highlighted the role of Indonesian fires in driving interannual variability. Numerical models can also be used to assimilate satellite CO observations to invert for CO emission fluxes, often highlighting differences between bottom-up and top-down inventories (e.g., Kopacz et al., 2010; Fortems-Cheiney et al., 2011; Elguindi et al., 2020; Gaubert et al., 2020). For instance, several modeling studies found that the increasing emissions from China in recent years in some emission inventories were inconsistent with the negative trends observed by MOPITT (Yin et al, 2015; Strode et al., 2016; Zheng et al, 2019), while the decreases over the United States and Europe are supported by the observed decrease in CO. Jiang et al (2017) and Zheng et al (2019) also found that a decrease in biomass burning contributes to the negative CO trend in the NH. Mean calculated O_3 burden using CMIP6 simulation (Griffiths et al, 2021) revealed an increase of 44% from 1850 to the mean of the period of 2005-2014 and by another 17% until 2100 using the SSP370 experiments. Other sources of NO_x such as lightning and soil emissions play an important role in controlling the O_3 budget, especially in low-NO_x regions. We investigate these sources and the role they play in determining O_3 trends and variability on regional and global scales, as well as their determining factors.

153   Previous literature demonstrates the importance of controlling the emissions of ozone
154   precursors to effectively reduce surface O_3 levels. Therefore, a thorough and rigorous
155   understanding of the trends and variability for O_3 precursors is of paramount importance for a
156   global abatement strategy of O_3 levels. In this study, we use ozonesonde, remote sensing, and
157   global models to evaluate tropospheric O_3 and O_3 precursor trends of CO, HCHO, and NO_2,
158   on regional and global scales.

159   **2.   Methodology**

160   **2.1. Trend Analysis**

161   We analyze the historical trends of tropospheric ozone and its precursors CO, NO_2, and HCHO,
162   from 2005 to 2019. For trend analysis, we use two methods, the Quantile regression (QR)
163   method (Chang et al., 2023), and the Weighted Least Squares (WLS). For NO_2, CO, and HCHO
164   trends are calculated based on the QR method (Chang et al., 2023), as follows: (1) we first
165   compute the deseasonalized monthly time series of NO_2 and HCHO tropospheric columns
166   (hereafter referred to as TrC-NO_2, TrC-HCHO), and CO atmospheric column (TC_CO), (2) we
167   use the quantile regression method for computing the trend, focusing here on the median, and (3)
168   uncertainties at a 95% confidence level are estimated using the block bootstrapping approach,
169   through 1000 iterations with blocks size of $N^{0.25}$ with N the number of monthly values. They are
170   calculated over a 1°x1° grid and only in cells where at least 75% of the monthly values are
171   available. TC_CO column (see sec. 2.2.1) time series trends are also calculated as Weighted
172   Least Squares (WLS) of the monthly anomaly, weighted by the monthly regional standard
173   deviation (for comparison with the QR method). The tropospheric ozone column (TrC-O_3),
174   trends are calculated based on the WLS method. Tropospheric columns of satellite observations
175   are calculated based on the WMO thermal definition of the tropopause. To account for varying
176   tropospheric column definitions used in previous literature, we also evaluate the trends at varying
177   column depths.

178   **2.2. Data resources**

179   In this section, we present the different data repositories and their characteristics.

180   **2.2.1.   Satellite data**

181   A list of the applied satellite data products and their resolution is shown in Table 1. For
182   Tropospheric ozone data, we use the Ozone Monitoring Instrument/Microwave Limb Sounder
183   (OMI/MLS) product (Ziemke et al., 2006). The OMI/MLS product is the residual of the OMI total
184   ozone column and the MLS stratospheric ozone column, available as gridded monthly means. The
185   OMI/MLS tropospheric column ozone product applies all necessary data quality flags to both OMI
186   total ozone and MLS profile ozone; the OMI/MLS product further includes cloud filtering by
187   omitting all scenes with OMI reflectivity greater than 0.30. The tropospheric NO_2 column
188   retrievals used were the QA4ECV project (http://www.qa4ecv.eu/ecvs) version 1.1 level 2 (L2)
189   product for OMI (Boersma et al., 2017a), GOME-2 (Boersma et al., 2017b), and SCIAMACHY
190   (Boersma et al., 2017c). The ground pixel sizes of the OMI, GOME-2, and SCIAMACHY
191   retrievals are 13 km×24 km, 80 km×40 km, and 60 km×30 km, with local Equator overpass times
192   of 13:45, 09:30, and 10:00 LT, respectively. We also use HCHO tropospheric columns retrieved
193   from OMI (De Smedt et al. 2018) from the QA4ECV project. Atmospheric total column CO
194   daytime observations were obtained from the MOPITT instrument aboard the Terra Satellite
195   (Barret et al., 2003; Buchholz et al., 2017). Monthly daytime L3 data were obtained at 1º gridded
196   horizontal resolution from the NASA Langley Research Center Atmospheric Science Data Center

197 (ASDC, 2024), using version 9 (V9) retrievals, and the joint near-infrared/thermal-infrared product
198 (Deeter et al., 2022). Low-quality data were excluded by applying the provided quality flag.

199

200 Table 1 Satellite data products and their reference periods.

Parameter	Resolution (Satellite pixel size)	Instrument/Platform	Reference Period	Reference
NO$_2$	1°x1° (13 km x 24 km)	OMI/Aura	2005–2020	Boersma et al., 2017a
NO$_2$	1°x1° (40 km x 80 km)	GOME-2/METOP-A	2007–2018	Boersma et al., 2017b
NO$_2$	1°x1° (30 km x 60 km)	SCIAMACHY/ENVISAT	2005–2011	Boersma et al., 2017c
CO	1°x1° (22 km x 22 km)	MOPITT/TERRA	2002–2020	Deeter et al., 2022
HCHO	1°x1° (13 km x 24 km)	OMI/Aura	2004–2020	De Smedt et al., 2018
Ozone	1°x1°	OMI/MLS	2004–2020	Ziemke et al., 2006

201

2.2.2.   Ozonesonde Data

203 Direct sampling of ozone throughout the atmospheric column by ozonesondes on board of high-
204 altitude balloons is a primary source of information of the ozone abundance and changes in the
205 free troposphere. Ozonesonde data have been used extensively for satellite ozone product
206 validations, trend analyses, and as a priori climatology profiles for satellite retrieval algorithms
207 (McPeters and Labow, 2012; Labow et al., 2015; Hubert et al., 2021; Christiansen et al., 2022;
208 Newton et al., 2016). Ozonesondes networks around the globe have been providing the ozone
209 community with accurate in situ measurements of high vertical resolution (100-m) for the last 5
210 decades in the Northern Hemisphere (Krizan and Lastovicka, 2005), nearing 3 decades at
211 stations in the tropics (Thompson et al., 2017), and in the last decade, new efforts are
212 contributing with data from undersampled regions such as the tropical Andes (Cazorla and
213 Herrera, 2022). Other important contributions include dedicated campaigns for regional studies
214 (e.g. Newton et al., 2016; Fadnavis et al., 2023). Figure 1 shows a map with ozonesonde stations
215 around the globe whose data are publicly available from data providers (station names,
216 coordinates, and links for data access in the Supplementary Material, Table S1). In this work, we

217 present a review of ozonesonde trends calculated and published in previous studies (Wang et al.,
218 2022 and Christiansen et al., 2022).

219
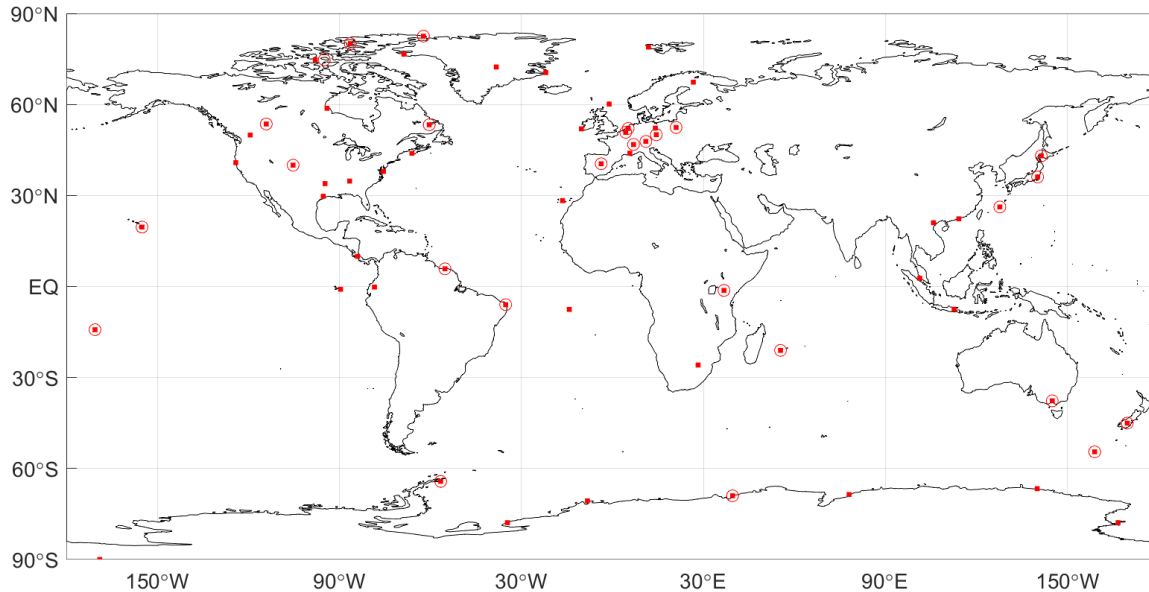
220

221 Figure 1: Ozone-sounding stations around the globe (red squares) whose data are publicly
222 available (Table S1). Stations that meet the criteria to calculate trends (Wang et al., 2022) are
223 circled in red.

224

225 2.2.3. Model simulations of ozone precursors and their vertical distribution

226 Model simulations provide information on the vertical distribution of trace gases that can help
227 interpret the observed columns. Here, we use a Goddard Earth Observing System (GEOS) Earth
228 System Model (Molod et al, 2015) simulation run with the GMI chemistry mechanism (Duncan
229 et al, 2007; Strahan et al, 2007; Nielsen et al, 2017) to simulate the contributions of the lower,
230 middle, and upper troposphere to the tropospheric columns of ozone and its precursors. The
231 model configuration is described in Fisher et al (2024) and summarized here. The MERRA-2
232 reanalysis (Gelaro et al., 2017) constrains the GEOS-GMI meteorology. The GEOS-GMI
233 meteorology is replayed to the MERRA-2 meteorology as described in Orbe et al (2017).
234 Anthropogenic emissions of NO_2, CO, and VOCs are based on the MACCity inventory (Granier
235 et al, 2011) through 2010 and the RCP8.5 emissions afterward, with NO_2 emissions scaled based
236 on OMI. The emissions are downscaled to higher resolution using the EDGAR 4.2 emission
237 inventory (Janssens-Maenhout et al., 2013). Biomass burning emissions for the analysis period
238 come from the Fire Energetics and Emissions Research (FEER) product (Ichoku and Ellison,
239 2014). Liu et al (2022) evaluated another GEOS simulation with GMI chemistry with satellite
240 observations of $TrC-O_3$, $TrC-NO_2$, $TrC-HCHO$, and TC-CO.

241 3. Data Analysis and Discussion

242 3.1. $TrC-O_3$ Sensitivity to Tropopause

243 Calculated $TrC-O_3$ depends on several factors such as tropospheric ozone levels, atmospheric
244 warming (e.g., due to GHG emissions) or cooling (stratospheric or tropospheric (e.g., after major
245 volcanic eruptions), and tropopause height (TH). Atmospheric warming or cooling can lead to a

246 decrease or an increase, respectively, of TrC-O_3 due to the respective change in the TH. Several
247 methods are used to determine the TH. The WMO thermal definition for the first TH, the lowest
248 altitude level at which the lapse rate decreases to 2º K km⁻¹ or less, provided that the average
249 lapse rate between this level and all higher levels within 2 km does not exceed 2º K km⁻¹. A
250 second tropopause may be also found if the lapse rate above the first tropopause exceeds 3°K
251 km⁻¹ (WMO, 1992; Hoffmann and Spang (2022). Other studies define the TH based on fixed
252 pressure levels (from ground to 150, 200, 300, and 400 hPa). Mean OMI/MLS TrC-O_3 values in
253 July (2005-2019) calculated based on the WMO thermal definition, are shown in Figure 2. TrC-
254 O_3 values are comparable to previously reported CMIP6 and satellite measurements (Griffiths et
255 al., 2021). Partial ozone columns (OC) calculated from the ground to different pressure levels,
256 150, 200, and 300 hPa show increasing OC values with increasing column depth, with calculated
257 OC at 150 and 200 hPa being the closest to the TrC-O_3 WMO values, still overestimating OC in
258 the northern hemisphere (50-90º N), especially for the 150 hPa OC, see Figure 2.

259
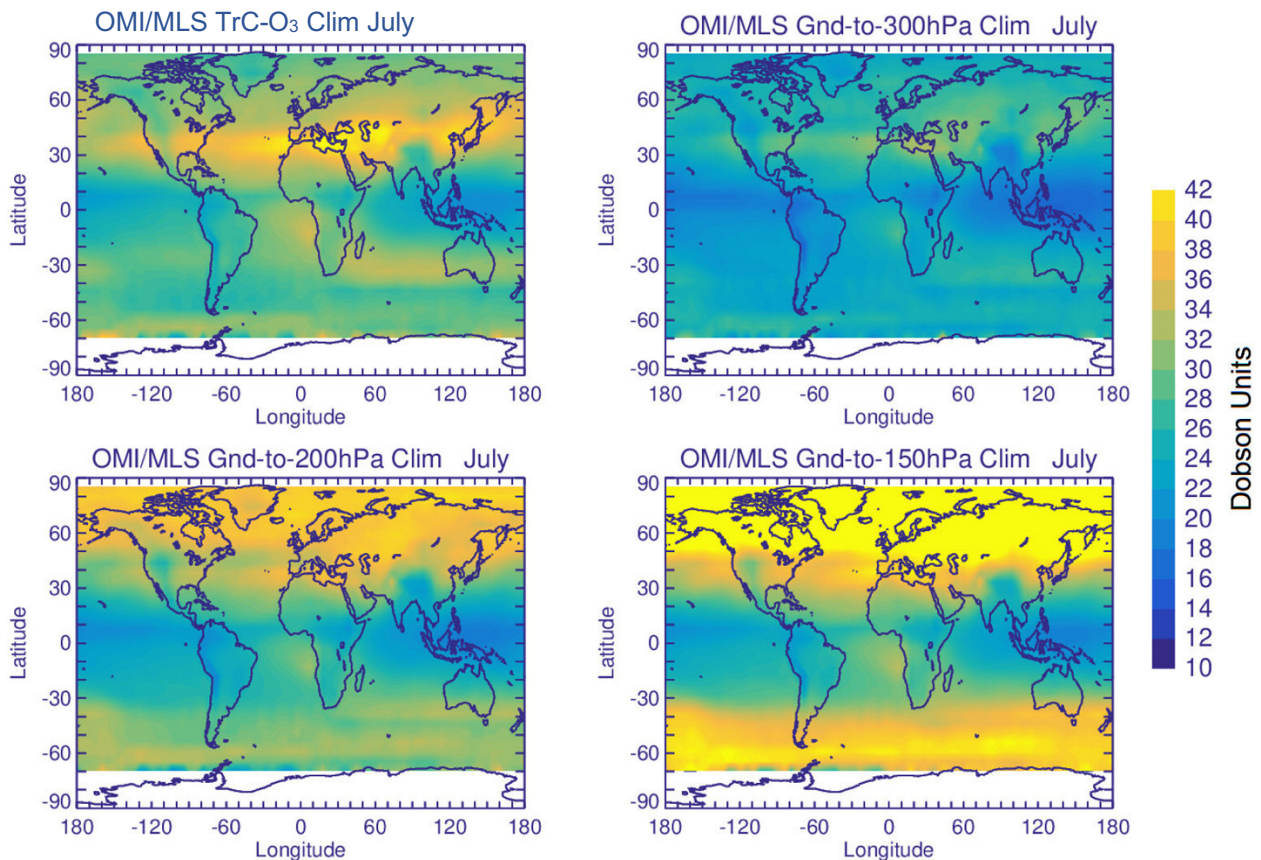
261 Figure 2: Global Mean (2005-2019) Column Ozone based on the WMO definition, and for
262 different column depths.

263

264 Steinbrecht et al (1998) found that observed tropospheric warming of 0.7± 0.3 K per decade
265 leads to an increase in the TH and a decrease in total ozone. They also calculated a decrease of
266 16 DU per kilometer increase in TH. These results indicate the importance of TH on calculated
267 long-term ozone trends. This could also affect comparisons between trends calculated based on
268 different TrC-O_3 definitions and near-surface ozone levels. The time series of deseasonalized TH
269 from 2004 to 2021 are shown in Figure 3 together with their zonal mean trends. Trends in TH are

270 positive reaching 60 meters/decade except in a narrow band in the tropics from 10ºS to 20ºN and
271 at 30ºS, where TH decreases at a rate up to 30 meters/decade. TH in the tropical regions is also
272 characterized by high variability (see Figure 3). These results are also consistent with recent
273 reports showing a positive trend of TH from 20-80ºN at a rate of 50-60 m/decade (Meng et al.,
274 2021). They related this increase primarily to tropospheric warming. These results show that
275 using a fixed pressure level for the tropopause may not be accurate given the change in TH over
276 time. In the following sections, tropospheric columns will be calculated based on the WMO
277 tropopause definition.

278
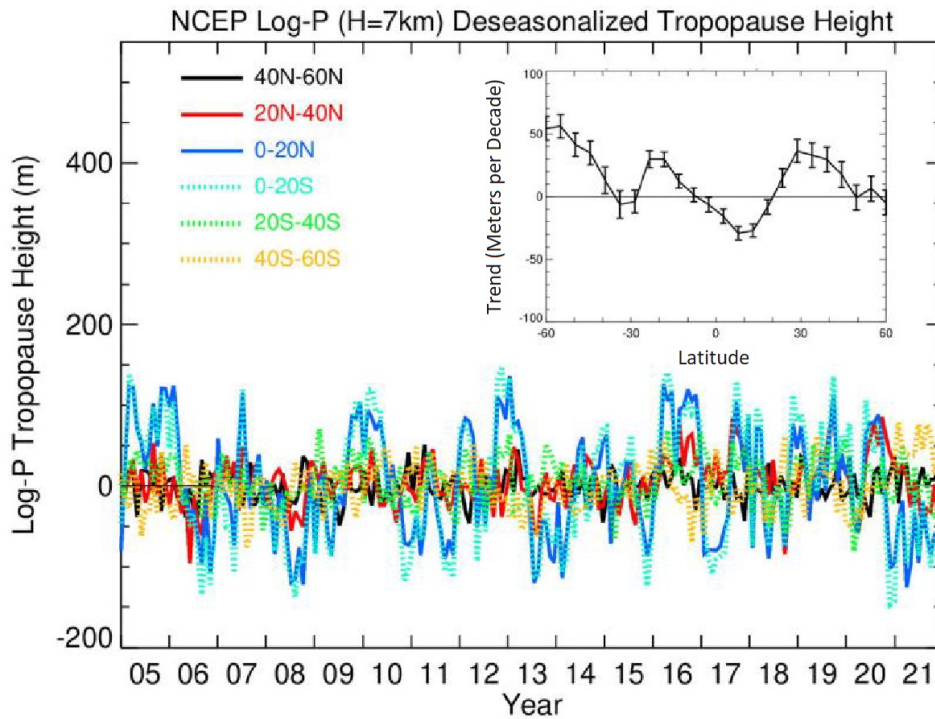
279

280 Figure 3: National Centers for Environmental Prediction (NCEP) WMO (2K/km) tropopause
281 log-P height time series with trends (meters/decade) embedded.

282

283   **3.2. Spatial Distribution of O$_3$ and its Precursors**

284 Tropospheric O$_3$ results from in-situ photochemical formation and STE. In-situ O$_3$ results from
285 the photolysis of NO$_2$. Therefore, the sources and fate of NO$_2$ in the atmosphere determine O$_3$
286 burden and distribution. NO$_2$ is formed from the reaction of hydrogen peroxyl (HO$_2$) and alkyl
287 peroxyl (RO$_2$) radicals with NO (R 3.2-1). While photolysis of NO$_2$ is the main source of ozone,
288 high NO$_2$ levels can suppress O$_3$ levels as NO$_2$ reacts with OH radical forming HNO$_3$ (R 3.2-2 to
289 R 3.2-4), thus reducing the oxidation rate of hydrocarbons and respectively HO$_2$ and RO$_2$ levels,
290 leading to a net loss of O$_3$ (e.g., Finlayson-Pitts and Pitts, 2000; Elshorbany et al., 2010,
291 Archibald et al., 2020). Ozone production efficiency is calculated as the ratio of the number of
292 NO$_2$ molecules photolyzed to form O$_3$ to that lost due to the reaction with OH forming HNO$_3$.
293 Under NO-sensitive conditions, the decrease in NO$_x$ leads to a reduction in OH, HCHO, and O$_3$.
294 However, under high NO conditions, a reduction in NO$_x$ could lead to an increase in
295 photochemical products, OH, HCHO, and O$_3$ because a reduction in NO$_2$ leads to a decrease in

296   OH loss rate, thus higher HO_2 and RO_2 production (Elshorbany et al., 2012; Archibald et al.,
297   2020).

298   R 3.2-1 HO_2/RO_2 +   NO   → NO_2

299   R 3.2-2 NO_2 +   hν (hν < 424 nm)   → $O(^3P)$ +   NO

300   R 3.2-3 $O(^3P)$ + O_2 +   M   → O_3 +   M

301   R 3.2-4   OH   + NO_2 (M)   → HNO_3 (M)
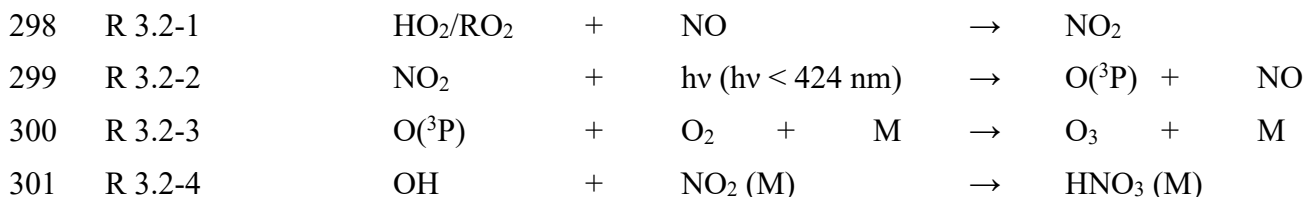
302

303   The observed mean tropospheric columns of O_3, NO_2, and HCHO and atmospheric column of
304   CO from 2005 to 2019 are shown in Figure 4. The unit for column number density is
305   Pmolec/cm^2 (×10^{15} molecules per square centimeter), except for TrC-O_3, which is Dobson. NO_2
306   concentration has decreased since 2005 in North America, Europe, and Australia, mainly due to
307   strict measures to reduce air pollution (Lamsal et al., 2015). Since O_3 is a photochemical product
308   that is formed based on non-linear chemistry, a reduction in NO_2 may lead to an increase or
309   decrease in tropospheric O_3 levels based on the dominant photochemical regime in the respective
310   region. In addition, tropospheric ozone levels may be affected by STE especially in the middle
311   and upper troposphere (Li et al., 2024), as well as LRT, especially in the free troposphere (e.g.,
312   Glotfelty et al, 2014; Itahashi et al., 2020). The highest values of the NO_2 tropospheric column
313   are in the northern hemisphere between 10 ºN and 50ºN, especially over the eastern US, northern
314   Europe, and east and south Asia, with elevated levels in the Southern Hemisphere (SH) between
315   10 and 30ºS, especially in sub-Saharan Africa, and Brazil. TrC-O_3 is also highest over the band
316   of 20-50º N, especially over the eastern coast of the US, southern Europe, and east Asia. Some
317   differences exist between TrC-O_3 and TrC-NO_2 spatial patterns which is due to factors including
318   different lifetime, photochemical sensitivity (see sec. 3.4), and STE. On average, the northern
319   hemisphere has higher TC-CO than the southern hemisphere due to a larger number of sources
320   (Buchholz et al., 2021). Additionally, high amounts of CO are found in regions with large
321   anthropogenic sources (e.g., eastern China) or in regions with large and regular fire seasons (e.g.,
322   central Africa) (Buchholz et al., 2021). HCHO and CO show a similar spatial pattern over
323   western Africa due to emissions from biomass burning (Marais et al., 2012, Buchholz et al.,
324   2021). In the following sections, global and regional trends of TrC-O_3 are investigated along
325   with tropospheric ozone precursors.

326
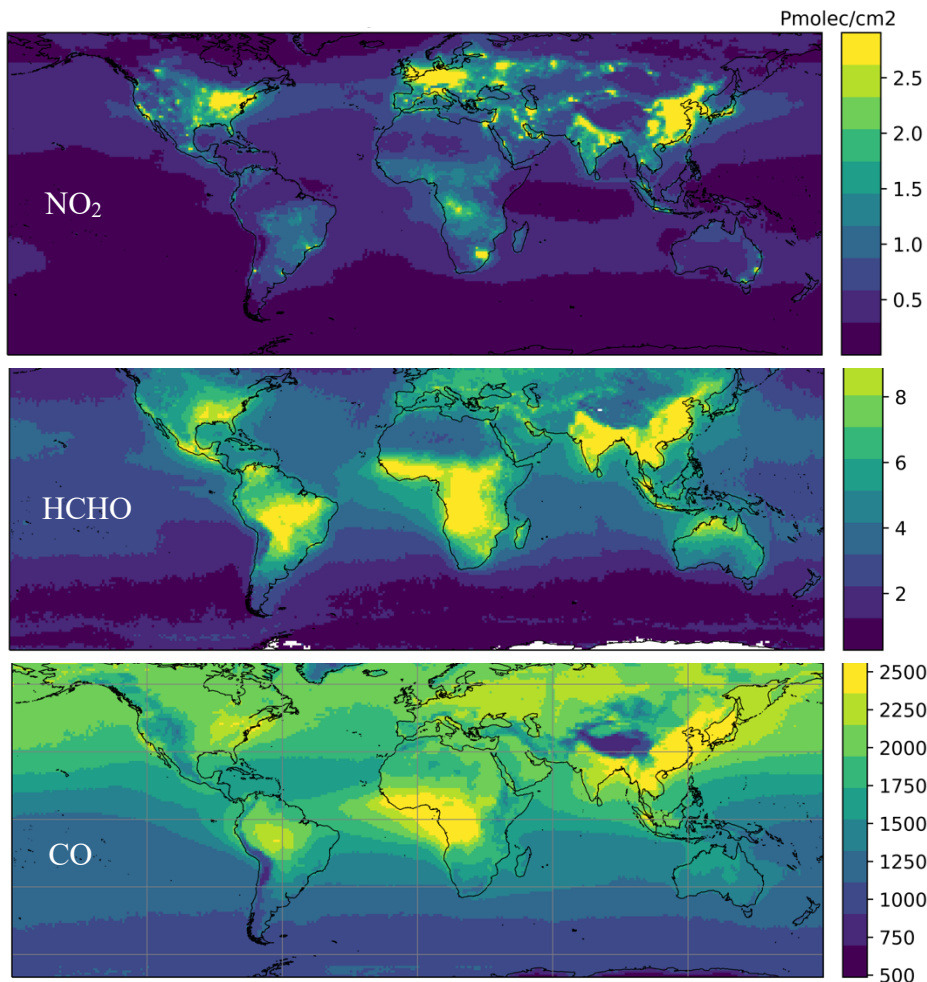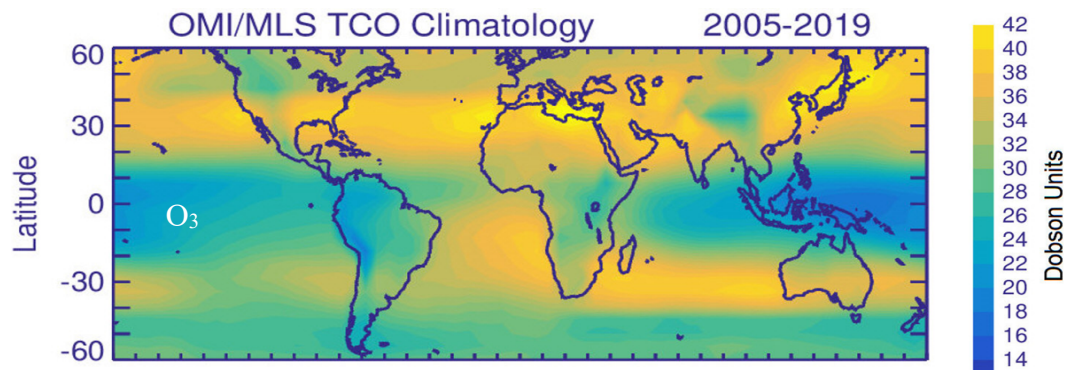
327

328   Figure 4: Mean (2005-2019) of TrC-O_3, TrC-NO_2, TrC-HCHO, and TC-CO.

329   **3.3. Simulated O_3 Precursors**

330   Ozone and its precursors differ in their vertical distribution through the troposphere. In this
331   section, we use the GEOS -simulations to show how the lower, middle, and upper troposphere
332   contribute to the simulated columns of O_3 and its precursors to complement the column
333   information from satellites. Figure 5 shows the simulated mean (2005-2019) contributions to
334   tropospheric columns of O_3, NO_2, formaldehyde, and CO, partitioned into the lower (up to
335   700hPa), middle (700-400hPa), and upper (400hPa to tropopause) portions of the troposphere for
336   the tropical band (30ºS:30ºN) and the global mean. The middle and upper troposphere make

337 large contributions to the simulated TrC-O$_3$ and its variability (Figure 5). The lower troposphere
338 makes the largest contribution to the TrC-HCHO since it is mainly a photochemical product
339 (e.g., Elshorbany et al., 2009), and all three levels make substantial contributions to the CO
340 column. Globally, the relative contributions for TrC-O$_3$, TrC-HCHO and CO are similar to those
341 of the tropics. However, for TrC-NO$_2$ the lower troposphere makes a smaller contribution in the
342 tropics than globally.

343
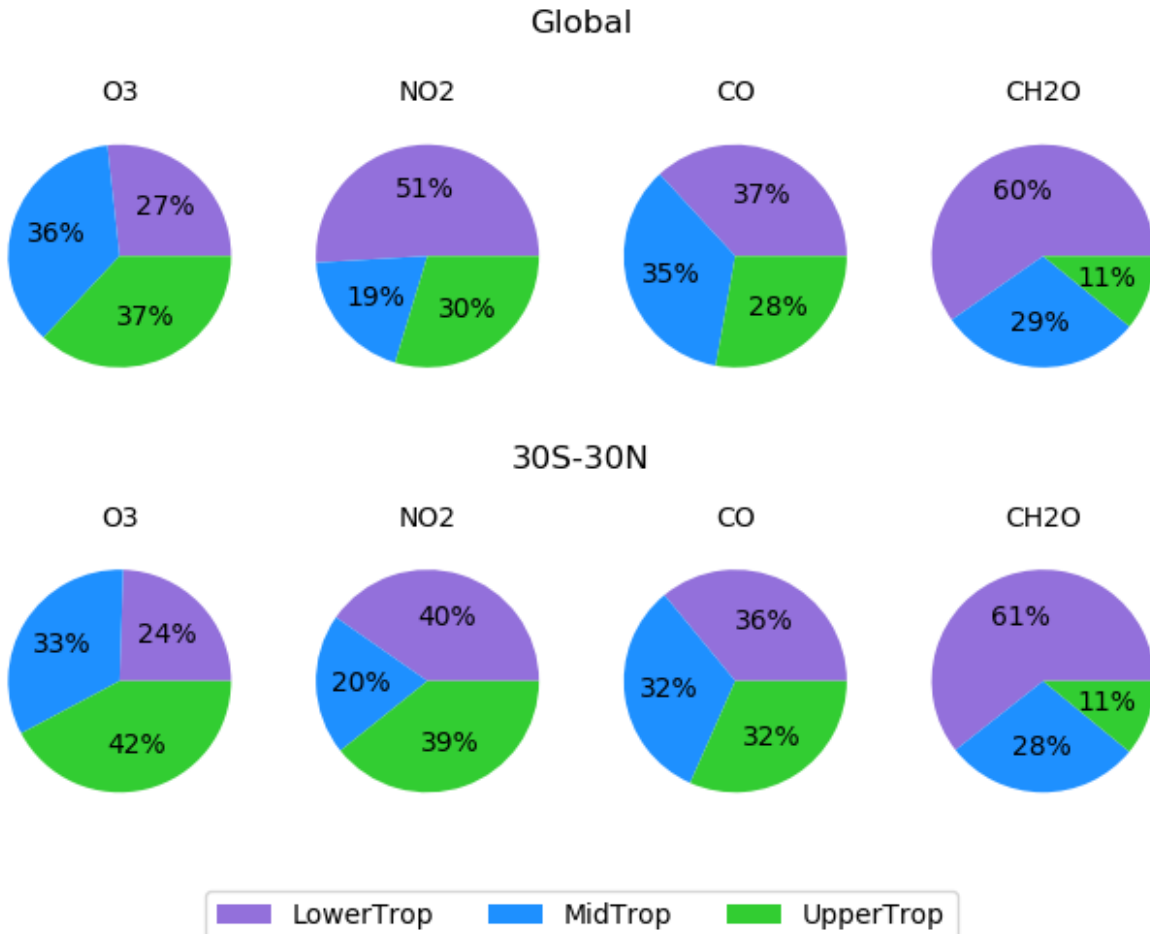
344

345 Figure 5: Simulated average (2005-2019) contributions to the tropospheric columns of O$_3$, NO$_2$,
346 formaldehyde, and CO from the lower (surface-700hPa), middle (700-400hPa), and upper
347 troposphere (400hPa-tropopause) using NASA GEOS-GMI. The top row is for the global mean,
348 while the bottom row is averaged from 30°S-30°N.

349 **3.4. Tropospheric Trends**

350 **3.4.1.   Global Tropospheric Ozone**

351 Global TrC-O$_3$ trends calculated for different column depths are shown in Figure 6. Compared to
352 TrC-O$_3$, OC trends up to 150 hPa seem to be the closest despite OC values being much higher
353 than that of the TrC-O$_3$ (Figure 2). All trends with high confidence, HC (at 95% confidence) are
354 positive indicating increasing trends of ozone columns, regardless of the tropopause height. Low
355 confidence, LC (at 2 σ levels) decreasing TrC-O$_3$ trends were also found in some locations, e.g.,
356 South Australia, South Africa, and the northeastern coast of the US. Increasing trends in the

357 northern midlatitudes may also be partially related to STE (Willimas et al, 2019; Li et al., 2024).
358 While the annual trends inform about overall trends, seasonal trends provide insights into local
359 chemistry and meteorology. For example, during the boreal summer months, June, July, and
360 August (JJA), TrC-O_3 HC trends are similar to the annual trends except for HC decreasing trends
361 over South America and South Africa and HC increasing trends over the west and central Africa
362 and Central America (Figure S7). During the boreal winter months, HC trends are also similar to
363 the annual trends (Figure 6) except for HC increasing trends over Europe, North America, South
364 America, and South Africa (Figure S7).

365
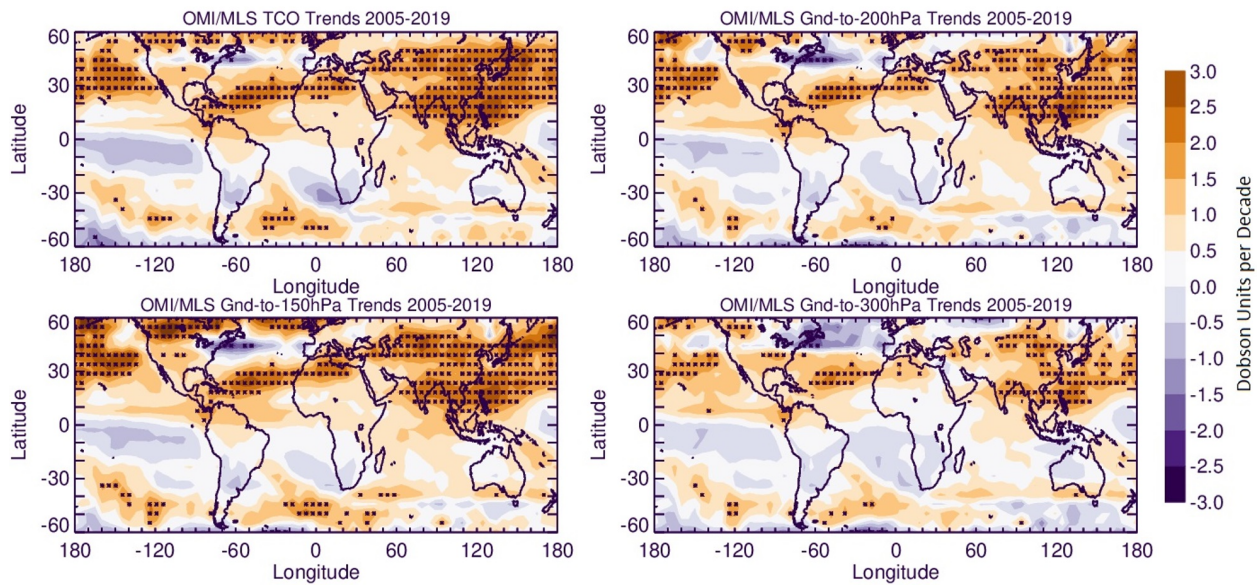
366
367 Figure 6: Trends in tropospheric column ozone, based on the WMO thermal definition, and the
368 trends on ozone columns (from ground to 150, 200, and 300 hPa). Trends are calculated based on
369 deseasonalized monthly data from 2005 to 2019. Asterisks denote 95% confidence trends.

370

371 The time series of OMI/MLS TrC-O_3 averaged over several latitudinal bands and at different
372 column depths are shown in Figure 7. Zonal mean TrC-O_3 compares well with partial ozone
373 columns in the tropics (from 30ºS to 30ºN) with the OC of up to 300 hPa differing by about 10
374 DU from the TrC-O_3 (Figure 7b). The lowest TrC-O_3 trends are located in the northern
375 hemisphere (30 – 60ºN) at 0.78±1.16 DU/decade, followed by the southern hemisphere (30-60ºS)
376 (0.95±0.75 DU/decade) and the tropical band (30-30ºN (1.06±0.40 DU/decade). In addition, the
377 continental trends over Australia, South Africa, and South America in the 30 ºS -60ºS band are
378 essentially negative and the positive trends in this band are contributed mainly by oceanic
379 regions (see Figure 6). The positive trends in the 30ºN -60ºN band are slightly offset by the
380 negative trends over the northeastern US and western Europe (see Figure 6).

381
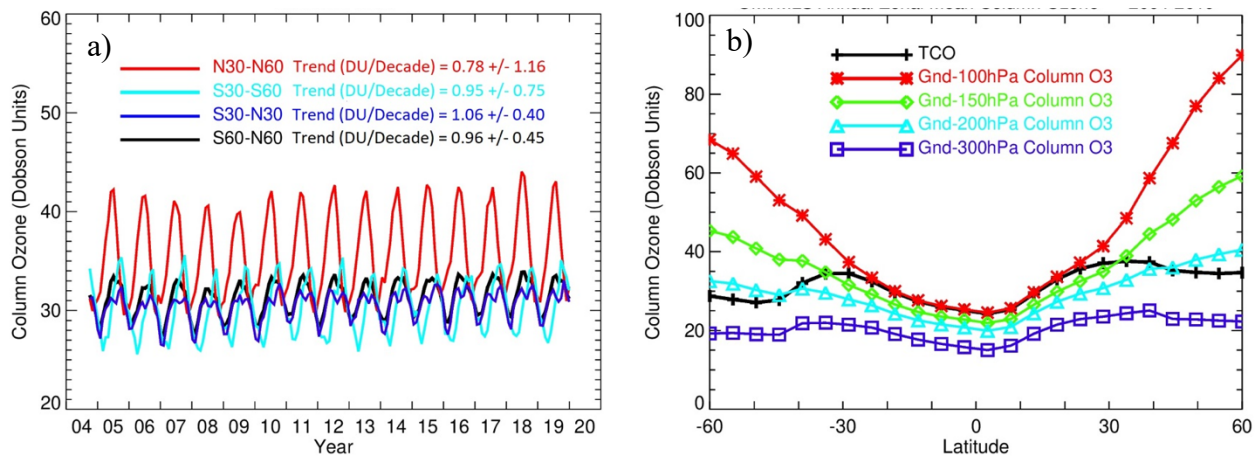
382

383 Figure 7: Time series and zonal mean trends of OMI/MLS TrC-O$_3$ in different latitudinal bands
384 (left) and zonal mean of different column depths (right) from 2005-2019.

385   Observed trends for the time period before COVID-19 (2005-2019) show that OC trends
386 were highest in the northern latitudes (0-30º N) reaching about 1.5 DU/decade, followed by the
387 northern midlatitudes 30-60ºN (Figure 8). The high trends in the 30-60ºN band are dominated by
388 transpacific impacts as well as some impacts from East Asia. The positive trends in the southern
389 hemisphere (0-30º S) are mainly over Amazonia and Southeast Asia, being offset by small
390 negative trends over Western Australia and South Africa. The trends during the time period
391 (2005-2021) show a decline in O$_3$ column trends in the northern hemisphere but a slightly
392 increasing trend in the southern hemisphere (Figure 8b). The decreasing trends in the northern
393 hemisphere during the COVID-19 is consistent with previous literature showing a decrease in
394 several pollutants including NO$_2$ and O$_3$ due to the extended lockdown periods imposed during
395 the pandemic (e.g., Bauwens et al., 2020; Elshorbany et al., 2021; Steinbrecht et al., 2021; Putero
396 et al., 2023). The decrease of NO$_2$ in some parts of Europe and the northeastern USA led to a
397 decrease in tropospheric O$_3$.

398   Zonal mean trends (Figure 8) show that OC up to 150 hPa is almost identical to that of
399 TrC-O$_3$ except for the high latitudes 45º-60º S and 45º-60º N. The decreasing trends above 30ºN
400 and 30ºS are due to the offsetting impact of negative trends over the northeastern US and western
401 Europe in the north, and Australia and South Africa in the south, respectively. This impact is less
402 apparent in the 150 hPa OC due to the lower positive trends in that band compared to TrC-O$_3$.
403 The 200 hPa OC comes next with a very good agreement from 60º S to 10º N. followed by the
404 100 hPa which is only in good agreement from 30º S to 30ºN, while the 300 hPa OC was the
405 farthest from the TrC-O$_3$. The decrease of O$_3$ in the northeastern US and western Europe is
406 consistent with decreasing NO$_2$ trends and NO-sensitive conditions dominating these regions.
407 The decreasing trends of NO$_2$ (see below) are due to the successful measures applied since 2004
408 to mitigate air pollution in these regions. The increase of O$_3$ in the western US maybe due to
409 LRT from eastern Asia (e.g., Itahashi et al., 2020).
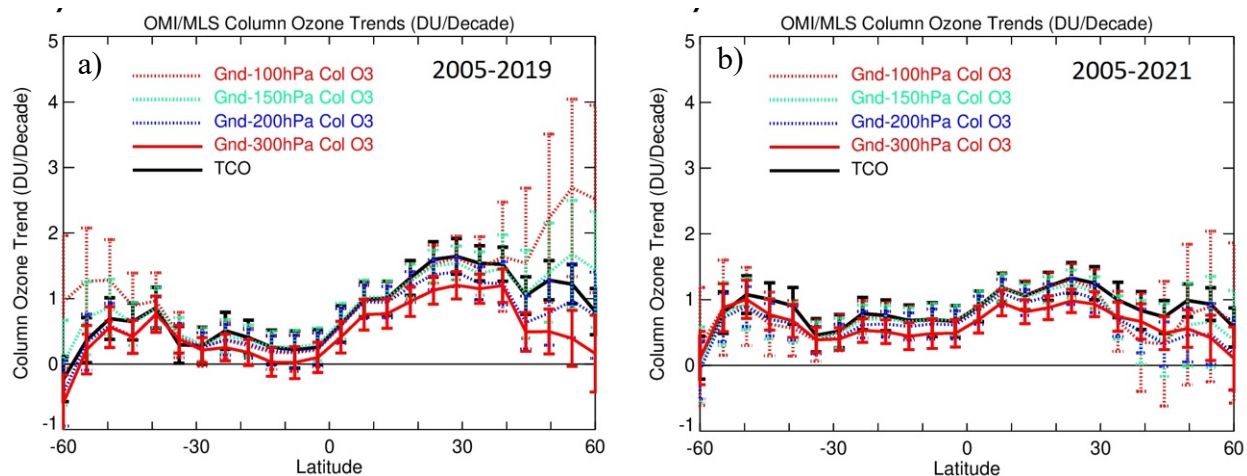
410

411 Figure 8: Tropospheric column ozone (TrC-O₃) and trends for different column depths before the
412 COVID-19 pandemic (2005-2019) and including the pandemic (2005-2021).

413

3.4.2. Free tropospheric trends

415 Trends of ozone in the free troposphere presented here are based on previous work published in
416 the literature. Despite the high stability of ozonesonde measurements across the global networks
417 over several decades (Stauffer et al., 2022), the spatial sparsity of sounding stations and non-
418 uniform sampling frequency among sites is a limitation in using these data to produce trends.
419 These shortcomings have constrained the ability to include data from many stations in previously
420 published analyses. For example, Chang et. al (2020) estimated that at least 18 profiles per
421 month are needed at a single station to calculate accurate long-term trends, while uncertainty
422 increases at lower sampling rates (Chang et al 2024). However, such high sampling frequency is
423 only achieved at three European stations (Hohenpeissenberg, Germany; Payerne, Switzerland,
424 and Uccle, Belgium), while the rest of the global stations work at lower sampling rates.
425 Nonetheless, high-quality ozonesonde observations continue to be the gold standard against
426 which satellite measurements are validated. Likewise, ozonesonde data continue to provide
427 spaceborne observations with climatological feedback. Thus, recent studies have softened the
428 sampling frequency criteria in order to take advantage of the valuable data set collected by the
429 global ozonesonde networks. For example, the latest trend studies establish the minimum
430 frequency requirement to calculate trends to at least three profiles per month (Wang et al., 2022;
431 Christiansen et al., 2022) with at least eight months of sampling in a year, and at least 15 annual
432 means for an analysis of about two decades (Wang et al., 2022). With these criteria, recent
433 ozonesonde trend analyses indicate that ozone concentration increased globally by 1.8+/-1.3
434 ppbv/decade in the free troposphere within 800 to 400 hPa (Christiansen et al., 2022). However,
435 there is high regional variability, as illustrated in Figure 9 where ozone trends published by
436 Wang et. al. (2022) (1995-2017 data between 950-250 hPa) are organized by regions and
437 stations. For example, ozone in East Asia (Japan) has been increasing at a rate of 3.5 to 5
438 ppbv/decade, particularly since 2010 (Christiansen et al., 2022), which may lead to transpacific
439 LRT of O₃ to the western US (e.g., Itahashi et al., 2020). Over the Southwestern Indian Ocean
440 (La Réunion), trends are of similar magnitude (>4.5 ppbv/decade). In tropical South America,
441 over the Atlantic basin region (Paramaribo and Natal), sounding measurements also show ozone
442 increases by almost 3 ppbv/decade (Natal), but other regions in South America continue to lack
443 sufficient measurements to produce trends. At tropical stations in Africa (Nairobi) and the

Pacific Ocean (Hilo and American Samoa) trends are also positive, although of lower magnitudes (0.83-1.7 ppbv/decade). In contrast, polar stations both at the Arctic and Antarctica as well as the Southern Ocean show overall decreasing ozone concentrations to low-confidence trends. Exceptions are the Eureka station in Canada and Lauder station in New Zealand, which both show slight ozone increases (less than 0.5 ppbv/decade). The direction of regional trends by Wang et. al. (2022) is consistent with regional trends presented in similar independent research (Christiansen et al., 2022). As atmospheric composition continues to become modified under the current regime of climate change, building consistent and longer time series of ozonesonde measurements at other regions will continue to be an important source of firsthand information to assess tropospheric ozone changes and trends.
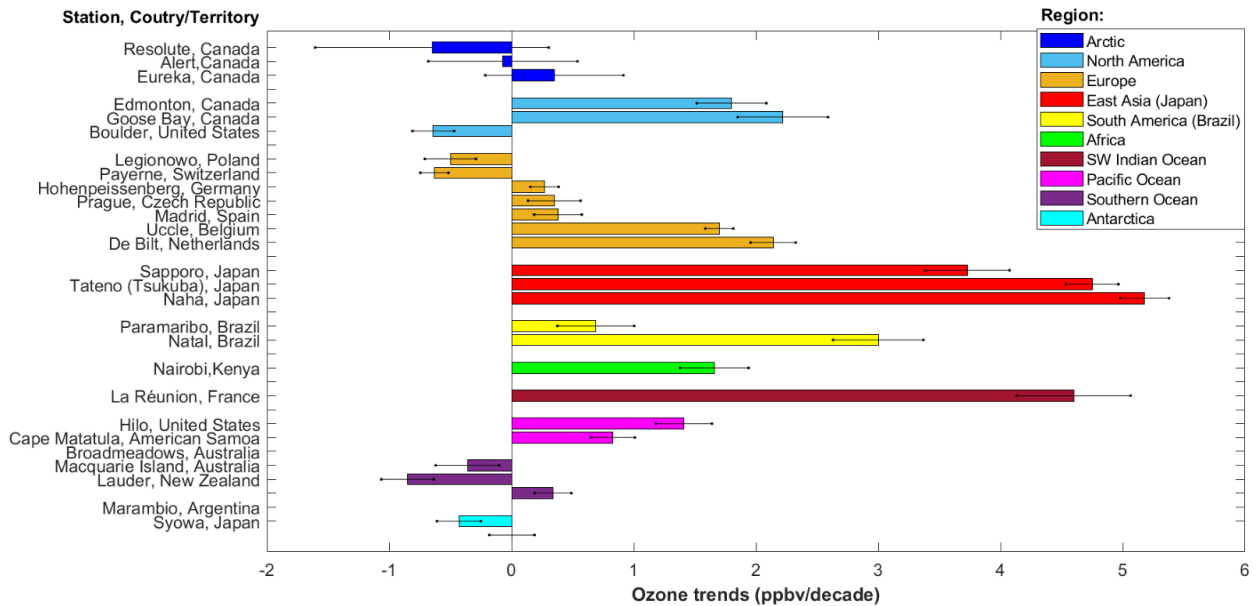
Figure 9: Ozone trends in the free troposphere from ozonesonde measurements calculated by Wang et. Al. (2022) and organized by region and station. Data covers the 1995-2017 period within 950 to 250 hPa. Error bars show 1-σ uncertainty. The coordinates of ozonesonde stations are listed in Table S1.

3.4.3.   Regional Ozone Trends

As shown in Figure 10, the highest OMI/MLS regional trend is observed over East Asia (2.16±1.27 DU/decade) while the lowest trend is calculated over Eastern USA (0.63±1.72) followed by Western Europe (0.89±1.60) and Australia (1.05±1.44) DU/decade. We next calculate the monthly trends from the GEOS-GMI simulation to investigate how the simulated trends vary through the tropospheric column.
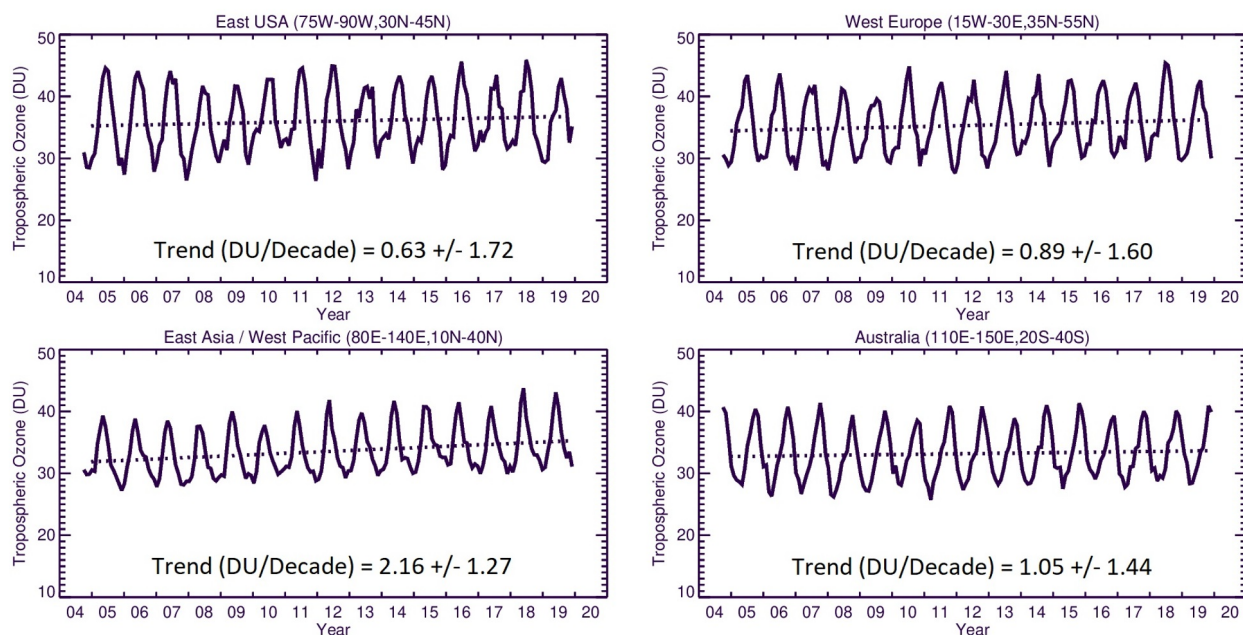
470   Figure 10: OMI/MLS observed regional mean trends of TrC-O_3.

The simulated trends in partial columns (lower, middle, and upper troposphere), as well as the TrC-O_3, TrC-NO_2, TrC-HCHO, and TC-CO from 2005 to 2019, are shown in Figure 11. The simulated tropospheric columns of TrC-O_3 and TrC-HCHO show a positive trend in most regions (Figure 11), consistent with the results of Liu et al (2022) using a different GEOSCCM simulation. Liu et al (2022) highlighted the importance of formaldehyde trends for analyzing the simulated trends in tropospheric ozone. Considering different latitude bands, the highest trends are simulated between 30° S and 60° N, consistent with calculated trends based on satellite observations (see sec. 3.4). In contrast, the simulated NO_2 and CO trends are mostly negative, although positive trends are simulated over East Asia. The largest NO_2 negative trends are in the northern hemisphere between 30°N and 60°N. The decrease in NO_2 trends is consistent with the successful measures to curb emissions of pollution criteria in the US and Europe. The increased trends in TrC-O_3 but decreased trends in TrC-NO_2, and TC-CO might indicate STE contribution (Trickl et al., 2020; Li et al., 2024) in addition to the local chemistry.

486
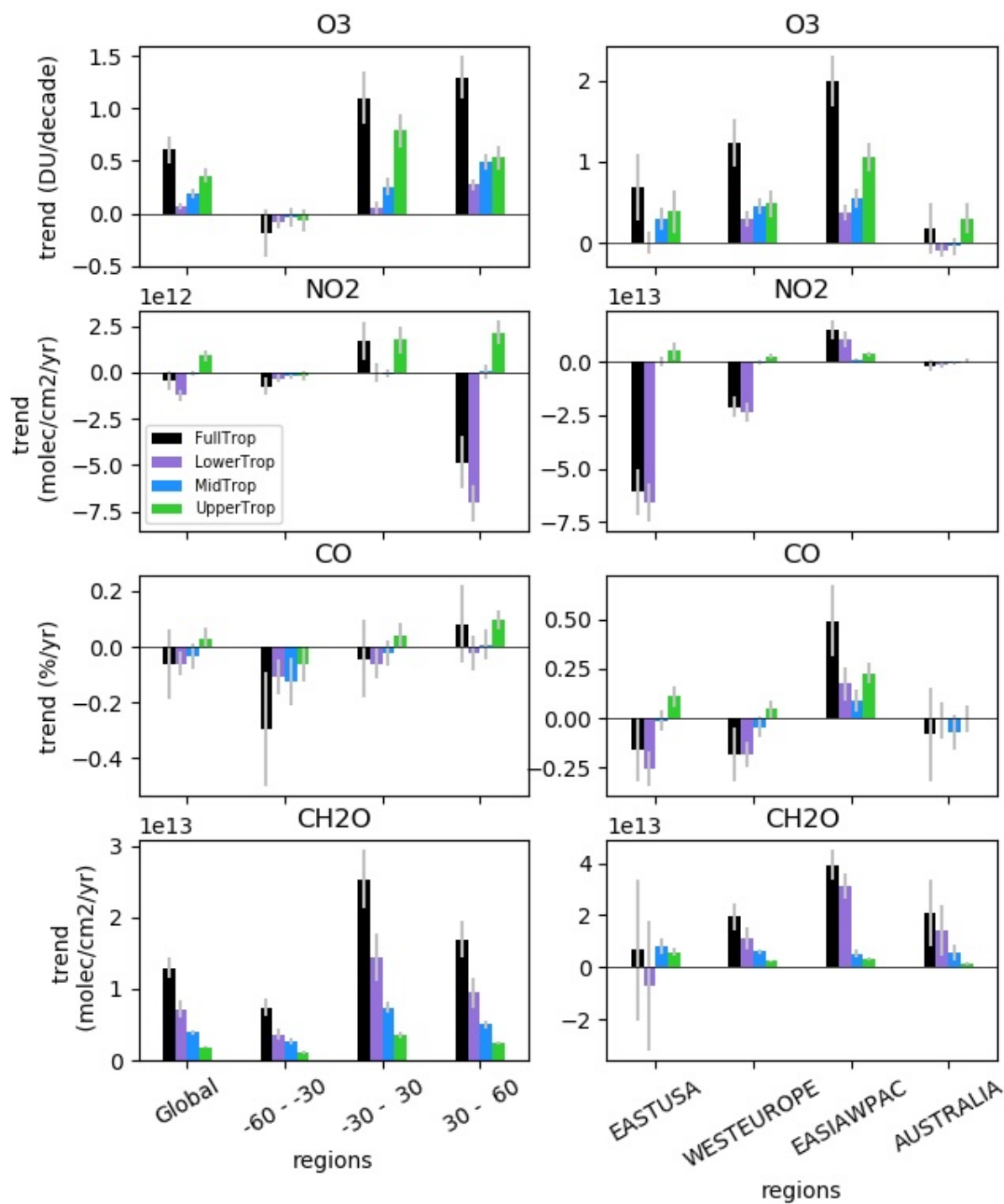
Figure 11: Global and regional trends in O_3, NO_2, CO, and HCHO calculated from the GEOS-
GMI simulation for the tropospheric column (black), lower troposphere (purple), middle
troposphere (blue), and upper troposphere (green) from 2005 to 2019. The lower, middle, and
upper troposphere are defined as in Figure 5.

491

The GEOS-GMI simulation provides an estimate of the relative contribution from different
portions of the tropospheric column to the column trends and shows that this contribution varies
by region and constituent. The middle and upper troposphere make the largest contributions to

495 the simulated TrC-O_3 trend globally, with large contributions from the upper troposphere driving
496 the simulated TrC-O_3 trend at 30°S-30°N (Figure 11). The middle and upper troposphere
497 contribute most of the simulated positive TrC-O_3 trend over the eastern USA, while all three
498 levels contribute over western Europe and East Asia. The upper troposphere makes the primary
499 contribution to the simulated trend over Australia. Simulated TrC-O_3 trends are also quite
500 comparable to those observed by OMI/MLS within the measurement model uncertainty (see
501 Figure 10 and Figure 7). Over Australia, the OMI/MLS trend of 1.05±1.44 DU/decade is higher
502 than the model trend of about 0.18±0.308 DU/decade (see Figure 11). However, since OMI/MLS
503 trend has a calculated uncertainty (2σ) of 1.44 DU/decade, both the model and OMI/MLS for
504 Australia are not statistically different.

505 While the upper troposphere is a major driver of the simulated TrC-O_3 trends, the lower
506 troposphere is the largest contributor to the simulated trends in the tropospheric NO_2, CO, and
507 HCHO globally and over many regions (Figure 11). Exceptions include the simulated NO_2 in the
508 tropics (30°S-30°N), which is dominated by the upper troposphere, the simulated HCHO column
509 over the eastern USA, which is driven by the middle and upper troposphere; an important role
510 for upper tropospheric CO over East Asia; and the CO trend over Australia driven by the middle
511 tropospheric contribution. Figure 11 also shows that in some regions, such as the eastern USA
512 for all 3 precursors, the upper and lower tropospheric trends counteract each other, reducing the
513 magnitude of the column trend. In the following sections, we investigate trends and variability in
514 O_3 precursors, NO_2, CO, and HCHO.

3.4.4. NO_2 Trends

516 The TrC-NO_2 trends over 2005-2019 are shown in Figure 12 with a regional summary in Figure
517 13. On a global scale, there is a strong spatial variability of the TrC-NO_2 trends. About a third of
518 the oceans show HC increase of TrC-NO_2 trends (at 95% confidence level), especially at mid-
519 latitude, with trends up to +0.01 Pmolec/cm^2/yr while only a few cells in the equatorial Pacific
520 show an HC decrease.
521
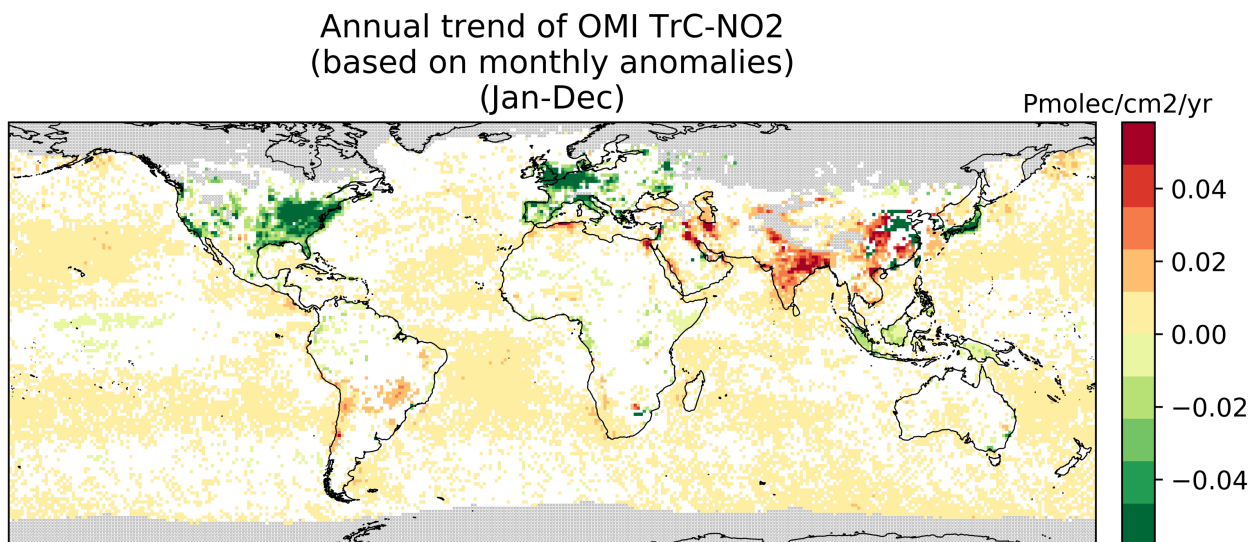
Figure 12: Global trends of OMI NO_2 tropospheric column (TrC-NO_2) over 2005-2019 (see text
for details on the calculation of the trends). Grey areas correspond to areas without enough data,
white areas correspond to regions where the trends remain at low confidence (at a 95%
confidence level).

527   Regional trends are shown in Figure 13. For high-confidence trends in a given region, the
528   numbers correspond to the percentiles 5/50/95 of trends among the different cells of the region
529   where trends are considered high-confidence. Each region is tagged with a circle whose size is
530   proportional to the p50 of the high-confidence trends (red for positive and green for negative),
531   which allows us to quickly see regions where the trend is strong. For instance, for Eastern Asia
532   (this region includes 1442 1°x1° grid cells) about 15% of the grid cells (about 216 grid cells) in
533   this region show a high-confidence decrease in $TrC-NO_2$. Over these specific 216 cells with a
534   high-confidence decrease of $TrC-NO_2$, the 5th and 95th percentile of the trend is -0.34 and -0.01,
535   respectively, $Pmolec/cm^2/yr$. About 28% of the grid cells in this region show a high-confidence
536   increase of $TrC-NO_2$ (which means about 403 grid cells). Over these specific 403 cells with a
537   high-confidence increase of $TrC-NO_2$, the 5th (resp 95th) percentile of the trend is +0.01 (resp
538   0.05) $Pmolec/cm^2/yr$. Therefore, the Eastern Asia region shows sub-regions with high-
539   confidence decreasing $TrC-NO_2$, others with high-confidence increasing $TrC-NO_2$, and the rest
540   with low-confidence (positive and negative) trends. This figure allows us to quickly understand
541   the distribution of the trends within a given region while the overall regional trend is given by
542   the 50th percentile and the circles tagging each region. It's a regional summary of what is shown
543   in the trend global map. In Eastern Asia, the area where trends are with high-confidence positive
544   is more extended than for the high-confidence decrease (28% versus 15%), but the trend values
545   tend to be smaller (at least when comparing the 50th percentiles, -0.05 versus +0.01
546    $Pmolec/cm^2/yr$). The map of regions is included in the supplement. Canada is included in
547   northern America but as shown in the trend map, most of Canada does not have OMI data

548   Over continental areas, high-confidence positive and negative trends are found in about
549   15-20% of the grid cells each (Figure 12). Regions with predominantly decreasing $TrC-NO_2$
550   include western and southern Europe (where about 50-60% of cells with a high-confidence
551   decrease), northern America (40% of cells with a high-confidence decrease, mostly located in the
552   eastern United States), Japan, and Indonesia. In absolute terms, these negative trends reach
553   values of about -0.03 $Pmolec/cm^2/yr$. Specific eastern regions of China also show similar high-
554   confidence $TrC-NO_2$ decreases but overall, a larger part of the country faces increasing trends up
555   to +0.03 $Pmolec/cm^2/yr$. Similar positive trends are observed over most of India, as well as in
556   specific parts of south-eastern Asia (mainly Vietnam) and the Middle East (mainly Iran and
557   Iraq). Conversely, $TrC-NO_2$ trends in Africa and South America remain mainly low-confidence ,
558   except in a few specific regions with high-confidence increases (e.g. South Africa, Morocco,
559   Chile, and parts of Brazil).

560   The trends in NO_2 have varying effects on the tropospheric ozone column, which is
561   related to the different local chemistry in each region. The concomitant decrease in $TrC-O_3$ and
562    $TrC-NO_2$ trends over some parts of the eastern US, and western Europe is consistent with the
563   strict NO_x control measures that were applied over the last two decades. STE can also contribute
564   to increased $TrC-O_3$ trends, especially in the mid-latitudes. A decreasing trend of $TrC-NO_2$ but
565   an increasing trend of $TrC-O_3$ is present in some other regions such as in the central US, which
566   might be due to local chemistry and STE.

567
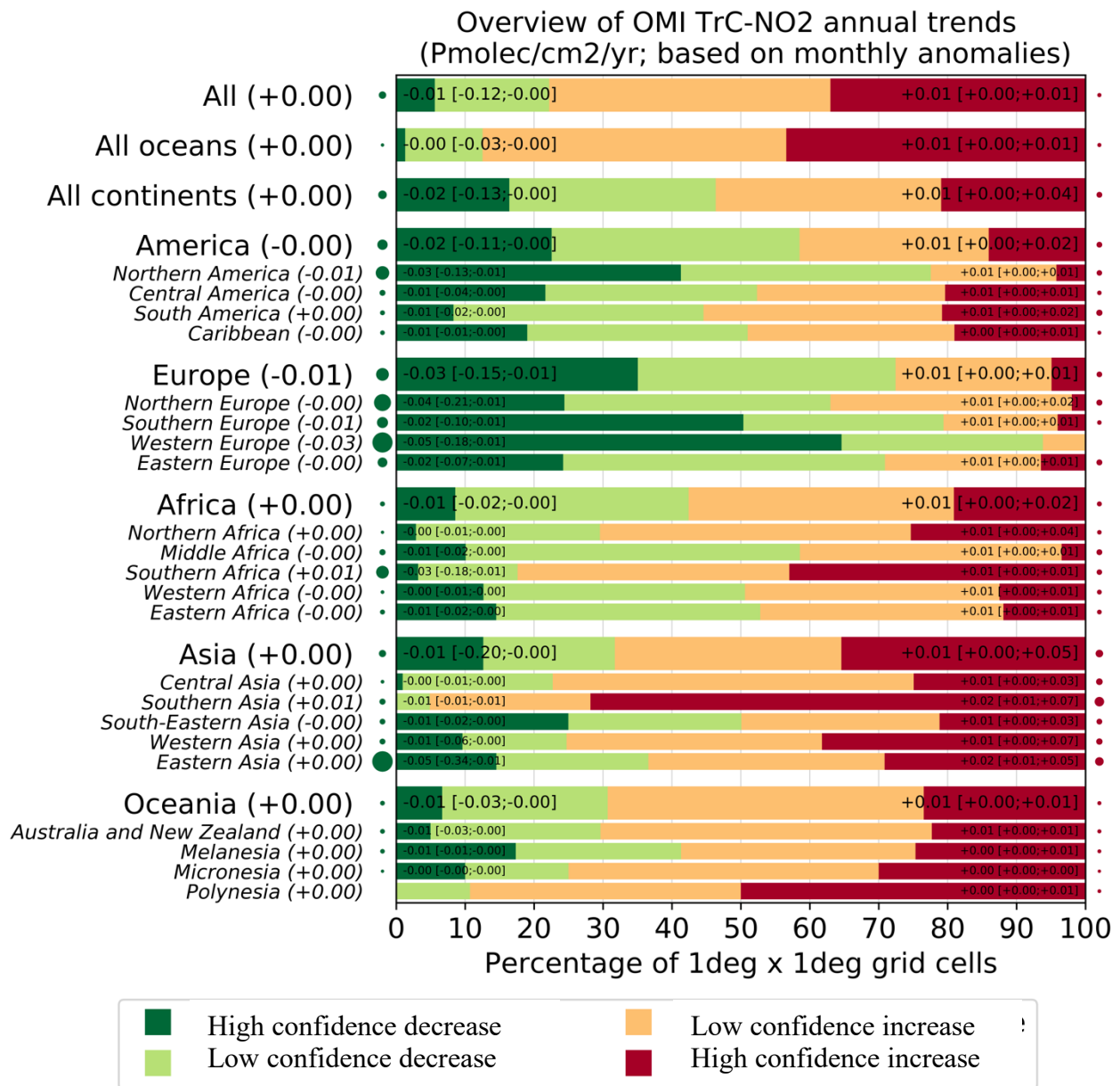
Figure 13: Summary of the high-and low-confidence regional trends of OMI NO₂ tropospheric column (TrC-NO₂) trends over 2005-2019, at a 95% confidence level (see text for details on the calculation of the trends). For each region, the trend on the bars is in the format: p50 [p5; p95], which represents the $50^{th}[5^{th}$, and $95^{th}]$ percentiles of the trends.

Figure 14 shows the time series of regional mean tropospheric NO₂ concentrations from three satellite instruments, OMI for 2005-2020, GOME-2 for 2007-2018, and SCIAMACHY for 2005-2012. All the instruments exhibit common large seasonal and year-to-year variations over both industrial regions and biomass-burning areas. Slight systematic differences among the instruments can mainly be attributed to the different overpass times. The satellite observations show positive trends over China by 2010, followed by a continued decrease. Over the USA and Europe, all the retrievals show a downward trend over the analysis period. Over the US, the observed TrC-NO₂ levels decreased rapidly during 2005–2009 and subsequently show weaker reductions, as

582 discussed by Jiang et al. (2018). A similar slowdown trend is found in Europe. Over India, the
583 OMI observations show positive trends over the 14 years (+1.6 % yr⁻¹). The seasonal and year-to-
584 year variations over Southeast Asia and northern and central Africa are associated with changes in
585 biomass-burning activity (Ghude et al., 2009).
586
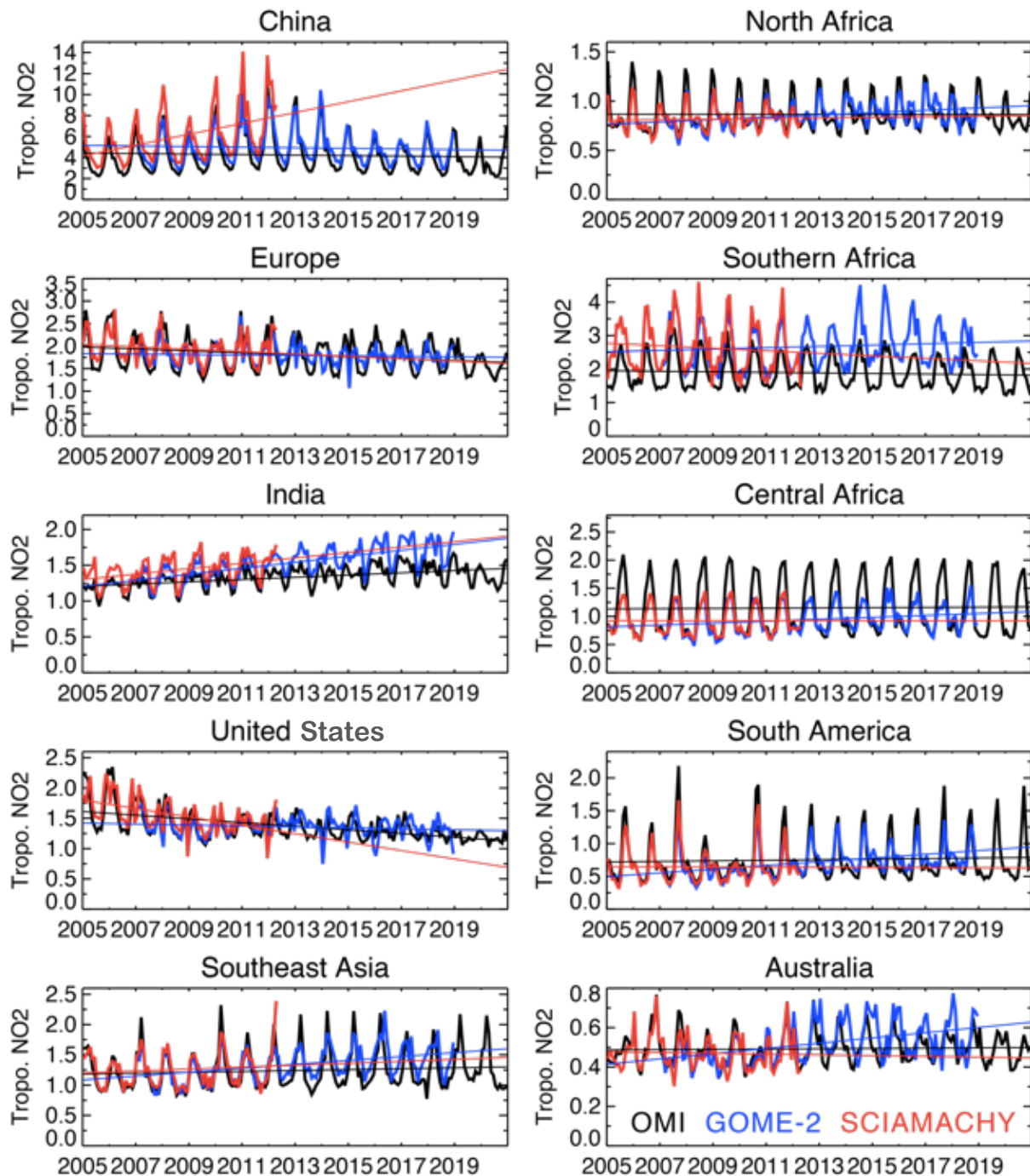
587
588 Figure 14: Time series of regional monthly mean tropospheric NO_2 columns (in 10^{15} molecules
589 cm⁻²) averaged over China (110–123° E, 30–40° N), Europe (10° W–30° E, 35–60° N), the US
590 (70–125° W, 28–50° N), India (68–89° E, 8–33° N), South America (50–70° W, 20° S–Equator),
591 northern Africa (20° W–40° E, Equator–20° N), central Africa (10–40° E, Equator–20° S),

592 southern Africa (25–34° E, 22–31° S), southeastern Asia (96–105° E, 10–20° N), and Australia
593 (113–155° E, 11–44° S) obtained from OMI (black), GOME-2 (blue), and SCIAMACHY (red).

3.4.5.   CO Trends

595 CO trends are calculated based on MOPITT v9 products, see sec. 2.2.1. Observed CO trends
596 below show a slowing in the trend compared to a previous analysis (Buchholz et al. (2021). In
597 the northern hemisphere, CO trends are largely negative over the US and Europe, which is
598 consistent with improvements in combustion efficiency and policies implemented to reduce air
599 pollution since 2004. Except for small sporadic positive trends, no HC trends can be calculated
600 over Central Asia (India and China), while there is a strong negative trend in East China due to
601 the recent strong focus on air quality improvement, and no HC trend in the SH.

Annual trend of MOPITT TC-CO
(based on monthly anomalies)
(Jan-Dec)
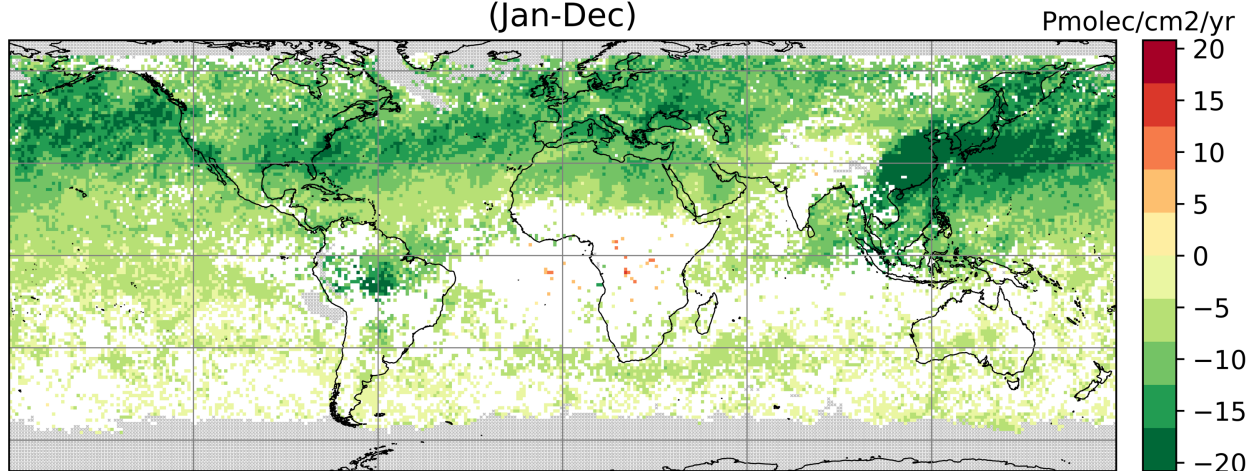
602

603 Figure 15: Trends in TC-CO from MOPITT V9J data, 2005-2019 (see text for details on the
604 calculation of the trends). Grey areas correspond to areas without enough data, white areas
605 correspond to regions where the trends remain statistically low-confidence at a 95% confidence
606 level.

607

608 A regional summary of the trends in the global map is shown in Figure 16. CO trends are
609 predominantly negative everywhere except for some sporadic positive trends over middle Africa.
610 Decreasing TC-CO trends are highest in Europe, followed by Asia and America with about 86%,
611 75%, and 69% of their cells being negative, respectively. The 50 percentiles of the trends in
612 these cells are -12.01, -10.21, and -10.16 Pmolec/cm^2/yr, respectively. Africa shows the lowest
613 decreasing trends as the negative trends in North Africa are being offset by small increasing
614 trends in middle Africa. Overall, about 41% of the cells in Africa show decreasing trends, and
615 50% of the trends in these cells account for -8.71 Pmolec/cm^2/yr. Thus, even though the NH
616 accounts for most of CO emissions, decreasing trends of TC-CO are evident in these regions.

617
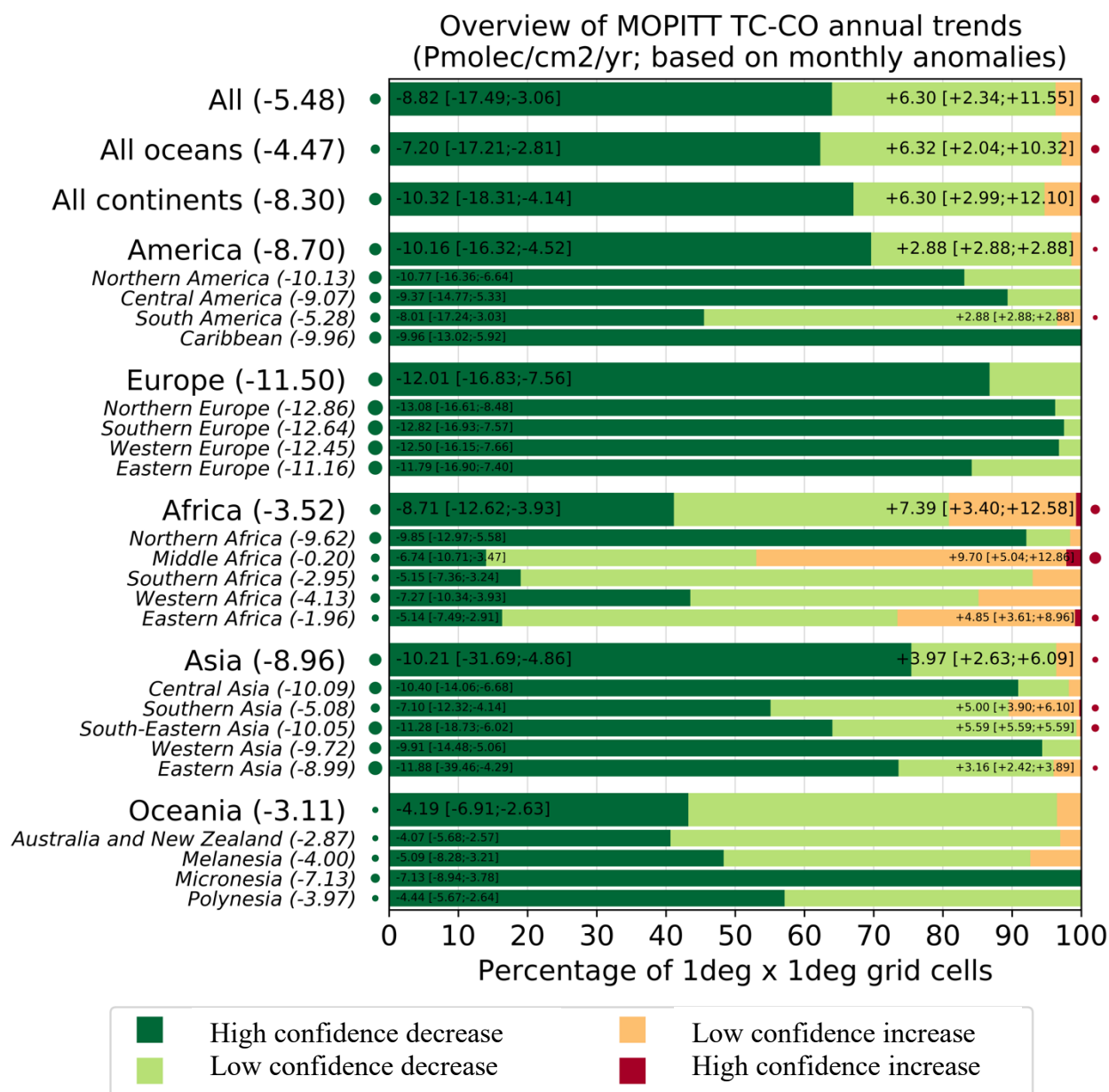
Figure 16: Summary of the statistically high- and low-confidence regional trends of MOPITT TC-CO trends over 2005-2019, at a 95% confidence level (see text for details on the calculation of the trends). For each region, the trends reported on the left (resp. right) represent the 50th[5th, and 95th] percentiles of the trends calculated over the different grid cells showing a high-confidence TC-CO increase or decrease.

Shown below are also the trends in the MOPITT column average volume mixing ratio (VMR) anomalies from 2005 to 2019 (Figure 17) using QR as well as Weighted least squares (WLS)) as Buchholz et al. (2021). The region boundaries are the same as used in Fig. 10 and 11. Results show a HC decreasing trend in the NH (-0.35 ±0.1% annually), a smaller decreasing trend in the Mid-latitudes (-0.26 ±0.1% annually), and LC trend in the SH (-0.14 ±0.1% annually). The three anthropogenic regions investigated in the NH all show strong decreases in CO. The larger negative trend over Australia (-0.2 ±0.1% annually) than the average SH, suggests sources from

632 the other two land regions (Southern Africa and South America) may be counteracting negative
633 trends in CO for the SH.

634
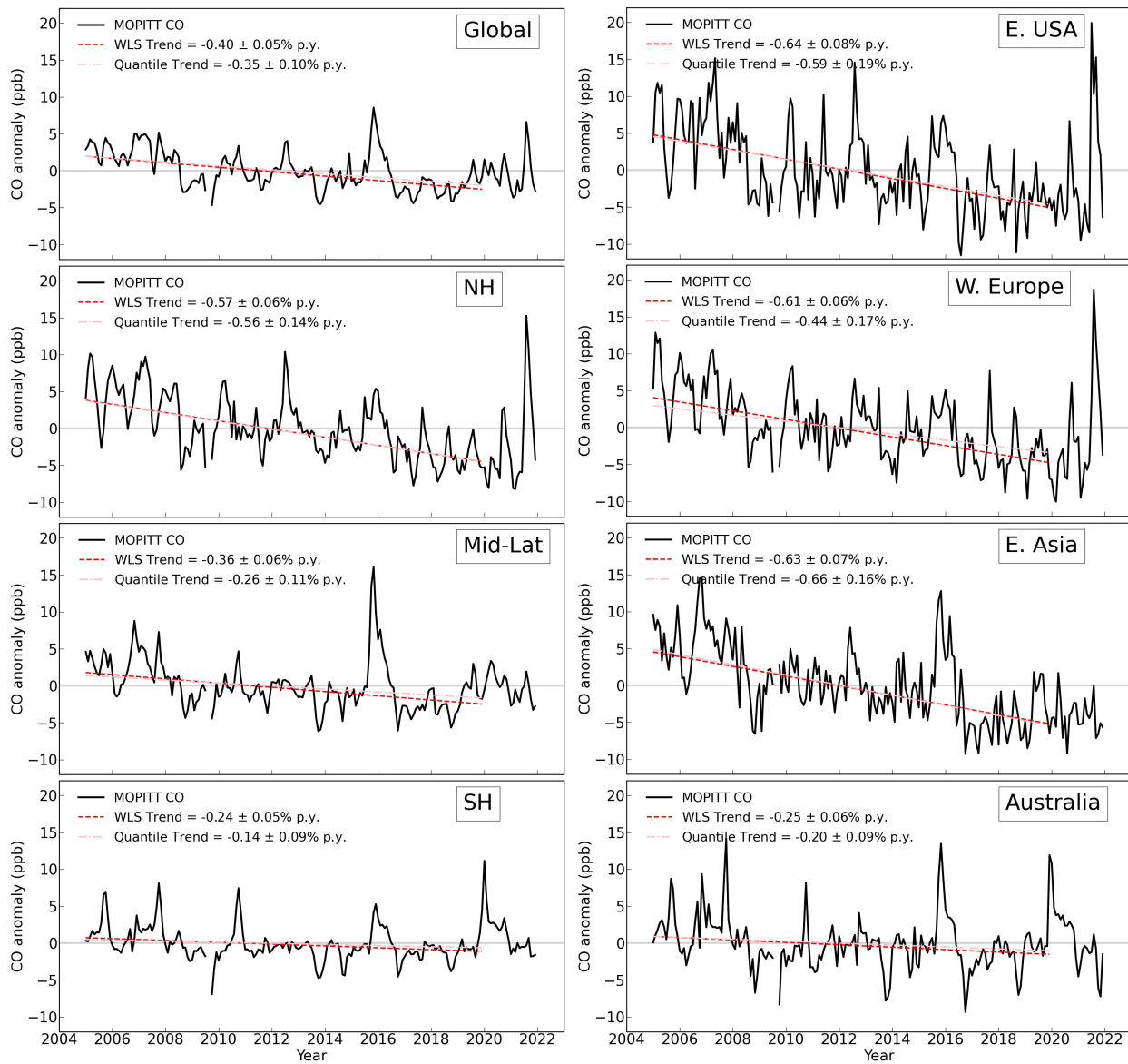
636 Figure 17: MOPITT monthly average CO anomalies in column average volume mixing ratio
637 (VMR, ppb), 2005-2021 (black). Updated dataset based on Buchholz et al. (2021). Data is Level
638 3, monthly average daytime observations, using version 9 joint NIR/TIR retrievals (V9J).
639 Regions are defined in Figure 10 and Figure 11. Trends are calculated on anomalies 2005-2019.
640 The weighted Least Squares trend (red) is weighted by the monthly regional standard deviation.
641 The quantile regression trend is also shown (pink). Grey dashed lines indicate a zero trend.

642

643 We also compare CO trends with Community Earth System Model (CESM) simulations
644 (Supplement Fig S1). While the magnitude of modeled CO tends to be underestimated relative to
645 observations, the anomalies between the model and measurements are comparable, indicating the
646 model reproduces interannual variability well. The negative trends in the NH are also reproduced

647 by CESM, although to a smaller degree than observations, suggesting that the trends in sources
648 or loss processes (such as OH oxidation) are underestimated in the model. These processes will
649 impact the feedback into modeled ozone and the resulting interpretation of driving factors for
650 ozone abundance and variability. Interestingly, CESM correctly represents a negative trend in
651 CO for the NH and East Asia while GEOS-GMI has a positive CO trend in those regions (Fig.
652 11), likely due to the well-known misrepresentation of East Asia air quality improvements in
653 emission inventories (Yin et al, 2015; Strode et al., 2016; Zheng et al, 2019). In the SH, CESM
654 does not predict HC trends.

655

3.4.6.   HCHO Trends

657 HCHO, mainly a photochemical product results from hydrocarbon oxidation. HCHO is itself a
658 source of OH and ozone through its photolysis producing HO_2, which can be recycled back to
659 OH if sufficient NO levels are present.

660 R 3.4-1 $HCHO$ + $h\nu\ (\lambda < 325\ nm)$ $\rightarrow$ H + HCO

661 R 3.4-2 H + O_2 + M $\rightarrow$ HO_2 + M

662 R 3.4-3 HCO + O_2 $\rightarrow$ HO_2 + CO

663 R 3.4-4 HO_2 + NO $\rightarrow$ OH + NO_2
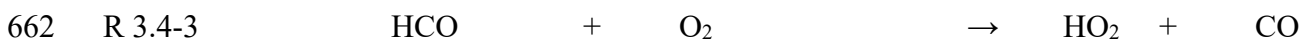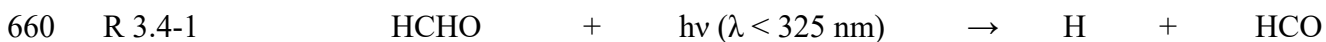
664 Unlike higher aldehydes, the OH reaction with HCHO leads also to the formation of a formyl
665 radical (HCO), which ultimately forms HO_2 (R 3.4-3).

666 R 3.4-5 $HCHO$ + OH $\rightarrow$ H_2O + HCO

667 Due to its solubility, the variability of HCHO also depends on the presence of clouds, and wet
668 deposition ultimately represents another important sink for HCHO (Lelieved and Crutzen, 1991).
669 Overall, HCHO plays a key role in the O_3 budget, both in polluted and remote regions.

670 Trends of the OMI HCHO tropospheric columns (hereafter referred to as TrC-HCHO) are
671 computed as described for OMI TrC-NO_2. TrC-HCHO trends over 2005-2019 are shown in
672 Figure 18 with a regional summary in Figure 19. The first global feature to highlight on the
673 global trends map is the presence of stripes along the OMI orbits. The number of rows affected
674 by the OMI row anomaly has increased over the years (Boersma et al., 2018). The affected rows
675 are filtered out in the HCHO data, but the change in the sampling and the related increase in the
676 noise impact the trend analysis. Along orbit stripes in the trend analysis should be ignored but
677 zonal trends are still valid (Figure 18).

678

Annual trend of OMI TrC-HCHO
(based on monthly anomalies)
(Jan-Dec)
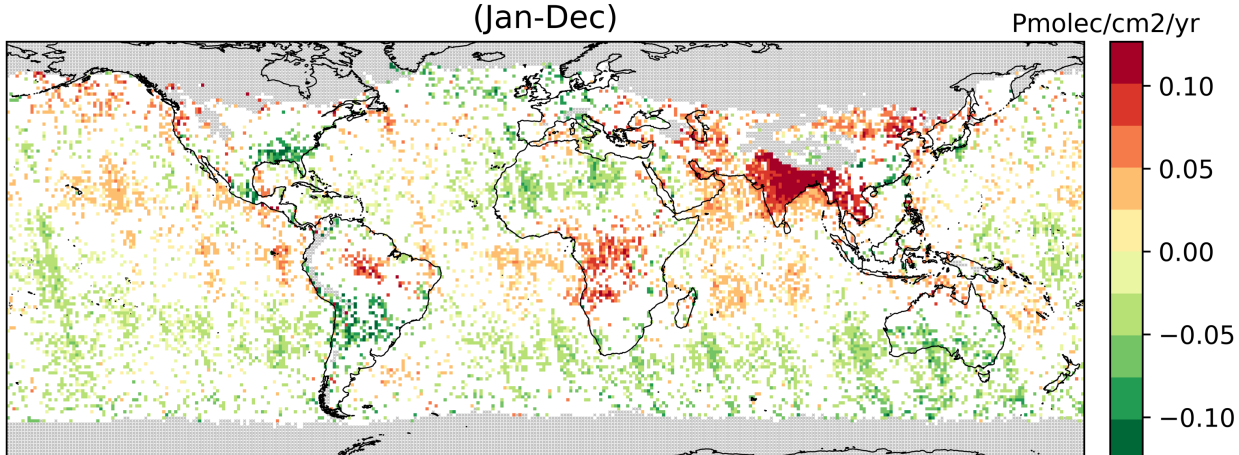
Figure 18: Global trends of OMI HCHO tropospheric column (TrC-HCHO) over 2005-2019 (see text for details on the calculation of the trends). Grey areas correspond to areas without enough data, white areas correspond to regions where the trends remain statistically low-confidence at a 95% confidence level.

Despite the fact that TrC-HCHO trends remain LC over a large part of the globe, specific regions do highlight clear trends. The region with clearest changes is unambiguously southern Asia where about 65% of the cells show increasing trends with a median of +0.09 Pmolec/cm^2/yr. The other regions with a large portion (25-30% of the cells) of increasing trends include the rest of Asia and central Africa, with median TrC-HCHO trends ranging between +0.05 and +0.08 Pmolec/cm^2/yr, as well as some parts of central Brazil (Amazonians). Conversely, some HC decreases of TrC-HCHO are observed in the south-eastern US, the southern half of Southern America, North and western Africa, and southern Australia, although part of them overlap with the aforementioned stripes and might thus not be real.
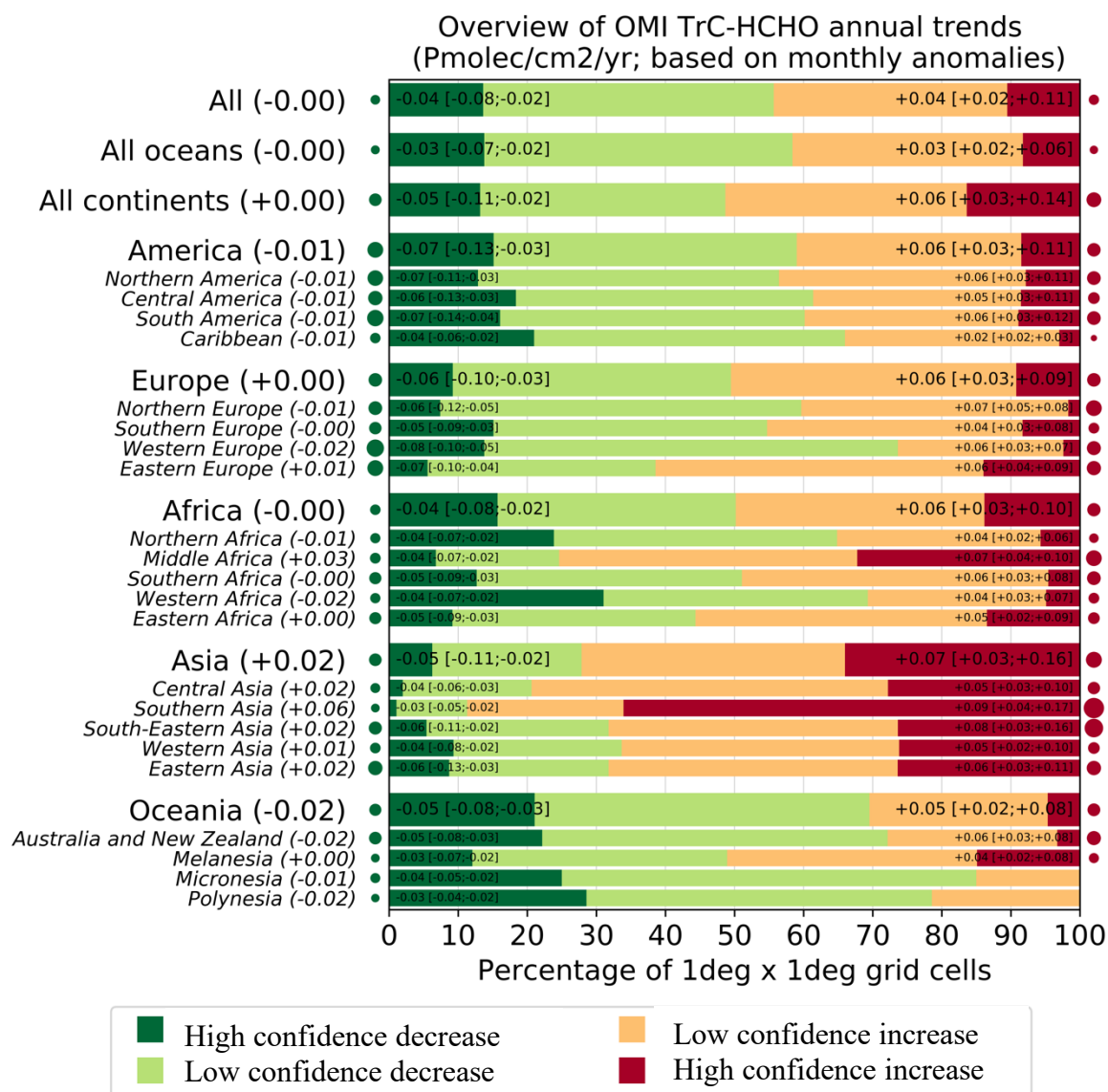
Figure 19: Summary of the statistically high- and low-confidence regional trends of OMI HCHO tropospheric column (TrC-HCHO) trends over 2005-2019, at a 95% confidence level (see text for details on the calculation of the trends). For each region, the trends reported on the left (resp. right) represent the 50th[5th, and 95th] percentiles of the trends calculated over the different grid cells showing a HC TrC-HCHO increase or decrease.

HCHO trends varies with that of O_3 (sec. 3.4.1) which might be due to several factors, such as their different sensitivity to NO_x and hydrocarbons (Luecken et al., 2018) but also possible STE contribution to tropospheric ozone levels, especially in midlatitudes (Willimas et al., 2019; Li et al., 2024). For example, while TrC-O_3 is increasing in the southeastern US, TrC-NO_2, TC-CO, and TrC-HCHO are decreasing, which, in addition to the local chemistry, might indicate a STE signal. TrC-NO_2 trends are decreasing over the northern coast of Australia while those of TrC-O_3 and TrC-HCHO are increasing. While the increase of HCHO/NO_2 might indicate a trend toward NO-limited conditions (see below), the increase of TrC-O_3 trends in this region might also indicate increasing trends of STE contribution (Li et al., 2024). However, TrC-HCHO trends are

710 consistent with that of TrC-O$_3$ in other regions, e.g., over the northeastern US and Europe.
711 Similarly, while NO$_2$ trends are slightly increasing over central and southern Australia, trends of
712 TrC-O$_3$ and TrC-HCHO are decreasing, which indicates a trend toward VOC-limited conditions
713 (see below).

714

3.4.7. HCHO/NO$_2$

716 The ratio of TrC-HCHO/TrC-NO$_2$ observed from space (e.g., Martin et al., 2004) has been used
717 in a number of studies to give insights on the O$_3$ chemical regime, higher (resp. lower) TrC-
718 HCHO/TrC-NO$_2$ ratios indicate NO$_x$-limited (resp. RO$_x$-limited) regimes. Although imperfect
719 (e.g. Souri et al., 2023), this indicator yet provides some qualitative information on the evolution
720 of the O$_3$ regime over the last years (Nussbaumer et al., 2023). We note that this analysis does not
721 consider variations in the ratios and their trends with respect to season or altitude. The mean TrC-
722 HCHO/TrC-NO$_2$ over 2005-2019 are shown in Figure 20, and the trend results are in Figure 21
723 with a regional summary in Figure 22. The highest ratios are observed in the tropical regions due
724 to strong TrC-HCHO from biogenic sources and fire NMVOC emissions in tropical South America
725 and Africa combined with relatively low TrC-NO$_2$. Conversely, lower TrC-HCHO/TrC-NO$_2$ ratios
726 are observed across western Europe and north-eastern Asia, and to a lesser extent, the northeastern
727 US.

728
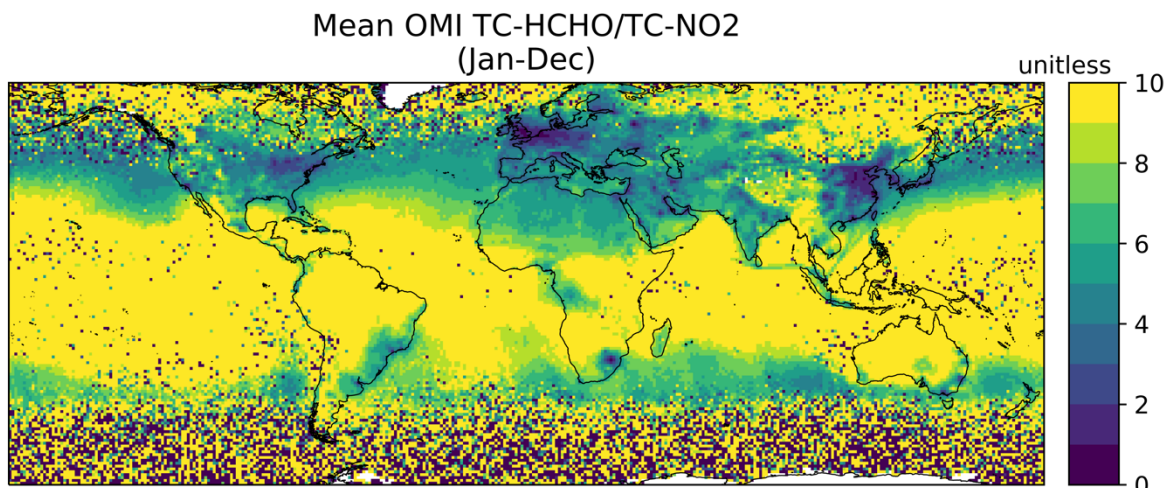
730 Figure 20: Global mean OMI HCHO/NO$_2$ tropospheric column ratio over 2005-2019.

731

732 At a global scale, the HC changes in TrC-HCHO/TrC-NO$_2$ trends (Figure 21-Figure 22) mostly
733 go in the direction of a reduction, with about 25% of the grid cells showing a median trend of -
734 0.52 yr^{-1}. (while only 5% of the cells show an HC increase of +0.03 yr^{-1}) as shown in Figure 22.
735 This suggests that these areas are evolving toward VOC-sensitive conditions (which does not
736 necessarily imply that they are already in this regime). This situation is observed over a large part
737 of Oceania (especially Polynesia) and specific parts of Africa, Asia, and South America. The
738 opposite HC trends, toward more NO-sensitive conditions, are mainly observed over Europe and
739 northern America, as well as South Asia. We note that the mean TrC-HCHO/TrC-NO$_2$ indicates
740 the mean status of the chemical regime over this period of time (2005-2019). However, the trends
741 of the TrC-HCHO/TrC-NO$_2$ ratio show the changing sensitivity of the chemical regime over this

742   period of time. For example, while the ratio in the Eastern US indicates VOC-sensitive conditions,
743   the trends of TrC-HCHO/TrC-NO₂ indicate a direction toward NO-sensitive conditions.
744

Annual trend of OMI TrC-HCHO/NO2
(based on monthly anomalies)
(Jan-Dec)
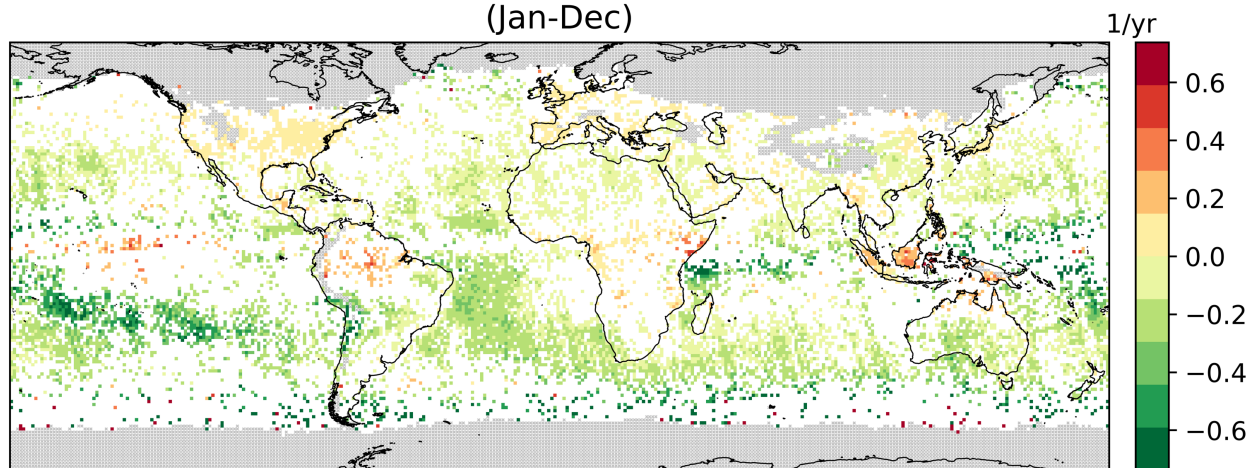
745

746   Figure 21: Global trends of OMI HCHO/NO₂ tropospheric column ratio over 2005-2019 (see
747   text for details on the calculation of the trends). Grey areas correspond to areas without enough
748   data, white areas correspond to regions where the trends remain statistically low-confidence at a
749   95% confidence level.

750

751   The trends on the TrC-HCHO/TrC-NO₂ ratio is mainly driven by specific trends on TrC-HCHO
752   and/or TrC-NO₂, depending on the region. The ratio increase in southern and western Europe and
753   southeast Asia appears primarily due to decreasing TrC-NO₂, since TrC-HCHO does not change
754   with HC. Over North America, observed TrC-HCHO values decrease but less than TrC-NO₂,
755   which thus drives the ratio toward an increase. Conversely, the increase of TrC-HCHO/TrC-NO₂
756   in equatorial Africa and Amazonians appears mainly driven by increasing TrC-HCHO. The
757   regions with HC decreasing TrC-HCHO/TrC-NO₂ ratio include Chile and Australia, due to both
758   decreasing TrC-HCHO and increasing TrC-NO₂ (Figure 22), indicating a trend towards a VOC-
759   limited regime. Note that over the US, Jin et al. (2020) demonstrated the reasonable ability of the
760   OMI-based TrC-HCHO/TrC-NO₂ trends to capture the transition from RO_x-limited to NO_x-limited
761   regimes over main US cities and found a relatively good consistency between observed changes
762   of the surface O_3 and space-based HCHO/NO₂ increasing trends.

763
764
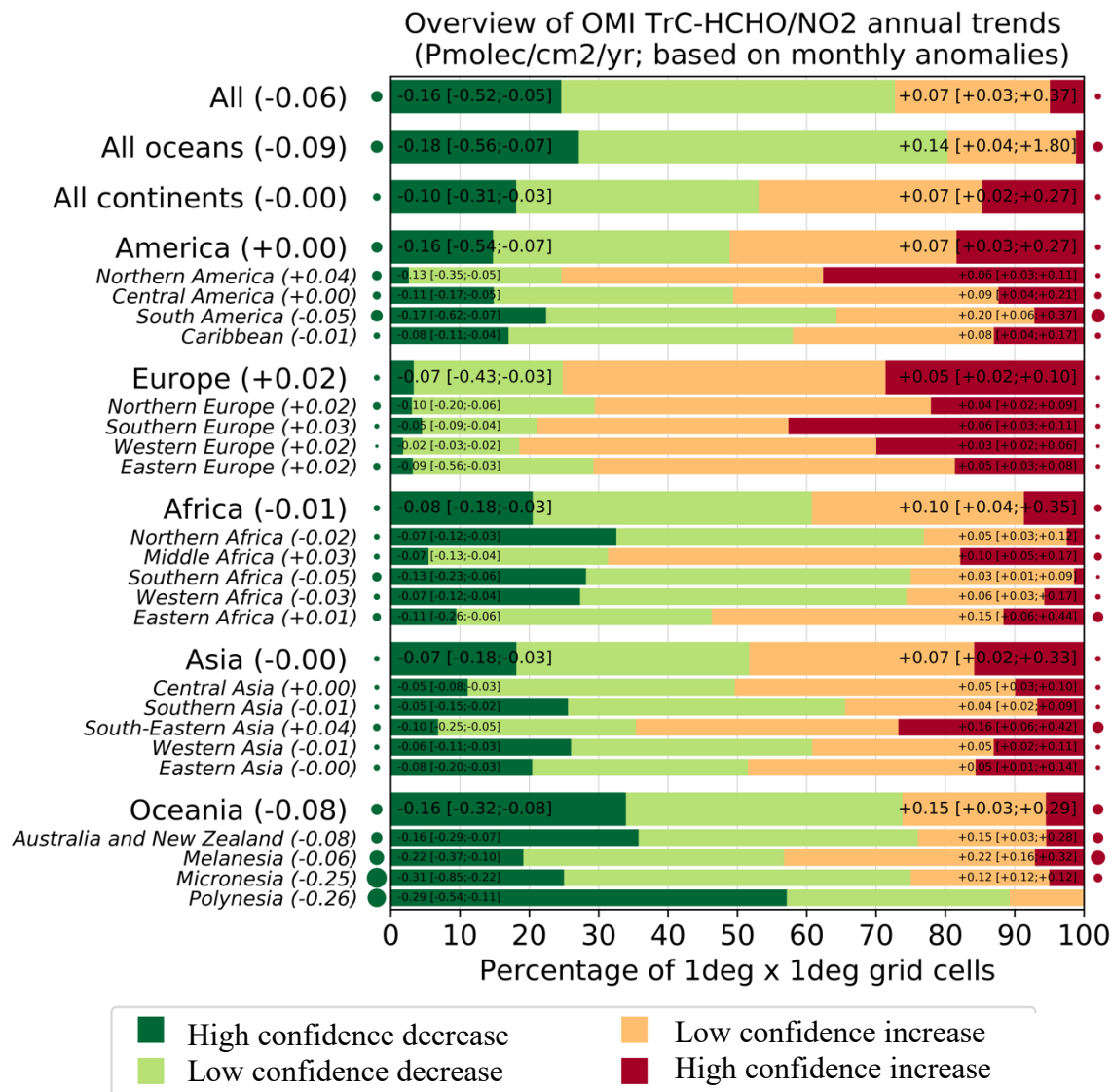
Figure 22: Summary of the statistically high- and low-confidence regional trends of OMI TrC-HCHO/TrC-NO₂ tropospheric column ratio trends over 2005-2019, at a 95% confidence level (see text for details on the calculation of the trends). For each region, the trends reported on the left (resp. right) represent the 50th[5th, and 95th] percentiles of the trends calculated over the different grid cells showing a high confidence TrC-HCHO/TrC-NO₂ increase or decrease.

3.5. Lightning NO$_x$ and Its Effects on Tropospheric NO$_x$ and O$_3$

Nitric oxide (NO) is produced in lightning flash channels and quickly comes into equilibrium with NO$_2$. Cloud-scale simulations of thunderstorms indicate that 55-75% of lightning NO$_x$ (LNO$_x$) is detrained above 8 km (Pickering et al., 1998) where it enhances upper tropospheric NO$_y$, OH, and O$_3$ (Labrador et al., 2005; Allen et al., 2010; Liaskos et al., 2015) and contributes to enhanced longwave radiative absorption by O$_3$ (Lacis et al., 1990; Finney et al., 2018). Enhanced OH leads to a decrease in CH$_4$ lifetime and decreased longwave radiative absorption (Fiore et al., 2006; Finney et al., 2018). The lifetime of NO$_x$ in the upper troposphere is controlled by the chemical cycling of NO$_x$ with reservoir species and is 10-20 days away from deep convection (Prather and Jacob, 1997) but only 2-12 hours in the vicinity of convection (Nault et al., 2016, 2017). This chemical recycling provides a source of NO$_x$ downwind of thunderstorms, which causes the ozone production efficiency of emitted NO$_x$ to be 4-20 times higher in the upper troposphere than at the surface. Thus, LNO$_x$ has a disproportionate impact on the tropospheric O$_3$ budget (Pickering et al., 1990; Grewe et al., 2001; Sauvage et al., 2007).

The distribution of lightning is fairly well known over much of the Earth due to remote sensing observations and an increase in the number and capability of ground-based lightning networks. However, the LNO$_x$ production efficiency (PE, mol fl^{-1}) is a continued source of uncertainty. Schumann and Huntrieser (2007) reviewed the literature on LNO$_x$ production, finding a best estimate of 250 moles per flash, with uncertainty factors ranging from 0.13 to 2.7. The PE can be estimated from theoretical and laboratory considerations (Price et al., 1997; Koshak et al., 2014), using thunderstorm anvil observations by aircraft (Ridley et al., 2004; Huntrieser et al., 2008, 2011; Pollack et al., 2016; Nault et al., 2017; Allen et al., 2021a), based on satellite data (Bucsela et al., 2010; Beirle et al., 2010; Pickering et al., 2016; Bucsela et al., 2019; Lapierre et al., 2020; Zhang et al., 2020; Allen et al., 2019, 2021b), or using cloud-resolved (e.g., DeCaria et al., 2000; 2005; Fehr et al., 2004; Ott et al., 2007, 2010; Cummings et al., 2013; Pickering et al., 2023) or global model simulations with chemistry (e.g. Martin, et al., 2007; Murray et al., 2012; Miyazaki et al., 2014; Marais et al., 2018). These various techniques have yielded PE estimates ranging from <50 to >1000 mol fl^{-1}, with most estimates in the 100-400 mol fl^{-1} range. Miyazaki et al. (2014) assimilated OMI NO$_2$, MLS and TES O$_3$, and MOPITT CO into a chemical transport model to provide comprehensive constraints on the global LNO$_x$ source, resulting in an estimate of mean PE of 310 moles per flash. Marais et al. (2018) used cloud-sliced upper tropospheric NO$_2$ from OMI together with the GEOS-Chem model to estimate a mean LNO$_x$ PE of 280 moles per flash. Lightning is the dominant source of NO$_x$ in the tropical upper troposphere year-round and in the northern mid-latitudes in summer. Lightning is responsible for 10-15% of NO$_x$ emissions globally. Assuming 100-400 mol fl^{-1}, the global LNO$_x$ production is likely $2 - 8$ Tg N a^{-1} (Schumann and Huntrieser, 2007; Verma et al., 2021).LNO$_x$ impacts air quality and deposition (Kaynak et al., 2008; Allen et al., 2012). On average LNO$_x$ adds 1-2 ppbv to surface O$_3$ (Kang et al., 2019b), although contributions as large as 18 ppbv have been seen for individual events (Murray et al., 2016). Allen et al. found that the addition of LNO$_x$ to the Community Multiscale Air Quality (CMAQ) model increased wet deposition of oxidized nitrogen at National Atmospheric Deposition Program (NADP) sites by 43%, reducing low biases from 33% to near-zero. Kang et al. (2019b) found similar improvements for wet deposition and also found that including LNO$_x$ resulted in smaller biases with respect to ozonesondes and aircraft profiles taken during the NASA DISCOVER-AQ field campaign (Flynn et al., 2016). Thus, to accurately assess its impacts on air quality, it is critical that LNO$_x$-producing deep convection is accurately simulated.

820   Only in recent years with the advent of satellite observations of lightning flashes and improved
821   coverage by ground-based lightning networks has there been sufficient data to make estimates of
822   trends in the occurrence of lightning. However, it is unknown whether trends in LNO_x production
823   are similar to those of lightning itself. Lightning characteristics such as the ratio of intracloud (IC)
824   flashes to cloud-to-ground (CG) flashes, the multiplicity (i.e., the number of strokes per flash), and
825   the peak current or energy associated with flashes may vary over time. All of these lightning
826   characteristics may have effects on the magnitude of LNOx production. We have insufficient data
827   to take into account these possible effects on LNO_x production over large spatial domains or over
828   sufficiently long periods of time.

3.5.1.   Global Historical Trends of Lightning

830   The first attempts at an examination of trends in thunderstorm activity were conducted in terms of
831   thunder-days (in Japan by Kitagawa et al., 1989; in Brazil by Pinto et al., 2013). A more recent
832   global analysis was conducted by Lavigne et al. (2019), who analyzed trends in thunder-days
833   (number of days with audible thunder at weather observation stations) over 43 years and in flashes
834   recorded by the Lightning Imaging Sensor (LIS) on the Tropical Rainfall Measuring Mission
835   (TRMM) for 16 years. Thunder-days increased since the 1970s in the Amazon Basin, the Maritime
836   Continent, India, Congo, Central America, and Argentina. Decreases in thunder-days were found
837   in China, Australia, and the Sahel region of Africa. Lavigne et al. (2019) do not provide a global
838   trend in thunder days, but an average trend computed over the nine primary lightning regions that
839   they considered, weighted by the mean annual thunder days in each region, yields a near global
840   estimate of +3.8% per decade. How well do thunder-days represent lightning flash rate? Lavigne
841   et al. found a positive correlation between thunder-days and LIS flash rates in China, the Maritime
842   Continent, South Africa and Argentina, but disagreement on the trend in India and West Africa.

843   Large-scale ($\pm38^{\circ}$ latitude) trends in lightning flashes have been examined in the data collected by
844   the LIS on the TRMM satellite (January 1998 – December 2014) and on the International Space
845   Station (February 2017 – December 2021). Füllekrug et al. (2022; see Figure SB2.1b) demonstrate
846   that the annual mean deviations from the 1998 – 2021 mean are no more than ~5% except for ~-
847   10% in 2020 and ~-8% in 2021. However, no long-term trend is evident from the LIS data. The
848   possibility that these larger negative deviations in 2020 and 2021 are due to Covid-19 lockdowns
849   and general declines in economic activity has been speculated. The link may be provided by
850   changes in Aerosol Optical Depth (AOD) as suggested by Liu et al. (2021) who demonstrated 10-
851   20% flash reductions in March – May 2020 relative to the 2018 – 2021 mean for those months
852   from the GLD360 and WWLLN ground-based lightning networks. Regional lightning reductions
853   were consistent with AOD reductions noted by Sanap (2021). Larger reductions in lightning were
854   noted over Africa/Europe and Asia/Maritime Continent and lesser reductions over the Americas.

3.5.2.   Regional Historical Trends of Lightning

856   Widely varying trends in lightning over China have been reported in the literature. To some extent,
857   whether the trend in lightning is upward or downward depends on the particular region studied and
858   on the period of time considered. Yang and Li (2014) were the first to report on lightning trends
859   in China. They used lightning data from the TRMM/LIS sensor and human-observed thunderstorm
860   day occurrence over the period 1990 to 2012 in southeastern China. Thunderstorms and lightning
861   occurrence increased over the period as well as LIS precipitation radar echo tops heights. These
862   increases were accompanied by decreases in visibility, indicating increases in pollution aerosol.
863   Detailed work on lightning trends in China has been performed in relation to aerosols. Shi et al.
864   (2020) correlated flashes from the TRMM/LIS Low-Resolution Monthly Time Series (2.5 deg.
865   resolution) with AOD from MODIS-Terra V6.1 Level 3 over the period 2001 to 2014. For AOD

< 1.0, r = 0.64, indicating a likely microphysical effect on lightning flash rate. For AOD > 1.0, r = -0.06, which could indicate that with higher aerosol concentration there is a radiation effect stabilizing the atmosphere and/or a decrease in the number of graupel particles in the mixed-phase region of the storms that is important for charging. Flashes were also correlated with surface relative humidity and Convective Available Potential Energy (CAPE). As AOD generally increased over much of the early portion of this time period and then decreased, lightning flash rates followed similar trends. Wang et al. (2021) examined a 9-year record (2010- 2018) of CG lightning from the China Lightning Detection Network in three polluted urban areas of China (Chengdu, Wuhan, and Jinan). They found decreasing trends (see Wang et al., 2021) in CG lightning and total AOD (from the MERRA-2 reanalysis). Annual mean lightning density in these three regions decreased by 50 – 75% as annual mean AOD fell from 0.70 – 0.75 to 0.53 to 0.62.

Qie et al. (2022) analyzed the OTD/LIS record from 1996 through 2013, and found that lightning increased over the eastern Tibetan Plateau by $0.072 \pm .069$ fl km^2 yr^{-1}. Over the 18 years, this increase amounted to a total of 1.3 fl km^2 yr^{-1}, compared with a climatological value of 7.7 fl km^2 yr^{-1}, thereby indicating a HC increase. The ground-based World Wide Lightning Location Network (WWLLN) also showed increased strokes in this region. The increase in lightning frequency in this region was found to be due to an increase in thunderstorm frequency, not increased storm intensity.

Koshak et al. (2015) analyzed National Lightning Detection Network (NLDN) CG flashes over the contiguous United States (CONUS) from 2003 to 2012. The five-year mean flashes over 2008 to 2012 decreased by 12.8% from the five-year mean for 2003 to 2007 (Table 1). The CONUS average wet bulb temperature also trended downward during this period, which may have led to lesser or weaker storms. However, US Environmental Protection Agency air quality trends show an 18% decrease in PM2.5 concentrations over CONUS between the two subperiods, which also could have had an influence on the flash rates. A recent effort to update the Koshak et al. (2015) analysis is underway. NLDN flashes have been reprocessed (Kenneth Cummins, personal communication) from 2015 through 2021 to ensure that the classification of IC and CG flashes is done consistently with data prior to 2015. Trend analysis of NLDN CG flashes from 2003 (a major upgrade of the NLDN network hardware) through 2022 (William Koshak, personal communication) shows a HC reduction in CG flashes over CONUS, comparing the mean CG flashes over 2003-2004 with the mean over 2021 -2022. Within this period a major decrease (~25%) in CONUS CG flashes occurred from 2011 to 2012. Flashes in 2013 remained low, but recovered by 2014-2015. A major decrease (~27%) occurred from 2019 to 2020, with a small increase in 2021. These results have been obtained from ongoing efforts by Dr. William Koshak of the NASA Marshall Space Flight Center, and are presently part of a draft manuscript by lead author Koshak that extends and refines the earlier work in Koshak et al. (2015). Details concerning these trends will be contained in that manuscript.

A possible contributing factor to the CONUs decline in CG flashes over 2003 to 2021 is the substantial decrease in aerosol. Surface annual average PM2.5 concentrations averaged over CONUS decreased by 37% from 2000 to 2021 according to the EPA National Air Quality Trends Report (https://www.epa.gov/air-trends/air-quality-national-summary). However, no decrease in CONUS annual average PM2.5 was seen from 2019 to 2020. As mentioned previously, AOD may be a better indicator of the aerosol amount that may become incorporated into thunderstorm clouds. Sanap (2021) showed negative anomalies of AOD of ~0.1 in portions of CONUS in March and April 2020 and 0.1 to 0.2 in May 2020. The major decrease in CONUS CG flashes from 2011 to 2012 has been related to drought conditions during Summer 2012 over the South Central and Southeastern US (Koshak et al., 2015). The reason for the number of CONUS flashes remaining

913 lower in 2013 is uncertain. Koehler (2020) analyzed 26 years (1993 – 2018) of NLDN CG
914 lightning data to construct a thunder-day climatology for CONUS. Positive anomalies from the
915 26-year mean were found from Texas to Colorado during 2003 to 2007, and negative anomalies
916 in this region during 2008 to 2012. These anomalies were consistent with precipitation anomalies
917 associated with ENSO.

918

919 Holzworth et al. (2021) analyzed primarily CG lightning data from WWLLN for June, July, and
920 August for the years 2010 through 2020. The ratio of lightning strokes north of 65°N latitude to
921 the total global strokes increased by a factor of three over this period. This increase occurred as
922 the surface temperature anomaly in this region increased by 0.3°C (see Holzworth et al., 2021).
923 These results suggest a substantial increase in upper tropospheric NO_x and subsequent ozone
924 production at high northern latitudes.

925

926   3.5.3.   Future Lightning Trends

927   Parameterizations in global chemistry and climate models have been developed for
928 lightning flash rate. These schemes typically use kinematic, thermodynamic or microphysical
929 variables from the model as predictors. In some studies such predictors have simply been applied
930 to output from multiple climate models. This is the case with the Romps et al. (2014) work, which
931 showed that when a lightning parameterization scheme using CAPE x Precipitation Rate is applied
932 to 11 climate models an increase in CG lightning by 12 +/- 5% per degree Celsius of climate
933 warming was computed. This work simply used the 12-hour resolution time series of spatial means
934 of these variables over CONUS as input. Changes in IC lightning flashes were not considered. IC
935 flashes typically outnumber CG flashes by a factor of 3 averaged over CONUS. Therefore, the
936 result of this work is unknown with respect to the amount of change in LNO_x emission. Romps et
937 al. (2018) updated their analysis using CAPE from 3-hourly North American Regional Reanalysis
938 (NARR) data and hourly precipitation from NOAA River Forecast Centers, finding that CAPE x
939 Precipitation Rate captures the spatial, seasonal, and diurnal variations of NLDN CG flash rate
940 over land, but does not predict the pronounced land-ocean contrast in flash rates. Therefore, these
941 analyses are of limited value in estimating trends of LNO_x over broader-scale regions. Romps et
942 al (2019) tested four lightning proxies in a cloud-resolved 4-km resolution simulation over
943 CONUS with the Weather Research and Forecasting (WRF) model, and over the tropical oceans
944 with a Radiative Convective Equilibrium model. The proxies were CAPE x Precipitation Rate,
945 precipitation with vertical velocity > 10 m/s, vertical ice flux at the 260K isotherm, and vertical
946 integral of cloud ice and graupel product. The fractional change in proxy values per 1 degree
947 Celsius of warming over CONUS was +8 to +16%. Over the tropical oceans the changes in proxy
948 values per degree ranged from +12% for CAPE x Precipitation Rate to -1% for ice flux and -3%
949 for the cloud ice and graupel product. Therefore, over broad regions of the Earth, there is great
950 uncertainty on future trends in lightning.

951   Finney et al. (2016; 2018) compared lightning projections for 2100 using vertical ice flux
952 (Finney et al., 2014) and cloud-top height parameterizations for flash rate in the UK Chemistry
953 and Aerosols Model. They obtained -15% global change in total flash rate with ice flux under a
954 strong global warming scenario (see Finney et al., 2018), which was composed of a greater
955 decrease in the tropics and small increases in mid-latitudes. In terms of LNO_x emissions this work
956 using the ice flux scheme produced -0.15 TgN K^{-1} change over the years from 2000 to 2100,
957 implying less O_3 production. With the cloud-top height scheme they obtained +0.44 TgN K^{-1} LNO_x
958 change, implying increased O_3 production. However, the ice flux scheme provided a more realistic

959   representation of global lightning for present day. Therefore, the negative LNOₓ emissions change
960   from this scheme may be more realistic. If indeed the ice flux scheme better represents the current
961   distribution of lightning, both the Romps and Finney results suggest LC   increase in LNOₓ
962   emission in future climate, and possibly a small global decrease. Murray (2018) points out that the
963   ice flux scheme is a closer representation of the underlying charging mechanism, but this scheme
964   needs to be tested in multiple global chemistry and climate models.

965

3.5.4.   Recent findings concerning LNOx PE

967   Recent satellite-based estimates of LNOₓ production (Figure 23) have suggested a possible flash
968   rate dependence of LNOₓ production per flash (Bucsela et al., 2019; Allen et al., 2019; 2021).
969   Smaller values of LNOₓ PE in these studies were found to be associated with high flash rates,
970   likely due to smaller flashes in these conditions (Bruning and Thomas, 2015). Allen et al. (2021a)
971   noted positive correlations (Figure 23) of LNOₓ PE with flash energy and with flash multiplicity
972   (number of strokes per flash). Laboratory studies by Wang et al. (1998) found a positive correlation
973   between peak current and LNOₓ production. Koshak et al. (2015) found an 8% increase in peak
974   current from the 2003-2007 period to the 2008-2012 period that accompanied the 12.8% decrease
975   in CG flashes. These findings make it difficult to project future LNOₓ production given only a
976   prediction of future lightning flashes.

977
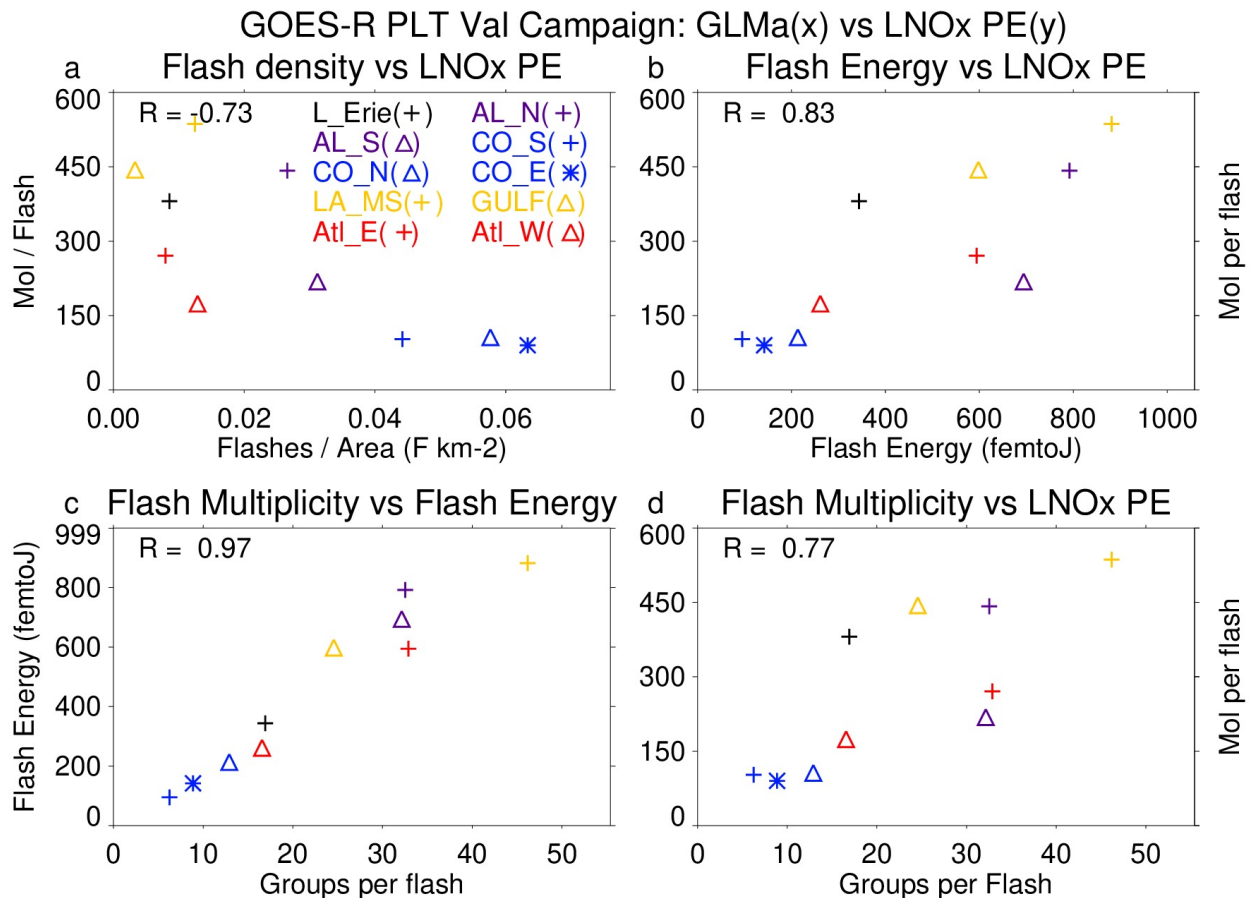
979   Figure 23. Scatterplots showing the GLMa-derived relationship between (a) LNOₓ PE (mol per
980   flash) and flash density (flashes km−2), (b) LNOₓ PE and flash energy (fJ), (c) flash energy and

981   flash multiplicity, and (d) LNO_x PE and flash multiplicity. Colors are used to separate flight days
982   while symbols are used to separate system within each flight day. Correlations are shown in the
983   upper right. LNOx PE derived from airborne remote sensor, the Geo-CAPE Airborne Simulator
984   (GCAS) during the GOES-R Post-launch Test field campaign. GLMa indicates Geostationary
985   Lightning Mapper data adjusted for missing data. From Allen et al. (2021a).

986

3.5.5.   Impacts of LNOx on upper tropospheric O_3

988   The literature concerning the effects of lightning NO_x production on upper tropospheric ozone
989   focuses on photochemical ozone production in storm outflow The STERAO-A storm simulation
990   by DeCaria et al. (2005) indicated that additional ozone production attributable to lightning NO
991   within the storm cloud during the lifetime of the storm was very small (~2 ppbv). However,
992   simulation of the photochemistry over the 24 hours following the storm showed that an additional
993   10 ppbv of ozone production in the upper troposphere can be attributed to lightning NO production.
994   Convective transport of HO_x precursors led to the generation of a HO_x plume, which substantially
995   aided the downstream ozone production. Ott et al. (2007) simulated the July 21, 1998 EULINOX
996   thunderstorm. During the storm, the inclusion of lightning NO_x in the model combined with
997   convectively-transported boundary layer NO_x from the Munich, Germany region resulted in
998   sufficiently large NO_x mixing ratios to cause a small titration loss of ozone (on average less than
999   4 ppbv) at all model levels. Simulations of the chemical environment in the 24 hours following the
1000   storm show on average a small increase in the net production of ozone at most levels resulting
1001   from lightning NO_x, maximizing at approximately 5 ppbv per day at 5.5 km. Between 8 and 10.5
1002   km, lightning NO_x caused decreased net ozone production. Ren et al. (2008) found that net
1003   tropospheric ozone production proceeded at a median rate of ~11 ppbv per day above 9 km in the
1004   Intercontinental Transport Experiment (INTEX-A) in which the effects of frequent deep
1005   convection over the United States dominated the upper troposphere. Apel et al. (2012) noted that
1006   a box model calculation indicated a net ozone increase of ~10 ppbv over a few hours following
1007   observed convection with lightning over Canada in the Arctic Research of the Composition of the
1008   Troposphere from Aircraft and Satellite (ARCTAS) experiment. Apel et al. (2015) performed box
1009   modeling of the chemistry downwind of two DC3 storms in northeast Colorado on June 22, 2012
1010   finding greater ozone production over 2 days (14 ppbv) in the southern storm with more LNO_x
1011   than in the northern storm (11 ppbv). Brune et al. (2018) studied ozone production in the outflow
1012   of the June 21, 2012 DC3 mesoscale convective system. Their Box model calculations yielded a
1013   13 ppbv increase in ozone over 5 hours, similar to the observed 14 ppbv increase. This rate of
1014   increase is larger than others in the literature, perhaps because for a portion of the 5 hours the
1015   outflow was in cirrus cloud, in which photolysis rates may have been larger than clear-sky values
1016   due to multiple scattering. Using a regional chemistry model, Pickering et al. (2023) estimated that
1017   net ozone production in the upper tropospheric outflow of a severe high flash rate storm observed
1018   over Oklahoma proceeded at a rate of 10-11 ppbv day^{-1} during the first 24 hours of downwind
1019   transport. Downwind photochemical production of ozone due to LNO_x accounted for much of the
1020   recovery of upper tropospheric ozone following large reductions due to convective transport of
1021   lower ozone boundary layer air.

3.5.6.   Summary of LNO_x

1023 LNO_x is responsible for the largest fraction of upper tropospheric ozone in the tropics year-round
1024   and in the mid-latitudes in summer. Effects on longwave radiation due to ozone are most sensitive
1025   due to the ozone near the tropopause. Therefore, it is of great importance to have knowledge of
1026   the trends in ozone in this region that are due to changes in frequency and characteristics of

lightning flashes. Considerable uncertainty remains concerning trends in global thunder days. No long-term trend in global flash rates has been found. However, regionally important trends have been noted in CONUS and in China, which tend to be correlated to the decreasing atmospheric aerosol content. An increasing trend at Arctic latitudes has been noted, as that region rapidly warms. Future trends in flash rate also are uncertain, with conflicting predictions coming from models with differing flash rate parameterizations. Flash characteristics (e.g., flash rate, flash extent, flash energy or peak current, intracloud fraction) have been found to have important implications for LNO_x production per flash. Insufficient knowledge of these characteristics on a global scale makes it highly uncertain to estimate changes in LNO_x production, even with knowledge of flash rate trends.

3.6. Soil NO and HONO emissions and their impacts on O_3

Nitrous acid (HONO) is produced from microbial activity in soils with a similar mechanism and strength as NO (Oswald et al., 2013). This emission source may partially account for the current mismatch between observed and simulated HONO levels in the lower troposphere (Su et al., 2011; Yang et al., 2020). Zhang et al. (2016) estimate a 29 % contribution of soil-HONO to the HONO sources in China. This may also contribute substantially to OH production with important implications for the HO_x and O_3 budget. To account for this emission source and assess the global potential for atmospheric pollution soil-HONO emissions have been parameterized based on the HONO/NO emission ratio measured at multiple field samples (taken from different regions of the world) and up-scale it to the 4 major land cover types applied to the whole globe. The study estimates a global emission source of 7 TgN/yr from soil-HONO in 2009 (Emmerichs et al., 2023). This is at the lower end of the estimated range of 7.4-12 TgN/yr presented by Wu et al. (2022) for 2017 who employ an empirical and statistical model in combination with observations. Due to the importance of NO and HONO soil emissions for the O_3 budget their variability and historical and future trends are described here and linked to O_3. Additionally, we discuss a modification of the soil NO emission scheme.

3.6.1. Global modeling of reactive nitrogen emissions from soil

In this section, we present a short overview of the soil-NO emission algorithms and estimates for regional and global emissions. The emission of nitrogen oxides (NO) from the soil is the major source of NO_x in unpolluted regions accounting for 15-25 % of global emissions (Weng et al., 2020, Vinken et al., 2014). Thereby, NO is produced from the nitrification in soil (microbial activity) and depends non-linearly on soil properties like pH, carbon and nutrient content, temperature, and soil moisture (Gödde and Conrad 2000, Oswald et al. 2013). Model algorithms estimate soil-NO emissions with a function dependent on biological and meteorological drivers. The common empirical approach by Yienger and Levy (1995), which is used in the current CMIP6 simulations (Szopa et al. 2022), is based on a biome-specific emission factor, soil temperature, precipitation, and the canopy uptake reduction factor. The resulting global estimate is in the range of 3.3-7.7 TgN/yr which is, however, only at the lower end of the more recent model and observation-based estimates. The Yienge and Levy (1995) approach generally underestimates soil NO for all landcover types except in the tundra and rainforest due to the pulsing parameterization, which describes a large NOx release at the wetting of very dry soil and the subsequent rapid decay (Steinkamp et al., 2009). This is accounted for in the more mechanistic approach by Hudman et al. (2012) representing pulsing of the emissions following dry spells and N-inputs from chemical fertilizer and atmospheric N-deposition. This approach calculates spatial and temporal patterns of soil moisture, temperature, pulsing, fertilizer, manure

1073 and atmospheric N deposition and biome overall replacing the emission factors by Yienger and
1074 Levy (1995) which yields in comparison 34 % more annual global soil emissions of nitrogen
1075 oxide (10.7 TgN/yr). Satellite top-down estimates range from 7.9 TgN/yr (Miyazaki et al., 2017:
1076 2005-2014, assimilation of satellite data sets) to 16.7 TgN/yr (Vinken et al., 2014; GEOS-Chem
1077 and OMI). The emission of soil-NO varies regionally with small sources in Australia (~0.5
1078 TgN/yr), Europe, Russia and Southern Hemisphere (SH) Africa (0.7 TgN/yr, 0.8 TgN/yr),
1079 America (0.9-1 TgN/yr) and high values in S.E. Asia and Northern Hemisphere (NH) Africa (2-
1080 2.1 TgN/yr). The emission estimates (here for 0.25° lat. × 0.3125° lon.) increase with resolution
1081 in some regions like Europe by 38 % (Weng et al., 2020).

1082 Nitrous acid (HONO), a major OH source, is also produced from microbial activity in soils with
1083 a similar mechanism and strength as NO (Oswald et al., 2013). This additional emission source
1084 may account for the current mismatch between models and measurements representing HONO
1085 levels in the lower troposphere (Su et al., 2011; Yang et al., 2020). Soil emissions of HONO play
1086 a major role in the daytime-HONO concentrations in rural areas (in the lowest layers) where
1087 traffic emissions and NO_2 heterogeneous reactions occur less than in urban areas (Wu et al.
1088 2022). HONO photolysis is a main OH source and impacts the oxidation capacity of the
1089 atmosphere (Zhang 2016, 2019). Therefore, this may also contribute significantly to OH
1090 production with important implications for the HO_x and O_3 budget.

1091 ### 3.6.2.   Variability and trends of soil emissions of NO and HONO in the last 15 years

1092 The magnitude of soil emissions varies strongly with season where the emissions rise from
1093 January and July by a factor of 2.5 (Weng et al., 2020). This follows the meteorological
1094 variability as for instance, heavy rainfall over dry grasslands/forests causes a pulse of soil NO
1095 emissions coupled with the usage of fertilizer (Hudman et al., 2012). According to the CCMI
1096 simulations by Jöckel et al. (2016) (following the future ('medium high') climate scenario
1097 RCP6.0 the soil NO emissions show a positive trend since pre-industrial times with a steeper
1098 increase of up to 0.3 TgN/decade from the year 2000. As soil emissions of HONO rely on the
1099 same biogeochemical process with similar dependencies on temperature and water content as NO
1100 also increased from 2000 to 2019.

1101 For soil-HONO, however, the trend over 2005-2019 is much smaller, most pronounced in
1102 Central Africa (Figure 25). Thereby, the highest positive monthly anomalies occur mainly in the
1103 5 most recent years which is likely due to the more frequent heat wave occurrence, e.g. in Europe
1104 and North America. Overall, Africa relates the most (~30%) to the global anomaly (Figure 24 -
1105 Figure 25).

1106
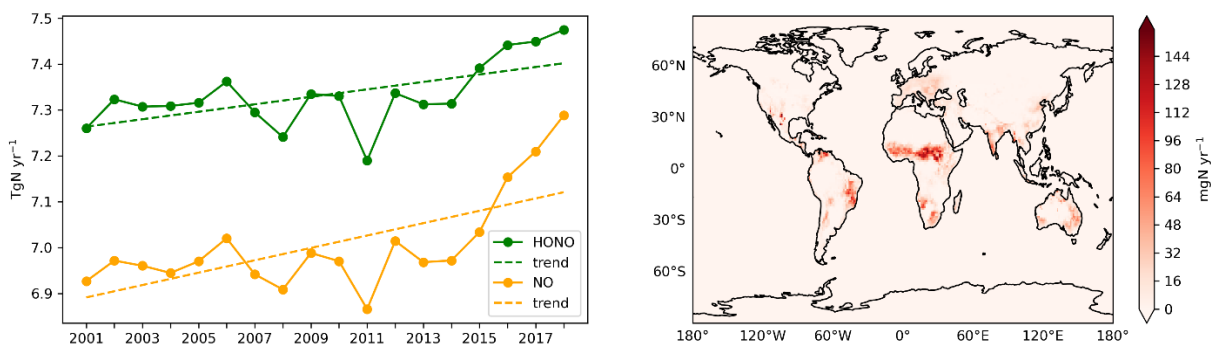
1107

1108 Figure 24: Time series of soil-HONO and soil-NO emissions and their trends (left) and the mean
1109 global distribution of the soil-HONO emission trend for 2005-2019 based on monthly anomalies
1110 (right).

1111

1112

1113
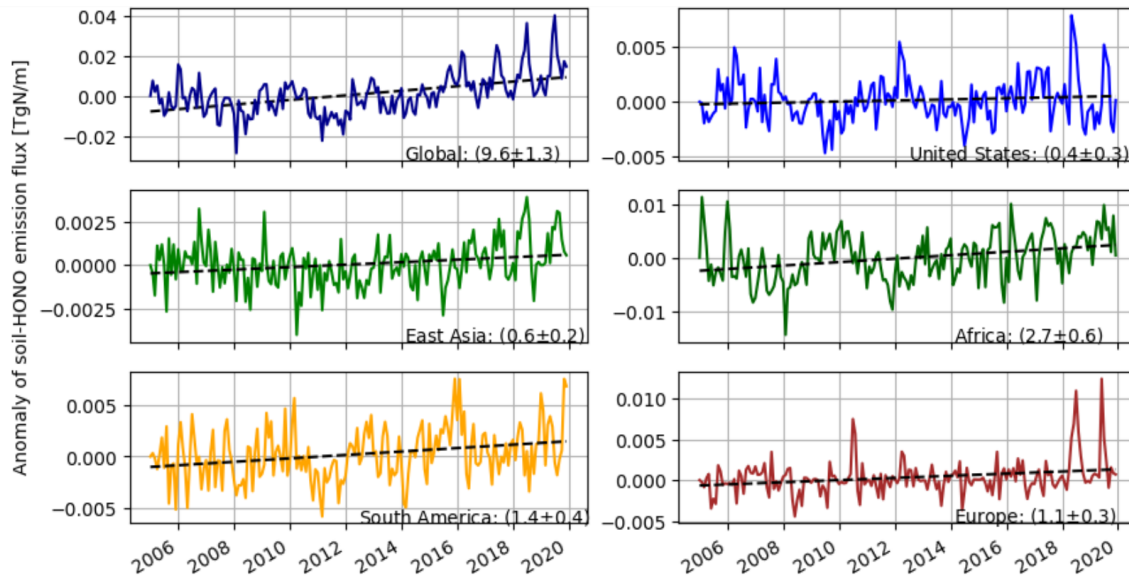
1114

1115 Figure 25: Monthly anomalies of HONO emissions from soil (de-seasonalized). The trend is
1116 given in 10^{-5}, including the uncertainty estimate (2*standard deviation).

3.6.3. Canopy Reduction Factor

1118 Most NO soil emission models (Yienger and Levy, 1995; Hudman et al., 2012) rely on an
1119 empirical canopy reduction scheme which represents loss processes in plants as the diffusion of
1120 NO_2 through the stomata and direct deposition to the cuticle. In particular, a large fraction of
1121 NO_x (and peroxyacyl nitrate) loss during the night may be only explainable by non-stomatal
1122 processes (Delaria et al., 2020b). Mechanistically, the canopy reduction can be described by an
1123 efficient NOx deposition to plants. Thus, Delaria et al. (2020a) points out that models already
1124 represent the uptake by vegetation and do not need to use a canopy reduction scheme. The
1125 potential change of NO soil emissions is shown by employing the global model
1126 ECHAM/MESSy (1°x1°) with an explicit trace gas uptake at stomata and cuticle (Emmerichs et
1127 al., 2021) for two different seasons in 2005 and 2006. Removing the canopy reduction factor in
1128 the model leads to a HC increase of soil NO emissions highest over tropical forests ([Figure 26](#)).
1129 The temporal variation follows the vegetational growth as in the Northern Hemisphere summer
1130 50% higher emissions occur. These findings are reasonable as Hudman et al. (2012) estimated
1131 that the canopy reduction scheme overall lowers the NO emissions by 10-15% in grasslands and
1132 up to 85% over forests (GEOS-Chem at 2°×2.5° in 2006). Consequently, improper accounting
1133 for the canopy reduction factor may imply a strong underestimation of the soil-N in densely
1134 forested regions and globally by about 31% (2005-2006).

1135
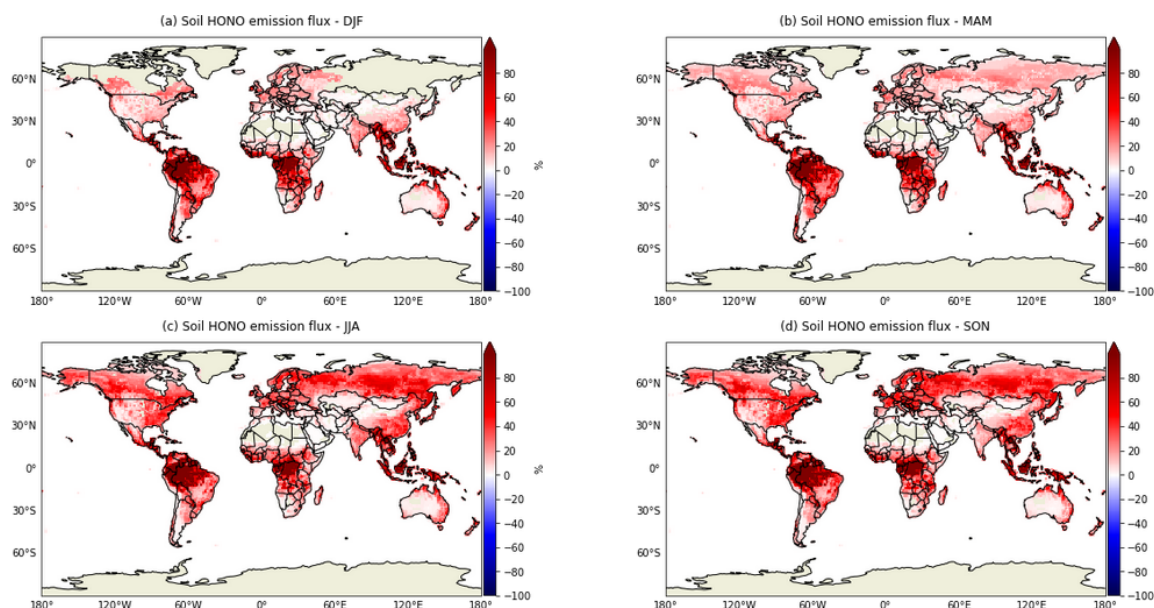
1136

1137 Figure 26: Relative difference Canopy Reduction soil HONO

1138

1139 ### 3.6.4. Projections of soil NO and variability in different climates

1140 The future land use is predicted to change as a consequence of the growing demand for
1141 nutrition and biofuels which implies an increasing use of fertilizer. Consequently, NO soil
1142 emissions are estimated to rise by ~28% during the century to 11.5 TgN/yr at the end of 2100
1143 (Fowler et al., 2015). Similarly, Liu et al. (2021) estimate an increasing soil NO emission of 8.9
1144 TgN/yr by the year 2050 due to intensive nitrification processes.

1145 An increase of LAI by 10 %, in contrast, would lead to 1% lower emissions. In addition, several
1146 responses are expected from the changing climate. In fact, the 1°C higher temperature would
1147 cause ~5% increase in emissions (Weng et al., 2020). Following the future ('medium high')
1148 climate scenario RCP6.0 (Representative Concentration Pathway, 6 W/m2 radiative forcing until
1149 2500, stabilization after 2150) used for the CMIP5 (Climate Model Intercomparison Project)
1150 simulations. Jöckel et al. (2016) suggest an increase of ~15 % in soil NO emissions due to
1151 increasing soil temperature (an increase of soil microbes) from present-day (2010) until 2100.
1152 However, the most significant implications for large-scale denitrification activity are changing
1153 rainfall and the regional hydrological cycles (Fowler et al., 2015). In general, soil NO_x will play
1154 a more important role in the global budget in the troposphere due to the decreasing
1155 anthropogenic emissions in the future. Therefore, increasing NOx-soil emissions may slow down
1156 the decrease of O3 in response to declining anthropogenic emissions (Wu et al. 2022).

1157

1158 ### 3.6.5. Next steps with biogeochemical models implemented in ESMs

1159 Uncertainties of modeling soil nitrogen emissions are associated with the model input and
1160 parameters (Wang and Chen 2012). Process-based biogeochemical models which also consider
1161 the complexity of soil emission processes as DNDC (Denitrification–Decomposition) are needed
1162 (Li et al., 2011). The capability to represent interactive biogeochemical cycles allows for
1163 instance for the online calculation of crop nutrition from soil. Also, a model like CLM5
1164 distinguishes between natural and agricultural soils which more accurately predicts the fertilizer

1165 usage (Fung et al., 2022). Resolving the soil and litter biogeochemical dynamics vertically, in
1166 addition, lead to a more efficient retainment and recycling of N by the ecosystem (Koven et al.,
1167 2013). However, these models should be calibrated to multiple sites (Wang et al., 2019) which is
1168 limited by the availability of measurement data, especially when it comes to global modeling.

1169

4. Conclusion

1171 In this article, we investigate temporal and spatial trends and variability of tropospheric ozone in
1172 relation to its precursors using satellite products, ozonesonde measurements, and model
1173 simulations. Our results show that ozone has positive trends at all latitudes and column depths
1174 regardless of the tropopause height within ±100 hPa. The positive trends in the 30-60ºN band are
1175 due to increasing trends over Canada and Alaska and are slightly offset by the small negative
1176 trends over the northeastern US and Europe. The lower trends in the bands 30-60ºN and 30-60ºS
1177 are due to the offsetting impact of negative trends over Eastern US and Europe in the north, and
1178 Australia and South Africa in the south, respectively. The decreasing trends of $TrC-O_3$ over parts
1179 of the northeastern US and Europe are likely due to the decreasing trend of $TrC-NO_2$, which is
1180 due to the effective measures applied over the last two decades to mitigate air pollution in these
1181 regions. TrC-HCHO trends are decreasing in the Eastern US, some parts of northern and western
1182 Africa, and western and northern Europe, and increasing in South Asia, central Africa, northern
1183 Australia, and Brazil. TrC-HCHO trends are consistent with that of $TrC-O_3$ over northeastern US
1184 and Europe. Simulated O_3 and its precursors are in good agreement with satellite measurements.
1185 Considering different latitude bands, the $TrC-O_3$ highest trends are simulated between 30º S and
1186 60º N, consistent with calculated trends based on satellite observations. The middle and upper
1187 troposphere make the largest contributions to the simulated $TrC-O_3$ trend globally, with large
1188 contributions from the upper troposphere driving the simulated $TrC-O_3$ trend at 30°S-30°N and
1189 counteracting the negative $TrC-O_3$ trend in the southern midlatitudes.

1190 We have also shed light on NO_X lightning and its relation to ozone trends. LNO_x is responsible
1191 for the largest fraction of upper tropospheric ozone in the tropics year-round and in the mid-
1192 latitudes in summer. Ozone Radiative forcing is due to the ozone near the tropopause. An
1193 increasing trend of LNO_x at Arctic latitudes has been noted, as that region rapidly warms.
1194 However, future trends in flash rate are uncertain, with conflicting predictions coming from
1195 models with differing flash rate parameterizations. Soil HONO emissions had their highest
1196 positive monthly anomalies mainly in the 5 most recent years which is likely due to the more
1197 frequent heat wave occurrence, e.g. in Europe and North America. Soil HONO trends are highest
1198 in Africa accounting for ~30% of the global anomaly. Soil NO_x emissions could play an
1199 important role in the tropospheric NO_x global budget due to the decreasing anthropogenic
1200 emissions in the future. Therefore, the expected increase in NO_x-soil emissions may slow down
1201 the decrease of O_3 in response to declining anthropogenic emissions. Overall, this study
1202 presented a comprehensive overview of tropospheric ozone trends in relation to its precursors in
1203 different spatial and temporal scales.

1204 Competing interests: At least one of the (co-)authors is a member of the editorial board of
1205 Atmospheric Chemistry and Physics

1206 Author contribution: YE led the conceptualization, writing, and review of the article, JZ led the
1207 OMI ozone satellite product and data analysis, SS led the GEOS 5 GMI data analysis, HP led the
1208 sections on HCHO, NO2, HCHO/NO2 data analysis and contributed to the CO analyses, KM led
1209 the comparison of different satellite products, KP lead the lightning NOx section, HW and RB

1210 contributed to the CO analysis, DT and TE led the section on HONO soil emission, all authors
1211 contribute to the writing and review of the article.

1212

1213 **Acknowledgment**

1214   This study was partially funded by the NSF AGS, grant number 1900795, USF Creative
1215 Scholarship Grant 2022. A part of the research was conducted at the Jet Propulsion Laboratory,
1216 California Institute of Technology, under a contract with NASA. HP has received funding from
1217 the Ministerio de Ciencia e Innovación through the MITIGATE project (grant no. PID2020-
1218 113840RA-I00 funded by MCIN/AEI/10.13039/501100011033) and the Ramon y Cajal grant
1219 (RYC2021-034511-I, MCIN / AEI / 10.13039/501100011033 and European Union
1220 NextGenerationEU/PRTR). The GEOS-GMI simulation was supported by the NASA's Making
1221 Earth System Data Records for Use in Research Environments (MEaSUREScs) program and the
1222 high-performance computing resources for GEOS-GMI were provided by the NASA Center for
1223 Climate Simulation (NCCS).

1224 **5.   References**

1225 Allen, D., Pickering, K., Duncan, B., and Damon, M.: Impact of lightning NO emissions on
1226   North American photochemistry as determined using the Global Modeling Initiative
1227   (GMI) model, J. Geophys. Res.,115, D22301, doi:10.1029/2010JD014062, 2010.

1228 Allen, D. J., Pickering, K. E., Pinder, R. W., Henderson, B. H., Appel, K. W., and Prados, A.:
1229   Impact of lightning-NO on eastern United States photochemistry during the summer
1230   of 2006 as determined using the CMAQ model, Atmos. Chem. Phys., 12, 1737-1758,
1231   doi:10.5194/acp-12-1737-2012, 2012.

1232 Allen, D. J., Pickering, K. E., Lamsal, L., Mach, D., Quick, M. G., Lapierre, J., Janz, S.,
1233   Koshak, W., Kowalewski, M. & Blakeslee, R.: Observations of Lightning NO_x
1234   production from GOES-R Post Launch Test Field Campaign Flights, J. Geophys.
1235   Res., 126 (8), https://doi.org/10.1029/2020JD033769, 2021a.

1236 Allen, D. J., Pickering, K. E., Bucsela, E., van Geffen, J., Lapierre, J., Koshak, W., & Eskes,
1237   H.: Observations of Lightning NOx production from Tropospheric Ozone Monitoring
1238   Instrument Case Studies over the United States, J. Geophys. Res., 126 (10),
1239   https://doi.org/10.1029/2020JD034174, 2021b.

1240 Allen, D., J., Pickering, K. E., Bucsela, E., Krotkov, N., and Holzworth, R.: Lightning NO_x
1241   Production in the Tropics as Determined Using OMI NO_2 Retrievals and WWLLN
1242   Stroke Data, J. Geophys. Res., https://doi.org/10.1029/2018JD029824, 2019.

1243 Apel, E. C., J. R. Olson, J. H. Crawford, R. S. Hornbrook, A. J. Hills, C. A. Cantrell, L. K.
1244   Emmons, D. J. Knapp, S. Hall, R. L. Mauldin III, A. J. Weinheimer, A. Fried, D. R.
1245   Blake, J. D. Crounse, J. M. St. Clair, P. O. Wennberg, G. S. Diskin, H. E. Fuelberg,
1246   A. Wisthaler, T. Mikoviny, W. Brune, and Riemer, D.:Impact of the deep convection
1247   of isoprene and other reactive trace species on radicals and ozone in the upper
1248   troposphere, Atmos. Chem. Phys., 12, 1135–1150, www.atmos-chem-
1249   phys.net/12/1135/2012/doi:10.5194/acp-12-1135-2012, 2012.

1250 Apel, E. C., et al.: Upper tropospheric ozone production from lightning NOx-impacted
1251   convection: Smoke ingestion case study from the DC3 campaign, J. Geophys. Res.
1252   Atmos., 120, doi:10.1002/2014JD022121, 2015.

Archibald, A.T., et al.: Tropospheric Ozone Assessment Report: A critical review of changes in the tropospheric ozone burden and budget from 1850 to 2100. Elem Sci Anth, 8: 1. DOI: https://doi.org/10.1525/elementa.2020.034, 2020.

ASDC, MOPITT CO gridded monthly means (Near and Thermal Infrared Radiances) V009 [Data set]. NASA Langley Atmospheric Science Data Center DAAC. Retrieved from https://doi.org/10.5067/TERRA/MOPITT/MOP03JM.009, 2024.

Barret, B., De Mazière, M., and Mahieu, E.: Ground-based FTIR measurements of CO from the Jungfraujoch: characterisation and comparison with in situ surface and MOPITT data, Atmos. Chem. Phys., 3, 2217–2223, https://doi.org/10.5194/acp-3-2217-2003, 2003.

Bauwens, M.; Compernolle, S.; Stavrakou, T.; Müller, J.; Gent, J.; Eskes, H.; Levelt, P.F.; van der A, R.; Veefkind, J.P.; Vlietinck, J.; et al. Impact of Coronavirus Outbreak on NO2 Pollution Assessed Using TROPOMI and OMI Observations. Geophys. Res. Lett., 47, 2020.

Beirle, S., Huntrieser, H., and Wagner, T.: Direct satellite observation of lightning-produced NO_x, Atmos. Chem. Phys., 10, 10965–10986, https://doi.org/10.5194/acp-10-10965-2010, 2010.

Boersma, K., Eskes, H., Richter, A., De Smedt, I., Lorente, A., Beirle, S., Van Geffen, J., Peters, E., Van Roozendael, M., and Wagner, T.: QA4ECV NO_2 tropospheric and stratospheric vertical column data from OMI (Version 1.1) (data set), Royal Netherlands Meteorological Institute (KNMI), https://doi.org/10.21944/qa4ecv-no2-omi-v1.1, 2017a.

Boersma, K., Eskes, H., Richter, A., De Smedt, I., Lorente, A., Beirle, S., Van Geffen, J., Peters, E., Van Roozendael, M., and Wagner, T.: QA4ECV NO_2 tropospheric and stratospheric vertical column data from GOME-2 (Version 1.1) (data set), Royal Netherlands Meteorological Institute (KNMI), https://doi.org/10.21944/qa4ecv-no2-gome2a-v1.1, 2017b.

Boersma, K., Eskes, H., Richter, A., De Smedt, I., Lorente, A., Beirle, S., Van Geffen, J., Peters, E., Van Roozendael, M., and Wagner, T.: QA4ECV NO_2 tropospheric and stratospheric vertical column data from SCIAMACHY (Version 1.1) (data set), Royal Netherlands Meteorological Institute (KNMI), https://doi.org/10.21944/qa4ecv-no2-scia-v1.1, 2017c.

Boersma, K. F., Eskes, H. J., Richter, A., De Smedt, I., Lorente, A., Beirle, S., van Geffen, J. H. G. M., Zara, M., Peters, E., Van Roozendael, M., Wagner, T., Maasakkers, J. D., van der A, R. J., Nightingale, J., De Rudder, A., Irie, H., Pinardi, G., Lambert, J.-C., and Compernolle, S. C.: Improving algorithms and uncertainty estimates for satellite NO2 retrievals: results from the quality assurance for the essential climate variables (QA4ECV) project, Atmos. Meas. Tech., 11, 6651–6678, https://doi.org/10.5194/amt-11-6651-2018, 2018.

Brune, W. H., et al.: Atmospheric oxidation in the presence of clouds during the Deep

Convective Clouds and Chemistry (DC3) study, Atmos. Chem. Phys., 18, 14493–14510, 2018, https://doi.org/10.5194/acp-18-14493-2018, 2018.

Bruning, E. C. & Thomas, R. J.: Lightning channel length and flash energy determined from moments of the flash area distribution, J. Geophys. Res. Atmos., 120, 8925–8940, doi:10.1002/2015JD023766, 2015.

Buchholz, R.R.; Deeter, M.N.;Worden, H.M.; Gille, J.; Edwards, D.P.; Hannigan, J.W.; Jones, N.B.; Paton-Walsh, C.; Griffith, D.W.T.; Smale, D.; et al.: Validation of MOPITT carbon monoxide using ground-based Fourier transform infrared spectrometer data from NDACC. Atmos. Meas. Tech. 10, 1927–1956, 2017.

Buchholz, R. R., Worden, H. M., Park, M., Francis, G., Deeter, M. N., Edwards, D. P., Emmons, L. K., Gaubert, B., Gille, J., Martinez-Alonso, S., Tang, W., Kumar, R., Drummond, J. R., Clerbaux, C., George, M., Coheur, P.-F., Hurtmans, D., Bowman, K. W., Luo, M., Payne, V. H., Worden, J. R., Chin, M., Levy, R. C., Warner, J., Wei, Z., and Kulawik, S. S.: Air pollution trends measured from Terra: CO and AOD over industrial, fire-prone, and background regions, Remote Sens. Environ., 256, 112275, https://doi.org/10.1016/j.rse.2020.112275, 2021.

Bucsela, E. J., K. E. Pickering, T. L. Huntemann, R. C. Cohen, A. Perring, J. F. Gleason, R. J. Blakeslee, R. I. Albrecht, R. Holzworth, J. P. Cipriani, D. Vargas-Navarro, I. Mora-Segura, A. Pacheco-Hernández, Laporte-Molina, S.: Lightning-generated NO_x seen by OMI during NASA's TC^4 experiment, J. Geophys. Res., 115, D00J10, doi:10.1029/2009JD013118, 2010.

Bucsela, E., Pickering, K. E., Allen, D., Holzworth, R., and Krotkov, N.: Midlatitude lightning NO_x Production Efficiency Inferred from OMI and WWLLN Data, J. Geophys. Res., https://doi.org/10.1029/2019JD030561, 2019.

Canadell, J.G., P.M.S. Monteiro, M.H. Costa, L. Cotrim da Cunha, P.M. Cox, A.V. Eliseev, S. Henson, M. Ishii, S. Jaccard, C. Koven, A. Lohila, P.K. Patra, S. Piao, J. Rogelj, S. Syampungani, S. Zaehle, and K. Zickfeld: Global Carbon and other Biogeochemical Cycles and Feedbacks. In Climate Change 2021: The Physical Science Basis. Contribution of Working Group I to the Sixth Assessment Report of the Intergovernmental Panel on Climate Change [Masson-Delmotte, V., P. Zhai, A. Pirani, S.L. Connors, C. Péan, S. Berger, N. Caud, Y. Chen, L. Goldfarb, M.I. Gomis, M. Huang, K. Leitzell, E. Lonnoy, J.B.R. Matthews, T.K. Maycock, T. Waterfield, O. Yelekçi, R. Yu, and B. Zhou (eds.)]. Cambridge University Press, Cambridge, United Kingdom and New York, NY, USA, pp. 673–816, doi: 10.1017/9781009157896.007, 2021.

Cazorla, M. and Herrera, E.: An ozonesonde evaluation of spaceborne observations in the Andean tropics, Sci Rep, 12, https://doi.org/10.1038/s41598-022-20303-7, 2022.

Chang K-L, Petropavlovskikh I, Cooper OR, Schultz MG, Wang T. Regional trend analysis of surface ozone observations from monitoring networks in eastern North America, Europe and East Asia. Elem Sci Anth., 5:50. DOI: 10.1525/elementa.243, 2017.

Chang, K.-L., Cooper, O. R., Gaudel, A., Petropavlovskikh, I., and Thouret, V.: Statistical regularization for trend detection: an integrated approach for detecting long-term trends from sparse tropospheric ozone profiles, Atmos. Chem. Phys., 20, 9915–9938, https://doi.org/10.5194/acp-20-9915-2020, 2020.

Chang, K.-L., Cooper, O. R., Gaudel, A., Allaart, M., Ancellet, G., Clark, H., et al.: Impact of the COVID-19 economic downturn on tropospheric ozone trends: An uncertainty

weighted data synthesis for quantifying regional anomalies above western North America and Europe. AGU Advances, 3, e2021AV000542. https://doi.org/10.1029/2021AV000542, 2022.

Chang K-L, Martin G. Schultz, Gerbrand Koren, Selke, N.: Guidance note on best statistical practices for TOAR analyses, https://doi.org/10.48550/arXiv.2304.14236, 2023.

Chang, K.-L., Cooper, O. R., Gaudel, A., Petropavlovskikh, I., Effertz, P., Morris, G., and McDonald, B. C.: Technical note: Challenges of detecting free tropospheric ozone trends in a sparsely sampled environment, EGUsphere [preprint], https://doi.org/10.5194/egusphere-2023-2739, 2024.

Chen, Z., Jane Liu, Xiushu Qie, Xugeng Cheng, Mengmiao Yang, Lei Shu, Zang, Z.: Stratospheric influence on surface ozone pollution in China, Nature Communications, 10.1038/s41467-024-48406-x, **15**, 1, 2024.

Christiansen, A., Mickley, L. J., Liu, J., Oman, L. D., and Hu, L.: Multidecadal increases in global tropospheric ozone derived from ozonesonde and surface site observations: can models reproduce ozone trends?, Atmos Chem Phys, 22, 14751–14782, https://doi.org/10.5194/acp-22-14751-2022, 2022.

Cooper, O. R., Schultz, M. G., Schröder, S., Chang, K. L., Gaudel, A., Benítez, G. C., Cuevas, E., Fröhlich, M., Galbally, I. E., Molloy, S., Kubistin, D., Lu, X., McClure-Begley, A., Nédélec, P., O'Brien, J., Oltmans, S. J., Petropavlovskikh, I., Ries, L., Senik, I., Sjöberg, K., Solberg, S., Spain, G. T., Spangl, W., Steinbacher, M., Tarasick, D., Thouret, V., and Xu, X.: Multi-decadal surface ozone trends at globally distributed remote locations, Elementa, 8, https://doi.org/10.1525/elementa.420, 2020.

Cummings, K. A., T. L. Huntemann, and E. Pickering, K.: Cloud-resolving chemistry simulation of a Hector thunderstorm, Atmos. Chem. Phys., 13(5), 2757-2777, doi:10.5194/acp-13-2757, 2013.

DeCaria, A., K. Pickering, G. Stenchikov, J. Scala, J. Stith, J. Dye, B. Ridley, and Laroche, P.: A cloud-scale model study of lightning-generated NO_x in an individual thunderstorm during STERAO-A, J. Geophys. Res., 105, 11,601-11,616, 2000.

DeCaria, A. J., K. E. Pickering, G. L. Stenchikov, and E. Ott, L.: Lightning-generated NOx and its impact on tropospheric ozone production: A three-dimensional modeling study of a STERAO-A thunderstorm, J. Geophys. Res., 110, D14303, doi:10.1029/2004JD005556, 2005.

Deeter, M., Francis, G., Gille, J., Mao, D., Martínez-Alonso, S., Worden, H., Ziskin, D., Drummond, J., Commane, R., Diskin, G., and McKain, K.: The MOPITT Version 9 CO product: sampling enhancements and validation, Atmos. Meas. Tech., 15, 2325–2344, https://doi.org/10.5194/amt-15-2325-2022, 2022.

De Smedt, I., Theys, N., Yu, H., Danckaert, T., Lerot, C., Compernolle, S., Van Roozendael, M., Richter, A., Hilboll, A., Peters, E., Pedergnana, M., Loyola, D., Beirle, S., Wagner, T., Eskes, H., van Geffen, J., Boersma, K. F., and Veefkind, P.: Algorithm theoretical baseline for formaldehyde retrievals from S5P TROPOMI and from the QA4ECV project, Atmos. Meas. Tech., 11, 2395–2426, https://doi.org/10.5194/amt-11-2395-2018, 2018

Duncan, B. N., Strahan, S. E., Yoshida, Y., Steenrod, S. D., and Livesey, N.: Model study of the cross-tropopause transport of biomass burning pollution, Atmos. Chem. Phys., 7, 3713–3736, https://doi.org/10.5194/acp-7-3713-2007, 2007.

Elguindi, N., Granier, C., Stavrakou, T., Darras, S., Bauwens, M., Cao, H., Chen, C., Denier van der Gon, H. A. C., Dubovik, O., Fu, T. M., Henze, D. K., Jiang, Z., Keita, S., Kuenen, J. J. P., Kurokawa, J., Liousse, C., Miyazaki, K., Müller, J. F., Qu, Z., Solmon, F., and Zheng, B.: Intercomparison of Magnitudes and Trends in Anthropogenic Surface Emissions From Bottom-Up Inventories, Top-Down Estimates, and Emission Scenarios, Earths Future, 8, e2020EF001520, https://doi.org/10.1029/2020EF001520, 2020.

Elshorbany, Y. F., Kurtenbach, R., Wiesen, P. Lissi, E., Rubio, M., Villena, G., Gramsch, E., Rickard, A. R., Pilling, M. J., Kleffmann. J.: Oxidation capacity of the city air of Santiago, Chile, Atmospheric Chemistry and Physics, **9**, 2257-2273, 2009.

Elshorbany, Y. F, Barnes, I., Becker, K. H, Kleffmann, J., and Wiesen, P.: Sources and Cycling of Tropospheric Hydroxyl Radicals-An Overview, Zeitschrift für Physikalische Chemie, 224, 967-987, DOI:10.1524/zpch.2010.6136, 2010.

Elshorbany, Y. F., Kleffmann, J., Hofzumahaus, A., Kurtenbach, R., Wiesen, P., Dorn,H.-P., Schlosser, E., Brauers, T., Fuchs, H., Rohrer, F., Wahner, A., Kanaya, Y., Yoshino, A., Nishida, S., Kajii, Y., Martinez, M., Rudolf, M., Harder, H., Lelieveld, J., Elste, T., Plass-Dülmer, C., Stange, G., and Berresheim, H.: HO_x Budgets during HOxComp: a Case Study of HO_x Chemistry under NO_x limited Conditions, J. Geophys. Res., 117, D03307, doi: 10.1029/2011JD017008, 2012.

Elshorbany, Y. F., Crutzen, P. J., Steil, B., Pozzer, A., Tost, H., and Lelieveld, J.: Global and regional impacts of HONO on the chemical composition of clouds and aerosols, Atmos. Chem. Phys., 14, 1167–1184, https://doi.org/10.5194/acp-14-1167-2014, 2014.

Elshorbany, Y. F.: Hannah C. Kapper; Jerald R. Ziemke; A. Parr, S.: The Status of Air Quality in the United States During the COVID-19 Pandemic: A Remote Sensing Perspective . Remote Sensing, doi:10.3390/rs13030369, 2021.

Fadnavis, S., Sagalgile, A., Sonbawne, S., Vogel, B., Peter, T., Wienhold, F. G., Dirksen, R., Oelsner, P., Naja, M., and Müller, R.: Comparison of ozonesonde measurements in the upper troposphere and lower Stratosphere in Northern India with reanalysis and chemistry-climate-model data, Sci Rep, 13, 7133, https://doi.org/10.1038/s41598-023-34330-5, 2023.

Fehr, T., H. Höller, and Huntrieser, H.: Model study on production and transport of lightning-produced NOx in a EULINOX supercell storm, J. Geophys. Res., 109, D09102, doi:10.1029/2003JD003935, 2004.

Finney. D. L., R. M. Doherty, O. Wild, H. Huntrieser, H. C. Pumphrey, and M. Blyth, A.: Using cloud ice flux to parameterize large-scale lightning, Atmos. Chem. Phys., 14, 12665–12682, www.atmos-chem-phys.net/14/12665/2014/ doi:10.5194/acp-14-12665-2014, 2014.

Finney, D. L., R. M. Doherty, O. Wild, P. J. Young, and Butler, A.: Response of lightning NOx emissions and ozone production to climate change: Insights from the

Atmospheric Chemistry and Climate Model Intercomparison Project, Geophys. Res. Lett., 43, 5492–5500, doi:10.1002/2016GL068825, 2016.

Finney, D. L., R. M. Doherty, O. Wild, D. S. Stevenson, I. A. MacKenzie, and M. Blyth, A.: A projected decrease in lightning under climate change, Nature Climate Change, 8, 210-213, 2018.

Fiore, A. M., Jacob, D. J., Field, B. D., Streets, D. G., Fernandes, S. D., and Jang, C.: Linking air pollution and climate change: The case for controlling methane, Geophys. Res. Lett., 29, 1919, doi:10.1029/2002GL015601, 2002.

Fiore, A. M., L. W. Horowitz, E. J. Dlugokencky, and J. West, J.: Impact of meteorology and emissions on methane trends, 1990–2004, Geophys. Res. Lett., 33, L12809, doi:10.1029/2006GL026199, 2006.

Fisher, B. L., Lamsal, L. N., Fasnacht, Z., Oman, L. D., Joiner, J., Krotkov, N. A., ... & Yang, E. S.: Revised estimates of NO_2 reductions during the COVID-19 lockdowns using updated TROPOMI NO_2 retrievals and model simulations. Atmospheric Environment, 326, 120459, 2024.

Fleming, Z.L., Doherty, R.M., von Schneidemesser, E., Malley, C.S., Cooper, O.R., Pinto, J.P., Colette, A., Xu, X., Simpson, D., Schultz, M.G., Lefohn, A.S., Hamad, S., Moolla, R., Solberg, S. and Feng, Z.: Tropospheric Ozone Assessment Report: Present-day ozone distribution and trends relevant to human health, Elem Sci Anth, 6(1), p.12. DOI: 10.1525/elementa.73, 2018.

Flynn, C. M., K. E. Pickering, J. H. Crawford, A. Weinheimer, K. L. Thornhill, C. Loughner, Lee, P.: Variability of O_3 and NO_2 profile shapes during DISCOVER-AQ: Implications for satellite observations and comparisons to model-simulated profiles, Atmos. Environ., 147, 133-156, 2016.

Fortems-Cheiney, A., Chevallier, F., Pison, I., Bousquet, P., Szopa, S., Deeter, M. N., and Clerbaux, C.: Ten years of CO emissions as seen from Measurements of Pollution in the Troposphere (MOPITT), J. Geophys. Res., 116, D05304, https://doi.org/10.1029/2010JD014416, 2011.

Fortems-Cheiney, A., Chevallier, F., Pison, I., Bousquet, P., Saunois, M., Szopa, S., Cressot, C., Kurosu, T. P., Chance, K., and Fried, A.: The formaldehyde budget as seen by a global-scale multi-constraint and multi-species inversion system, Atmos. Chem. Phys., 12, 6699–6721, https://doi.org/10.5194/acp-12-6699-2012, 2012.

Forster, P., T. Storelvmo, K. Armour, W. Collins, J.-L. Dufresne, D. Frame, D.J. Lunt, T. Mauritsen, M.D. Palmer, M. Watanabe, M. Wild, and H. Zhang, 2021: The Earth's Energy Budget, Climate Feedbacks, and Climate Sensitivity. In Climate Change 2021: The Physical Science Basis. Contribution of Working Group I to the Sixth Assessment Report of the Intergovernmental Panel on Climate Change [Masson-Delmotte, V., P. Zhai, A. Pirani, S.L. Connors, C. Péan, S. Berger, N. Caud, Y. Chen, L. Goldfarb, M.I. Gomis, M. Huang, K. Leitzell, E. Lonnoy, J.B.R. Matthews, T.K. Maycock, T. Waterfield, O. Yelekçi, R. Yu, and B. Zhou (eds.)]. Cambridge University Press, 923 Cambridge, United Kingdom and New York, NY, USA, pp. 923–1054, doi:10.1017/9781009157896.009, 2021.

Fullekrug, M. E. Williams, C. Price, S. Goodman, R. Holzworth, K. Virts, and Buechler Sidebar, D.: Lightning, in State of the Climate: 2021, Bull. Amer. Meteor. Soc., 108, S79-S81, doi:10.1175/BAMS-D-22-0092.1, 2022

Fung, K. M., Val Martin, M., and Tai, A. P. K.: Modeling the interinfluence of fertilizer-induced NH3 emission, nitrogen deposition, and aerosol radiative effects using modified CESM2, Biogeosciences, 19, 1635–1655, https://doi.org/10.5194/bg-19-1635-2022, 2022.

Gaubert, B., Emmons, L. K., Raeder, K., Tilmes, S., Miyazaki, K., Arellano Jr., A. F., Elguindi, N., Granier, C., Tang, W., Barré, J., Worden, H. M., Buchholz, R. R., Edwards, D. P., Franke, P., Anderson, J. L., Saunois, M., Schroeder, J., Woo, J.-H., Simpson, I. J., Blake, D. R., Meinardi, S., Wennberg, P. O., Crounse, J., Teng, A., Kim, M., Dickerson, R. R., He, H., Ren, X., Pusede, S. E., and Diskin, G. S.: Correcting model biases of CO in East Asia: impact on oxidant distributions during KORUS-AQ, Atmos. Chem. Phys., 20, 14617–14647, https://doi.org/10.5194/acp-20-14617-2020, 2020.

Gaudel, A., Cooper, O.R., Ancellet, G., Barret, B., Boynard, A., Burrows, J.P., Clerbaux, C., Coheur, P.-F., Cuesta, J., Cuevas, E., Doniki, S., Dufour, G., Ebojie, F., Foret, G., Garcia, O., Granados Muños, M.J., Hannigan, J.W., Hase, F., Huang, G., Hassler, B., Hurtmans, D., Jaffe, D., Jones, N., Kalabokas, P., Kerridge, B., Kulawik, S.S., Latter, B., Leblanc, T., Le Flochmoën, E., Lin, W., Liu, J., Liu, X., Mahieu, E., McClure-Begley, A., Neu, J.L., Osman, M., Palm, M., Petetin, H., Petropavlovskikh, I., Querel, R., Rahpoe, N., Rozanov, A., Schultz, M.G., Schwab, J., Siddans, R., Smale, D., Steinbacher, M., Tanimoto, H., Tarasick, D.W., Thouret, V., Thompson, A.M., Trickl, T., Weatherhead, E., Wespes, C., Worden, H.M., Vigouroux, C., Xu, X., Zeng, G. and Ziemke, J., Tropospheric Ozone Assessment Report: Present-day distribution and trends of tropospheric ozone relevant to climate and global atmospheric chemistry model evaluation, Elem Sci Anth, 6(1), p.39. DOI: 10.1525/elementa.291, 2018.

Gelaro, Ronald, et al.: The modern-era retrospective analysis for research and applications, version 2 (MERRA-2), Journal of climate 30.14, 5419-5454, 2017.

Ghude, S.D., Van der A, R.J., Beig, G., Fadnavis, S., Polade, S.D.: Satellite derived trends in NO2 over the major global hotspot regions during the past decade and their inter-comparison. Environ. Pollut. 157, 1873–1878. https://doi.org/10.1016/j.envpol.2009.01.013, 2009.

Glotfelty, T., Zhang, Y., Karamchandani, P., and Streets, D. G.: Will the role of intercontinental transport change in a changing climate?, Atmos. Chem. Phys., 14, 9379–9402, https://doi.org/10.5194/acp-14-9379-2014, 2014.

Gödde, M., Conrad, R. Influence of soil properties on the turnover of nitric oxide and nitrous oxide by nitrification and denitrification at constant temperature and moisture. Biol Fertil Soils 32, 120–128, https://doi.org/10.1007/s003740000247, 2000.

Granier, C., Bessagnet, B., Bond, T., D'Angiola, A., Denier van der Gon, H., Frost, G. J., ... & van Vuuren, D. P.: Evolution of anthropogenic and biomass burning emissions of air pollutants at global and regional scales during the 1980–2010 period. Climatic change, 109, 163-190, 2011.

Grewe, V., Brunner, D., Dameris, M., Grenfell, J. L., Hein, R., Shindell, D., & Staehelin, J.:
Origin and variability of upper tropospheric nitrogen oxides and ozone at northern
mid-latitudes, Atmos. Env., 35, 3421-3433, 2001.

Griffiths, P. T., Murray, L. T., Zeng, G., Shin, Y. M., Abraham, N. L., Archibald, A. T.,
Deushi, M., Emmons, L. K., Galbally, I. E., Hassler, B., Horowitz, L. W., Keeble, J.,
Liu, J., Moeini, O., Naik, V., O'Connor, F. M., Oshima, N., Tarasick, D., Tilmes, S.,
Turnock, S. T., Wild, O., Young, P. J., and Zanis, P.: Tropospheric ozone in CMIP6
simulations, Atmos. Chem. Phys., 21, 4187–4218, https://doi.org/10.5194/acp-21-
4187-2021, 2021.

Gulev, S.K., P.W. Thorne, J. Ahn, F.J. Dentener, C.M. Domingues, S. Gerland, D. Gong,
D.S. Kaufman, H.C. Nnamchi, J. Quaas, J.A. Rivera, S. Sathyendranath, S.L. Smith,
B. Trewin, K. von Schuckmann, and R.S. Vose: Changing State of the Climate
System. In Climate Change 2021: The Physical Science Basis. Contribution of
Working Group I to the Sixth Assessment Report of the Intergovernmental Panel on
Climate Change [Masson-Delmotte, V., P. Zhai, A. Pirani, S.L. Connors, C. Péan, S.
Berger, N. Caud, Y. Chen, L. Goldfarb, M.I. Gomis, M. Huang, K. Leitzell, E.
Lonnoy, J.B.R. Matthews, T.K. Maycock, T. Waterfield, O. Yelekçi, R. Yu, and B.
Zhou (eds.)]. Cambridge University Press, Cambridge, United Kingdom and New
York, NY, USA, pp. 287–422, doi: 10.1017/9781009157896.004, 2021.

Hoor, P., Borken-Kleefeld, J., Caro, D., Dessens, O., Endresen, O., Gauss, M., Grewe, V.,
Hauglustaine, D., Isaksen, I. S. A., Jöckel, P., Lelieveld, J., Myhre, G., Meijer, E.,
Olivie, D., Prather, M., Schnadt Poberaj, C., Shine, K. P., Staehelin, J., Tang, Q., van
Aardenne, J., van Velthoven, P., and Sausen, R.: The impact of traffic emissions on
atmospheric ozone and OH: results from QUANTIFY, Atmos. Chem. Phys., 9, 3113–
3136, https://doi.org/10.5194/acp-9-3113-2009, 2009.

Holzworth, R. H., Brundell, J. B., McCarthy, M. P., Jacobson, A. R., Rodger, C. J., &
Anderson, T. S.: Lightning in the Arctic. Geophysical Research Letters, 48,
e2020GL091366, https://doi.org/10.1029/2020GL091366, 2021.

Hov, Ö., Hesstvedt, E. & Isaksen, I. Long-range transport of tropospheric ozone. Nature **273**,
341–344. https://doi.org/10.1038/273341a0, 1978.

Hubert, D., Heue, K.-P., Lambert, J.-C., Verhoelst, T., Allaart, M., Compernolle, S., Cullis,
P. D., Dehn, A., Félix, C., Johnson, B. J., Keppens, A., Kollonige, D. E., Lerot, C.,
Loyola, D., Maata, M., Mitro, S., Mohamad, M., Piters, A., Romahn, F., Selkirk, H.
B., da Silva, F. R., Stauffer, R. M., Thompson, A. M., Veefkind, J. P., Vömel, H.,
Witte, J. C., and Zehner, C.: TROPOMI tropospheric ozone column data: geophysical
assessment and comparison to ozonesondes, GOME-2B and OMI, Atmos Meas Tech,
14, 7405–7433, https://doi.org/10.5194/amt-14-7405-2021, 2021.

Hudman, R. C., Moore, N. E., Mebust, A. K., Martin, R. V., Russell, A. R., Valin, L. C., and
Cohen, R. C.: Steps towards a mechanistic model of global soil nitric oxide
emissions: implementation and space based-constraints, Atmos. Chem. Phys., 12,
7779–7795, https://doi.org/10.5194/acp-12-7779-2012, 2012.

Huntrieser, H., U. Schumann, H. Schlager, H. Höller, A. Giez, H.-D. Betz, D. Brunner, C.
Forster, O. Pinto Jr., and Calheiros, R.: Lightning activity in Brazilian thunderstorms

during TROCCINOX: Implications for NOx production, Atmos. Chem. Phys., 8, 21–953, 2008.

Huntrieser, H., H. Schlager, M. Lichtenstern, P. Stock, T. Hamburger, H. Hoeller, K. Schmidt, H.-D. Betz, A. Ulanovsky, and Ravegnani, F.: Mesoscale convective systems observed during AMMA and their impact on the NOx and O3 budget over West Africa, Atmos. Chem. Phys., 11, 2503–2536, www.atmos-chem-phys.net/11/2503/2011, doi:10.5194/acp-11-2503-2011, 2011.

Ichoku, C., & Ellison, L.: Global top-down smoke-aerosol emissions estimation using satellite fire radiative power measurements. Atmospheric Chemistry and Physics, 14(13), 6643-6667, 2014.

IPCC, AR5, chrome-extension://efaidnbmnnnibpcajpcglclefindmkaj/https://www.ipcc.ch/site/assets/uploads/2018/03/TAR-06.pdf, 2018.

Isaksen, I.S.A.; Berntsen, T.K.; Dalsøren, S.B.; Eleftheratos, K.; Orsolini, Y.; Rognerud, B.; Stordal, F.; Søvde, O.A.; Zerefos, C.; Holmes, C. D.: Atmospheric Ozone and Methane in a Changing Climate. Atmosphere, 5, 518-535. https://doi.org/10.3390/atmos5030518, 2014.

Itahashi, S., Mathur, R., Hogrefe, C., Napelenok, S. L., and Zhang, Y.: Modeling stratospheric intrusion and trans-Pacific transport on tropospheric ozone using hemispheric CMAQ during April 2010 – Part 2: Examination of emission impacts based on the higher-order decoupled direct method, Atmos. Chem. Phys., 20, 3397–3413, https://doi.org/10.5194/acp-20-3397-2020, 2020.

Janssens-Maenhout, G., Pagliari, V., Guizzardi, D., & Muntean, M.: Global emission inventories in the emission database for global atmospheric research (EDGAR)–Manual (I). Gridding: EDGAR emissions distribution on global gridmaps, Publications Office of the European Union, Luxembourg, 775, 2013.

Jin, X., Fiore, A., Boersma, K. F., Smedt, I. D., and Valin, L.: Inferring Changes in Summertime Surface Ozone–NOx –VOC Chemistry over U.S. Urban Areas from Two Decades of Satellite and Ground-Based Observations, Environmental Science Technology, 54, 6518–6529, https://doi.org/10.1021/acs.est.9b07785, 2020.

J. Jung, Y. Choi, S. Mousavinezhad, D. Kang, J. Park, A. Pouyaei, et al.: Changes in the ozone chemical regime over the contiguous United States inferred by the inversion of NOx and VOC emissions using satellite observation, Atmos. Res., 270, 106076, https://doi.org/10.1016/j.atmosres.2022.106076, 2022.

Kang, D., K. Foley, R. Mathur, S. Roselle, K. Pickering, and D. Allen, Lightning NO_X Production in CMAQ Part II – Performance Evaluations, Geosci. Model Devel., 12, 4409–4424, https://doi.org/10.5194/gmd-12-4409-2019, 2019.

Kaynak, B., Hu, Y., Martin, R. V., Russell, A. G., Choi, Y., & Wang, Y.: The effect of lightning NOx production on surface ozone in the continental United States, Atmospheric Chemistry and Physics, 8, 5151–5159, 2008.

Koven, C. D., Riley, W. J., Subin, Z. M., Tang, J. Y., Torn, M. S., Collins, W. D., Bonan, G. B., Lawrence, D. M., and Swenson, S. C.: The effect of vertically resolved soil

biogeochemistry and alternate soil C and N models on C dynamics of CLM4, Biogeosciences, 10, 7109–7131, https://doi.org/10.5194/bg-10-7109-2013, 2013.

Kitagawa, N.: Long-term variations in thunder-day frequencies in Japan, J. Geophys. Res., 94, 13 183–13 189, https://doi.org/10.1029/JD094iD11p13183, 1989.

Koehler, T. L.: Cloud-to-Ground Lightning Flash Density and Thunderstorm Day Distributions over the Contiguous United States Derived from NLDN Measurements: 1993–2018, Mon. Weather Rev., DOI: 10.1175/MWR-D-19-0211.1, 2020

Kopacz, M., Jacob, D. J., Fisher, J. A., Logan, J. A., Zhang, L., Megretskaia, I. A., Yantosca, R. M., Singh, K., Henze, D. K., Burrows, J. P., Buchwitz, M., Khlystova, I., McMillan, W. W., Gille, J. C., Edwards, D. P., Eldering, A., Thouret, V., and Nedelec, P.: Global estimates of CO sources with high resolution by adjoint inversion of multiple satellite datasets (MOPITT, AIRS, SCIAMACHY, TES), Atmos. Chem. Phys., 10, 855–876, https://doi.org/10.5194/acp-10-855-2010, 2010.

Koshak, W., Peterson, H., Biazar, A., Khan, M., & Wang, L.: The NASA Lightning Nitrogen Oxides Model (LNOM): application to air quality modeling. Atmospheric Research, 135, 363-369, 2014.

Koshak, W.J., Cummins, K.L., Buechler, D.E., Vant-Hull, B., Blakeslee, R.J., Williams, E.R. and Peterson, H.S.: Variability of CONUS lightning in 2003–12 and associated impacts. Journal of Applied Meteorology and Climatology, **54**, 15–41, https://doi.org/10.1175/JAMC-D-14-0072.1, 2015.

Krizan, P. and Lastovicka, J.: Trends in positive and negative ozone laminae in the Northern Hemisphere, Journal of Geophysical Research: Atmospheres, 110, https://doi.org/https://doi.org/10.1029/2004JD005477, 2005.

Labow, G. J., Ziemke, J. R., McPeters, R. D., Haffner, D. P., and Bhartia, P. K.: A total ozone-dependent ozone profile climatology based on ozonesondes and Aura MLS data, Journal of Geophysical Research: Atmospheres, 120, 2537–2545, https://doi.org/10.1002/2014JD022634, 2015.

Labrador, L. J., Kuhlmann, R. V., and Lawrence, M. G.: The effects of lightning-produced NOx and its vertical distribution on atmospheric chemistry: sensitivity simulations with MATCH-MPIC, Atmos. Chem. Phys., 5, 1815-1834, 2005.

Lacis, A. A., Wuebbles, D. J., and Logan, J. A.: Radiative forcing of climate by changes in the vertical distribution of ozone, J. Geophys. Res., 95, 9971-9982, 1990.

Lamsal, L. N, Duncan, B. N., Yoshida, Y., Krotkov, N. A., Pickering, K. E., Streets, D. G., Zifeng Lu, Z.: U.S. NO2 trends (2005–2013): EPA Air Quality System (AQS) data versus improved observations from the Ozone Monitoring Instrument (OMI), Atmospheric Environment, https://doi.org/10.1016/j.atmosenv.2015.03.055, 2015.

Lapierre, J. L., Laughner, J. L., Geddes, J. A., Koshak, W. J., Cohen, R. C., Pusede, S. E.: Observing U.S. regional variability in lightning NO_2 production rates, J. Geophys. Res., 125 (5), https:/doi.org/10.1029/2019JD031362, 2020.

Lavigne, T., C. Liu, and Liu, N.: How does the trend in thunder days relate to the variation of lightning flash density? J. Geophys. Res. Atmos., 124, 4955–4974, https://doi.org/10.1029/2018JD029920, 2019.

Lefohn, AS, Malley, CS, Smith, L, Wells, B, Hazucha, M, Simon, H, Naik, V, Mills, G,
Schultz, MG, Paoletti, E, De Marco, A, Xu, X, Zhang, L, Wang, T, Neufeld, HS,
Musselman, RC, Tarasick, D, Brauer, M, Feng, Z, Tang, H, Kobayashi, K, Sicard, P,
Solberg, S and Gerosa, G.: Tropospheric ozone assessment report: Global ozone
metrics for climate change, human health, and crop/ecosystem research. Elem Sci
Anth, 6: 28. DOI: 10.1525/elementa.279, 2018.

Lelieveld, J.; Crutzen, P J.: The role of clouds in tropospheric photochemistry, 12(3), 229–
267. doi:10.1007/bf00048075, 1991.

Liaskos, C. E., Allen, D. J., & Pickering, K. E.: Sensitivity of tropical tropospheric
composition to lightning NOx production as determined by replay simulations with
GEOS-5, J. Geophys. Res. Atmos., 120, 8512–8534, doi:10.1002/2014JD022987,
2015.

Liu, J., Jose M. Rodriguez, Luke D. Oman, Anne R. Douglass, Mark A. Olsen, Lu
Hu, Stratospheric impact on the Northern Hemisphere winter and spring ozone
interannual variability in the troposphere, Atmospheric Chemistry and Physics,
10.5194/acp-20-6417-2020, **20**, 11, 6417-6433, 2020.

Liu, X., Tai, A. P. K., and Fung, K. M.: Responses of surface ozone to future agricultural
ammonia emissions and subsequent nitrogen deposition through terrestrial ecosystem
changes, Atmos. Chem. Phys., 21, 17743–17758, https://doi.org/10.5194/acp-21-
17743-2021, 2021.

Liu, J., Strode, S. A., Liang, Q., Oman, L.D., Colarco, P. R., Fleming, E. L., et al. (2022).
Change in tropospheric ozone in the recent decades and its contribution to global total
ozone. Journal of Geophysical Research: Atmospheres, 127, e2022JD037170.
https://doi.org/10.1029/2022JD037170, 2022.

Li et al. Jianjun Qiu, Ligang Wang, Yang, L.: Advance in a terrestrial biogeochemical
model—DNDC model, Acta Ecologica Sinica, 31, 2,
https://doi.org/10.1016/j.chnaes.2010.11.006, 2011.

Luecken, D. J.; Napelenok, S. L.; Strum, M.; Scheffe, R.; Phillips, S.: Sensitivity of ambient
atmospheric formaldehyde and ozone to precursor species and source types across the
united states, Environ. Sci. Technol., 52, 4668– 4675, DOI: 10.1021/acs.est.7b05509,
2018

Marais, E. A., Jacob, D. J., Kurosu, T. P., Chance, K., Murphy, J. G., Reeves, C., Mills, G.,
Casadio, S., Millet, D. B., Barkley, M. P., Paulot, F., and Mao, J.: Isoprene emissions
in Africa inferred from OMI observations of formaldehyde columns, Atmos. Chem.
Phys., 12, 6219–6235, https://doi.org/10.5194/acp-12-6219-2012, 2012.

Marais, E. A., Jacob, D. J., Choi, S., Joiner, J., Belmonte-Rivas, M., Cohen, R. C., et al.:
Nitrogen oxides in the global upper troposphere: interpreting cloud-sliced NO_2
observations from the OMI satellite instrument, Atmospheric Chemistry and Physics,
https://doi.org/10.5194/acp-18-17017-2018, 2018

Martin, R. V., Sauvage, B., Folkins, I., Sioris, C. E., Boone, Bernath, C. P., & Ziemke, J.:
Space-based constraints on the production of nitric oxide by lightning, J. Geophys.
Res., 112, D09309, doi:10.1029/2006JD007831, 2007.

Matandirotya, N.R., Burger, R. An assessment of NO_2 atmospheric air pollution over three cities in South Africa during 2020 COVID-19 pandemic. Air Qual Atmos Health **16**, 263–276, https://doi.org/10.1007/s11869-022-01271-3, 2023.

McDuffie, E. E., Smith, S. J., O'Rourke, P., Tibrewal, K., Venkataraman, C., Marais, E. A., Zheng, B., Crippa, M., Brauer, M., and Martin, R. V.: A global anthropogenic emission inventory of atmospheric pollutants from sector- and fuel-specific sources (1970–2017): an application of the Community Emissions Data System (CEDS), Earth Syst. Sci. Data, 12, 3413–3442, https://doi.org/10.5194/essd-12-3413-2020, 2020.

Meng, L., Liu, J., Tarasick, D. W., Randel, W. J., Steiner, A. K., Wilhelmsen, H., Wang, L., and Haimberger, L.: Continuous rise of the tropopause in the Northern Hemisphere over 1980–2020. Science Advances, https://doi.org/10.1126/sciadv.abi8065, 2021.

Mills G, Pleijel H, Malley CS, Sinha B, Cooper OR, Schultz MG, Neufeld HS, Simpson D, Sharps K, Feng Z, Gerosa G, Harmens H, Kobayashi K, Saxena P, Paoletti E, Sinha V, Xu X,. Tropospheric Ozone Assessment Report: Present-day tropospheric ozone distribution and trends relevant to vegetation. Elem Sci Anth.,6(1):47. DOI: 10.1525/elementa.302, 2018.

Miyazaki, K., H. J. Eskes, K. Sudo, and Zhang, C.: Global lightning NO_x production estimated by an assimilation of multiple satellite data sets, Atmos. Chem Phys., 14, 3277–3305, doi:10.5194/acp-14-3277-2014, 2014.

Miyazaki, K., Bowman, K., Sekiya, T., Eskes, H., Boersma, F., Worden, H., Livesey, N., Payne, V. H., Sudo, K., Kanaya, Y., Takigawa, M., and Ogochi, K.: Updated tropospheric chemistry reanalysis and emission estimates, TCR-2, for 2005–2018, Earth Syst. Sci. Data, 12, 2223–2259, https://doi.org/10.5194/essd-12-2223-2020, 2020.

McPeters, R. D. and Labow, G. J.: Climatology 2011: An MLS and sonde derived ozone climatology for satellite retrieval algorithms, Journal of Geophysical Research: Atmospheres, 117, n/a-n/a, https://doi.org/10.1029/2011JD017006, 2012.

Molod, A., Takacs, L., Suarez, M., and Bacmeister, J.: Development of the GEOS-5 atmospheric general circulation model: evolution from MERRA to MERRA2, Geosci. Model Dev., 8, 1339–1356, https://doi.org/10.5194/gmd-8-1339-2015, 2015.

Murray, L.T.: An uncertain future for lightning. Nature Clim Change **8**, 191–192, https://doi.org/10.1038/s41558-018-0094-0, 2018.

Murray, L. T.: Lightning NO_x and Impacts on Air Quality, Curr Pollution Rep (2016) 2:115–133, DOI 10.1007/s40726-016-0031-7, 2016

Murray, L. T., D. J. Jacob, J. A. Logan, R. C. Hudman, and J. Koshak, W.: Optimized regional and interannual variability of lightning in a global chemical transport model constrained by LIS/OTD satellite data, J. Geophys. Res., 117, D20307, doi:10.1029/2012JD017934, 2012.

Nault, B. A., Garland, C., Wooldridge, J. L., Brune, W. H., Campuzano-Jost, P., Crounse, J. D., et al.: Observational Constraints on the Oxidation of NO_x in the Upper Troposphere, The Journal of Physical Chemistry A, 120 (9), 1468-1478, doi: 10.1021/acs.jpca.5b07824, 2016.

Nault, B. A., Laughner, J. L., Wooldridge, P. J., Crounse, J. D., Dibb, J., Diskin, et al.: Lightning NO_x emissions: reconciling measured and modeled estimates with updated NO_x chemistry. Geophysical Research Letters, 44, 9479–9488, 2017.

Newton, R., Vaughan, G., Ricketts, H. M. A., Pan, L. L., Weinheimer, A. J., and Chemel, C.: Ozonesonde profiles from the West Pacific Warm Pool: measurements and validation, Atmos Chem Phys, 16, 619–634, https://doi.org/10.5194/acp-16-619-2016, 2016.

Nielsen, J. Eric, et al. "Chemical mechanisms and their applications in the Goddard Earth Observing System (GEOS) earth system model." Journal of Advances in Modeling Earth Systems 9.8, 3019-3044, 2017.

NOAA, https://gml.noaa.gov/ccgg/trends_ch4/, 2024. Last visited: August 2nd, 2024.

Nussbaumer, C. M., Fischer, H., Lelieveld, J., and Pozzer, A.: What controls ozone sensitivity in the upper tropical troposphere?, Atmos. Chem. Phys., 23, 12651–12669, https://doi.org/10.5194/acp-23-12651-2023, 2023.

Oleribe OO, Suliman AAA, Taylor-Robinson SD, Corrah T. Possible Reasons Why Sub-Saharan Africa Experienced a Less Severe COVID-19 Pandemic in 2020. J Multidiscip Healthc. 2021;14:3267-3271, https://doi.org/10.2147/JMDH.S331847, 2021.

Oltmans, SJ, Lefohn, AS, Shadwick, D, Harris, JM, Scheel, HE, et al.: Recent tropospheric ozone changes — A pattern dominated by slow or no growth, Atmos. Environ, 2013.

Orbe, C., Oman, L. D., Strahan, S. E., Waugh, D. W., Pawson, S., Takacs, L. L., and Molod, A. M.: Large-scale atmospheric transport in GEOS replay simulations. Journal of Advances in Modeling Earth Systems, 9, 2545–2560. https://doi.org/10.1002/2017MS001053, 2017.

Ott, L. E., K. E. Pickering, G. L. Stenchikov, H. Huntrieser, and Schumann, U.: Effects of lightning NOx production during the 21 July European Lightning Nitrogen Oxides Project storm studied with a three-dimensional cloud-scale chemical transport model, J. Geophys. Res., 112, D05307, doi:10.1029/2006JD007365, 2007.

Ott, L. E., K. E. Pickering, G. L. Stenchikov, D. J. Allen, A. J. DeCaria, B. Ridley, R.-F. Lin, S. Lang, and Tao, W.-K.: Production of lightning NOx and its vertical distribution calculated from three-dimensional cloud-scale chemical transport model simulations, J. Geophys. Res., 115, D04301,doi:10.1029/2009JD011880, 2010.

Philipona, R., C. Mears, M. Fujiwara, P. Jeannet, P. Thorne, G. Bodeker, L. Haimberger, M. Hervo, C. Popp, G. Romanens, W. Steinbrecht, R. Stubi, R. Van Malderen, adiosondes show that after decades of cooling, the lower stratosphere is now warming. J. Geophys. Res. Atmos. 123, 12509–12522, 2018.

Pickering, K. E, A. M. Thompson, R. R. Dickerson, W. T. Luke, D. P. McNamara, J. P. Greenberg, and R. Zimmerman, P.: Model calculations of tropospheric ozone production potential following observed convective events, J. Geophys. Res., 95:14,049-14,062, 1990.

Pickering, K. E., Y. Wang, W.-K. Tao, C. Price, and Mueller, J.-F.: Vertical distributions of lightning NO_x for use in regional and global chemical transport models, J. Geophys. Res., 103: 31,203-31,216, 1998.

Pickering, K. E., E. Bucsela, D. Allen, A. Ring, R. Holzworth, and Krotkov, N.: Estimates of lightning NOx production based on OMI NO$_2$ observations over the Gulf of Mexico, J. Geophys. Res. Atmos., 121, doi:10.1002/2015JD024179, 2016.

Pickering, K., Y. Li, K. A. Cummings, M. Brock, D. Allen, E. C. Bruning, and B. Pollack, I.: Lightning NOx in the 29–30 May 2012 Deep Convective Clouds and Chemistry (DC3) Severe Storm and Its Downwind Chemical Consequences, J. Geophys. Res., 129, e2023JD039439., doi:10.1029/2023JD039439, 2024.

Pinto, O., Jr., K. P. Naccarato, and R. C. A. Pinto, I.: Thunderstorm incidence in southeastern Brazil estimated from different data sources. Ann. Geophys., 31, 1213–1219, https://doi.org/10.5194/angeo-31-1213-2013, 2013.

Prodromos Zanis, Dimitris Akritidis, Steven Turnock, Vaishali Naik, Sophie Szopa, Aristeidis K Georgoulias, Susanne E Bauer, Makoto Deushi, Larry W Horowitz, James Keeble, Climate change penalty and benefit on surface ozone: a global perspective based on CMIP6 earth system models, Environmental Research Letters, 17, 2, DOI: https://doi.org/10.1088/1748-9326/ac4a34, 2022.

Pollack, I. B., C. R. Homeyer, T. B. Ryerson, K. C. Aikin, J. Peischl, E. C. Apel, T. Campos, F. Flocke, R. S. Hornbrook, D. J. Knapp, et al.: Airborne quantification of upper tropospheric NOx production from lightning in deep convective storms over the United States Great Plains, J. Geophys. Res. Atmos., 121, 2002–2028, doi:10.1002/2015JD023941, 2016.

Prather, M. J. and J. Jacob, D.: A persistent imbalance in HO$_x$ and NO$_x$ photochemistry of the upper troposphere driven by deep tropical convection, Geophys. Res. Lett., 24, 3189 – 3192, 1997.

Price, C., J. Penner, and Prather, M.: NO$_x$ from lightning 1. Global distribution based on lightning physics, J. Geophys. Res., 102 (D5), 5929-5941, 1997.

Price, C. G.: Lightning Applications in Weather and Climate Research, Surv. Geophys. (2013) 34:755–767, DOI 10.1007/s10712-012-9218-7, 2013.

Putero, D., Cristofanelli, P., Chang, K.-L., Dufour, G., Beachley, G., Couret, C., Effertz, P., Jaffe, D. A., Kubistin, D., Lynch, J., Petropavlovskikh, I., Puchalski, M., Sharac, T., Sive, B. C., Steinbacher, M., Torres, C., and Cooper, O. R.: Fingerprints of the COVID-19 economic downturn and recovery on ozone anomalies at high-elevation sites in North America and western Europe, Atmos. Chem. Phys., 23, 15693–15709, https://doi.org/10.5194/acp-23-15693-2023, 2023.

Qie, K., Qie, X., & Tian, W.: Increasing trend of lightning activity in the South Asian region, Science Bulletin, 66 (1), 78-84, 2021.

Qie, K., Tian, W., Wang, W., Wu, X., Yuan, T., Tian, H., Luo, J., Zhang, R., & Want, T. Regional trends of lightning activity in the tropics and subtropics, Atmos. Res., 242, Article 104960, 10.1016/j.atmosres.2020.104960, 2020.

Randel, W. J., L. Polvani, F. Wu, D. E. Kinnison, C.-Z. Zou, C. Mears, Troposphere stratosphere temperature trends derived from satellite data compared with ensemble simulations from WACCM. J. Geophys. Res. Atmos. 122, 9651–9667, 2017.

Ravetta, F., G. Ancellet, A. Colette, and H. Schlager, H.: Long-range transport and tropospheric ozone variability in the western Mediterranean region during the

Intercontinental Transport of Ozone and Precursors (ITOP-2004) campaign, J. Geophys. Res., 112, D10S46, doi:10.1029/2006JD007724, 2007.

Ren, X., J. R. Olson, J. H. Crawford, W. H. Brune, J. Mao, R. B. Long, G. Chen, M. A. Avery, G. W. Sachse, J. D. Barrick, G. S. Diskin, L. G. Huey, Alan Fried, Ronald C. Cohen, Brian Heikes, Paul Wennberg, Hanwant B. Singh, Donald R. Blake, E. Shetter, R.: HOx Chemistry during INTEX–A 2004: Observation, Model Calculations and comparison with previous studies, J. Geophys. Res., 113, D05310, doi:10.1029/2007JD009166, 2008.

Ridley, B., Ott, L., Pickering, K., Emmons, L., Montzka, D., Weinheimer, A., et al.: Florida thunderstorms: A faucet of reactive nitrogen to the upper troposphere, J. Geophys. Res., 109 (D17), 10.1029/2004JD004769, 2004.

Romps, D. M., Seeley, J. T., Vollaro, D., & Molinar, J.: Projected increase in lightning strikes in the United States due to global warming, Science, 851-854, 2014.

Romps, D. M., Charn, A. B., Holzworth, R. H., Lawrence, W. E., Molinari, J., & Vollaro, D.: CAPE times P explains lightning over land but not the land-ocean contrast. Geophysical Research Letters, 45, 12,623–12,630, https://doi.org/10.1029/2018GL080267, 2018.

Romps, D. M.: Evaluating the future of lightning in cloud-resolving models. Geophysical Research Letters, 46, https://doi.org/10.1029/2019GL085748, 2019.

Sanap, S. D.: Global and regional variations in aerosol loading during COVID-19

imposed lockdown, Atmos. Environ., 246, https://doi.org/10.1016/j.atmosenv.2020.118132, 2021

Sauvage, B., R. V. Martin, A. van Donkelaar, and R. Ziemke, J.: Quantification of the factors controlling tropical tropospheric ozone and the South Atlantic maximum, J. Geophys. Res., 112, D11309, doi:10.1029/2006JD008008, 2007.

Saunois, M., R. Stavert, A., Poulter, B., Bousquet, P., G. Canadell, J., B. Jackson, R., A. Raymond, P., J. Dlugokencky, E., Houweling, S., K. Patra, P., Ciais, P., K. Arora, V., Bastviken, D., Bergamaschi, P., R. Blake, D., Brailsford, G., Bruhwiler, L., M. Carlson, K., Carrol, M., Castaldi, S., Chandra, N., Crevoisier, C., M. Crill, P., Covey, K., L. Curry, C., Etiope, G., Frankenberg, C., Gedney, N., I. Hegglin, M., Höglund-Isaksson, L., Hugelius, G., Ishizawa, M., Ito, A., Janssens-Maenhout, G., M. Jensen, K., Joos, F., Kleinen, T., B. Krummel, P., L. Langenfelds, R., G. Laruelle, G., Liu, L., MacHida, T., Maksyutov, S., C. McDonald, K., McNorton, J., A. Miller, P., R. Melton, J., Morino, I., Müller, J., Murguia-Flores, F., Naik, V., Niwa, Y., Noce, S., O'Doherty, S., J. Parker, R., Peng, C., Peng, S., P. Peters, G., Prigent, C., Prinn, R., Ramonet, M., Regnier, P., J. Riley, W., A. Rosentreter, J., Segers, A., J. Simpson, I., Shi, H., J. Smith, S., Paul Steele, L., F. Thornton, B., Tian, H., Tohjima, Y., N. Tubiello, F., Tsuruta, A., Viovy, N., Voulgarakis, A., S. Weber, T., Van Weele, M., R. Van Der Werf, G., F. Weiss, R., Worthy, D., Wunch, D., Yin, Y., Yoshida, Y., Zhang, W., Zhang, Z., Zhao, Y., Zheng, B., Zhu, Q., Zhu, Q., and Zhuang, Q.: The global methane budget 2000-2017, Earth Syst Sci Data, 12, https://doi.org/10.5194/essd-12-1561-2020, 2020.

Schumann, U., and Huntrieser, H.: The global lightning-induced nitrogen oxides source, Atmos. Chem. Phys., 7, 3823-3907, 2007.

Seguel, R. J., Castillo, L., Opazo, C., Rojas, N. Y., Nogueira, T., Cazorla, M., Gavidia-Calderón, M., Gallardo, L., Garreaud, R., Carrasco-Escaff, T., and Elshorbany, Y.: Changes in South American Surface Ozone Trends: Exploring the Influences of Precursors and Extreme Events, EGUsphere [preprint], https://doi.org/10.5194/egusphere-2024-328, 2024.

Sen, P.: Estimated of the regression coefficient based on Kendall's Tau. J Am Stat Assoc 39:1379-1389, 1968.

Shi, Z., H. Wang, Y. Tan, L. Li, Li, C.: Influence of aerosols on lightning activities in central eastern parts of China, Atmos Sci Lett., 21:e957, https://doi.org/10.1002/asl.957, 2020.

Sokhi, R. S., Singh, V., Querol, X., Finardi, S., Targino, A. C., Andrade, M. de F., Pavlovic, R., Garland, R. M., Massagué, J., Kong, S., Baklanov, A., Ren, L., Tarasova, O., Carmichael, G., Peuch, V. H., Anand, V., Arbilla, G., Badali, K., Beig, G., Belalcazar, L. C., Bolignano, A., Brimblecombe, P., Camacho, P., Casallas, A., Charland, J. P., Choi, J., Chourdakis, E., Coll, I., Collins, M., Cyrys, J., da Silva, C. M., Di Giosa, A. D., Di Leo, A., Ferro, C., Gavidia-Calderon, M., Gayen, A., Ginzburg, A., Godefroy, F., Gonzalez, Y. A., Guevara-Luna, M., Haque, S. M., Havenga, H., Herod, D., Hõrrak, U., Hussein, T., Ibarra, S., Jaimes, M., Kaasik, M., Khaiwal, R., Kim, J., Kousa, A., Kukkonen, J., Kulmala, M., Kuula, J., La Violette, N., Lanzani, G., Liu, X., MacDougall, S., Manseau, P. M., Marchegiani, G., McDonald, B., Mishra, S. V., Molina, L. T., Mooibroek, D., Mor, S., Moussiopoulos, N., Murena, F., Niemi, J. V., Noe, S., Nogueira, T., Norman, M., Pérez-Camaño, J. L., Petäjä, T., Piketh, S., Rathod, A., Reid, K., Retama, A., Rivera, O., Rojas, N. Y., Rojas-Quincho, J. P., San José, R., Sánchez, O., Seguel, R. J., Sillanpää, S., Su, Y., Tapper, N., Terrazas, A., Timonen, H., Toscano, D., Tsegas, G., Velders, G. J. M., Vlachokostas, C., von Schneidemesser, E., VPM, R., Yadav, R., Zalakeviciute, R., and Zavala, M.: A global observational analysis to understand changes in air quality during exceptionally low anthropogenic emission conditions, Environ Int, 157, https://doi.org/10.1016/j.envint.2021.106818, 2021.

Souri, A. H., Johnson, M. S., Wolfe, G. M., Crawford, J. H., Fried, A., Wisthaler, A., Brune, W. H., Blake, D. R., Weinheimer, A. J., Verhoelst, T., Compernolle, S., Pinardi, G., Vigouroux, C., Langerock, B., Choi, S., Lamsal, L., Zhu, L., Sun, S., Cohen, R. C., Min, K.-E., Cho, C., Philip, S., Liu, X., and Chance, K.: Characterization of errors in satellite-based HCHONO2 tropospheric column ratios with respect to chemistry, column-to-PBL translation, spatial representation, and retrieval uncertainties, Atmospheric Chemistry and Physics, 23, 1963–1986, https://doi.org/10.5194/acp-23-1963-2023, 2023.

Stauffer, R. M., Thompson, A. M., Kollonige, D., Tarasick, D., Van Malderen, R., Smit, H. G. J., Vömel, H., Morris, G., Johnson, B. J., Cullis, P., and et al.: An Examination of the Recent Stability of Ozonesonde Global Network Data, Earth and Space Science Open Archive, 48, https://doi.org/10.1002/essoar.10511590.1, 2022.

Steinbrecht, W., Claude, H., Köhler, U., and Hoinka, K. P.: Correlations between tropopause height and total ozone: Implications for long-term changes, J. Geophys. Res., 103, 19183–19192, https://doi.org/10.1029/98JD01929, 1998.

Steinbrecht, W., Kubistin, D., Plass-Dülmer, C., Davies, J., Tarasick, D. W., von der Gathen, P., et al.: COVID-19 crisis reduces free tropospheric ozone across the Northern Hemisphere. Geophysical Research Letters, 48, e2020GL091987. https://doi.org/10.1029/2020GL091987, 2021

Steiner, A. K., F. Ladst.dter, W. J. Randel, A. C. Maycock, Q. Fu, C. Claud, H. Gleisner, L. Haimberger, S. -P. Ho, P. Keckhut, T. Leblanc, C. Mears, L. M. Polvani, B. D. Santer, T. Schmidt, V. Sofieva, R. Wing, C. -Z. Zou, Observed temperature changes in the troposphere and stratosphere from 1979 to 2018. J. Climate 33, 8165–8194, 2020.

Stohl, A., Bonasoni, P., Cristofanelli, P., Collins, W., Feichter, J., Frank, A., Forster, C., Gerasopoulos, E., Gäggeler, H., James, P., Kentarchos, T., Kromp-Kolb, H., Krüger, B., Land, C., Meloen, J., Papayannis, A., Priller, A., Seibert, P., Sprenger, M., Roelofs, G. J., Scheel, H. E., Schnabel, C., Siegmund, P., Tobler, L., Trickl, T., Wernli, H., Wirth, V., Zanis, P., and Zerefos, C.: Stratosphere-troposphere exchange: A review, and what we have learned from STACCATO, J. Geophys. Res., 108, 8516, https://doi.org/10.1029/2002JD002490, 2003.

Strahan, S. E., Duncan, B. N., and Hoor, P.: Observationally derived transport diagnostics for the lowermost stratosphere and their application to the GMI chemistry and transport model. Atmospheric Chemistry and Physics, 7(9), 2435–2445. https://doi.org/10.5194/acp-7-2435-2007, 2007.

Schultz, M.G., Schröder, S., Lyapina, O., Cooper, O., Galbally, I., Petropavlovskikh, I., von Schneidemesser, E., Tanimoto, H., Elshorbany, Y., Naja, M., Seguel, R., Dauert, U., Eckhardt, P., Feigenspahn, S., Fiebig, M., Hjellbrekke, A.-G., Hong, Y.-D., Christian Kjeld, P., Koide, H., Lear, G., Tarasick, D., Ueno, M., Wallasch, M., Baumgardner, D., Chuang, M.-T., Gillett, R., Lee, M., Molloy, S., Moolla, R., Wang, T., Sharps, K., Adame, J.A., Ancellet, G., Apadula, F., Artaxo, P., Barlasina, M., Bogucka, M., Bonasoni, P., Chang, L., Colomb, A., Cuevas, E., Cupeiro, M., Degorska, A., Ding, A., Fröhlich, M., Frolova, M., Gadhavi, H., Gheusi, F., Gilge, S., Gonzalez, M.Y., Gros, V., Hamad, S.H., Helmig, D., Henriques, D., Hermansen, O., Holla, R., Huber, J., Im, U., Jaffe, D.A., Komala, N., Kubistin, D., Lam, K.-S., Laurila, T., Lee, H., Levy, I., Mazzoleni, C., Mazzoleni, L., McClure-Begley, A., Mohamad, M., Murovic, M., Navarro-Comas, M., Nicodim, F., Parrish, D., Read, K.A., Reid, N., Ries, L., Saxena, P., Schwab, J.J., Scorgie, Y., Senik, I., Simmonds, P., Sinha, V., Skorokhod, A., Spain, G., Spangl, W., Spoor, R., Springston, S.R., Steer, K., Steinbacher, M., Suharguniyawan, E., Torre, P., Trickl, T., Weili, L., Weller, R., Xu, X., Xue, L. and Zhiqiang, M., Tropospheric Ozone Assessment Report: Database and Metrics Data of Global Surface Ozone Observations, Elem Sci Anth, 5, p.58. DOI: 10.1525/elementa.244, 2017.

Szopa, S., Naik, V., Adhikary, B., Artaxo, P., Berntsen, T., Collins, W.D., Fuzzi, S., Gallardo, L., Kiendler-Scharr, A., Klimont, Z., Liao, H., Unger, N., and Zanis, P.: Short-Lived Climate Forcers. In Climate Change 2021: The Physical Science Basis. Contribution of Working Group I to the Sixth Assessment Report of the Intergovernmental Panel on Climate Change [Masson-Delmotte, V., P. Zhai, A. Pirani, S.L. Connors, C. Péan, S. Berger, N. Caud, Y. Chen, L. Goldfarb, M.I. Gomis, M. Huang, K. Leitzell, E. Lonnoy, J.B.R. Matthews, T.K. Maycock, T. Waterfield, O. Yelekçi, R. Yu, and B. Zhou (eds.)]. Cambridge University Press,

Cambridge, United Kingdom and New York, NY, USA, pp. 817–922, doi:10.1017/9781009157896.008, 2021.

Tarasick, D., Galbally, I.E., Cooper, O.R., Schultz, M.G., Ancellet, G., Leblanc, T., Wallington, T.J., Ziemke, J., Liu, X., Steinbacher, M., Staehelin, J., Vigouroux, C., Hannigan, J.W., García, O., Foret, G., Zanis, P., Weatherhead, E., Petropavlovskikh, I., Worden, H., Osman, M., Liu, J., Chang, K.-L., Gaudel, A., Lin, M., Granados-Muñoz, M., Thompson, A.M., Oltmans, S.J., Cuesta, J., Dufour, G., Thouret, V., Hassler, B., Trickl, T. and Neu, J.L., 2019. Tropospheric Ozone Assessment Report: Tropospheric ozone from 1877 to 2016, observed levels, trends and uncertainties. Tropospheric Ozone Assessment Report: Tropospheric ozone from 1877 to 2016, observed levels, trends and uncertainties. Elem Sci Anth, 7(1), p.39. DOI : 10.1525/elementa.376, 2019.

Thompson, A. M., Witte, J. C., Sterling, C., Jordan, A., Johnson, B. J., Oltmans, S. J., Fujiwara, M., Vömel, H., Allaart, M., Piters, A., Coetzee, G. J. R., Posny, F., Corrales, E., Diaz, J. A., Félix, C., Komala, N., Lai, N., Ahn Nguyen, H. T., Maata, M., Mani, F., Zainal, Z., Ogino, S., Paredes, F., Penha, T. L. B., Silva, F. R., Sallons-Mitro, S., Selkirk, H. B., Schmidlin, F. J., Stübi, R., and Thiongo, K.: First Reprocessing of Southern Hemisphere Additional Ozonesondes (SHADOZ) Ozone Profiles (1998–2016): 2. Comparisons With Satellites and Ground-Based Instruments, Journal of Geophysical Research: Atmospheres, 122, https://doi.org/10.1002/2017JD027406, 2017.

Tsivlidou, M., Sauvage, B., Barret, B., Wolff, P., Clark, H., Bennouna, Y., Blot, R., Boulanger, D., Nédélec, P., Le Flochmoën, E., and Thouret, V.: Tropical tropospheric ozone and carbon monoxide distributions: characteristics, origins and control factors, as seen by IAGOS and IASI, Atmos. Chem. Phys. Discuss. (preprint), https://doi.org/10.5194/acp-2022-686, in review, 2022.

Turnock, S. T., Allen, R. J., Andrews, M., Bauer, S. E., Deushi, M., Emmons, L., Good, P., Horowitz, L., John, J. G., Michou, M., Nabat, P., Naik, V., Neubauer, D., O'Connor, F. M., Olivié, D., Oshima, N., Schulz, M., Sellar, A., Shim, S., Takemura, T., Tilmes, S., Tsigaridis, K., Wu, T., and Zhang, J.: Historical and future changes in air pollutants from CMIP6 models, Atmos. Chem. Phys., 20, 14547–14579, https://doi.org/10.5194/acp-20-14547-2020, 2020.

Theil, H.: A rank-invariant method of linear and polynomial regression analysis. I, II, III", Nederl. Akad. Wetensch., Proc., 53: 386–392, 521–525, 1397–1412, 1950.

Trickl, T., Bärtsch-Ritter, N., Eisele, H., Furger, M., Mücke, R., Sprenger, M., and Stohl, A.: High-ozone layers in the middle and upper troposphere above Central Europe: potential import from the stratosphere along the subtropical jet stream, Atmos. Chem. Phys., 11, 9343–9366, https://doi.org/10.5194/acp-11-9343-2011, 2011.

Verma, S., Yadava, P. K., Lal, D. M., Mall, R. K., Harshbardhan, K., & Payra, S.: Role of Lightning NO_x in ozone formation: A review, Pure and Applied Geophysics, 178, 1425-1443, 2021.

Wang, H., Shi, Z., Wang, X., Tan, Y., Wang, H., Li, L., & Lin, X.: Cloud-to-Ground Lightning Response to Aerosol over Air-Polluted Urban Areas in China. Remote Sens. 13, 2600. https://doi.org/10.3390/rs13132600, 2021

Wang, H., Lu, X., Jacob, D. J., Cooper, O. R., Chang, K.-L., Li, K., Gao, M., Liu, Y., Sheng, B., Wu, K., Wu, T., Zhang, J., Sauvage, B., Nédélec, P., Blot, R., and Fan, S.: Global tropospheric ozone trends, attributions, and radiative impacts in 1995–2017: an integrated analysis using aircraft (IAGOS) observations, ozonesonde, and multi-decadal chemical model simulations, Atmos Chem Phys, 22, 13753–13782, https://doi.org/10.5194/acp-22-13753-2022, 2022.

Wang, Y., A. W. DeSilva, G. C. Goldenbaum, and R Dickerson, R.: Nitric oxide production by simulated lightning: Dependence on current, energy, and pressure, J. Geophys. Res., 103, 19,149-19,159, 1998.

Wilcox, R.: Fundamentals of Modern Statistical Methods: Substantially Improving Power and Accuracy. Springer Science and Business Media, 2001.

Williams, R. S., Hegglin, M. I., Kerridge, B. J., Jöckel, P., Latter, B. G., and Plummer, D. A.: Characterising the seasonal and geographical variability in tropospheric ozone, stratospheric influence and recent changes, Atmos. Chem. Phys., 19, 3589–3620, https://doi.org/10.5194/acp-19-3589-2019, 2019.

Wu, D., Zhang, J., Wang, M., An, J., Wang, R., Haider, H., et al.: Global and regional patterns of soil nitrous acid emissions and their acceleration of rural photochemical reactions. Journal of Geophysical Research: Atmospheres, 127, e2021JD036379. https://doi.org/10.1029/2021JD036379, 2022.

WMO: International Meteorological Vocabulary (2nd ed.), Geneva: Secretariat of the World Meteorological Organization. 1992. p. 636. ISBN 978-92-63-02182-3, 1992

Wang and Chen, A review on parameterization and uncertainty in modeling greenhouse gas emissions from soil, Geoderma,: https://doi.org/10.1016/j.geoderma.2011.11.009, 2012.

Xue, X., Ren, G. Y., Xu, X. D., Sun, X. B., Yang, G. W., Zhang, P. F., & Zhang, S. Q.: The trends of warm-season thunderstorm and lightning days in China and the influence of environmental factors, J. Geophys. Res., 126 (15), 10.1029/2021JD034950, 2021.

Yang, X., and Li, Z.: Increases in thunderstorm activity and relationships with air pollution in southeast China, J. Geophys. Res. Atmos., 119, 1835–1844, doi:10.1002/2013JD021224, 2014.

Yang et al.: Photochemical emissions of HONO, NO2 and NO from the soil surface under simulated sunlight, Atmospheric Environment, https://doi.org/10.1016/j.atmosenv.2020.117596, 2020.

Yetong Li, Yan Xia, Fei Xie, Yingying Yan, Influence of stratosphere-troposphere exchange on long-term trends of surface ozone in CMIP6, Atmospheric Research, 297, doi: https://doi.org/10.1016/j.atmosres.2023.107086, 2024.

Yin, Y., Chevallier, F., Ciais, P., Broquet, G., Fortems-Cheiney, A., Pison, I., and Saunois, M.: Decadal trends in global CO emissions as seen by MOPITT, Atmos. Chem. Phys., 15, 13433–13451, https://doi.org/10.5194/acp-15-13433-2015, 2015.

Young, P.J., Naik, V., Fiore, A.M., Gaudel, A., Guo, J., Lin, M.Y., Neu, J.L., Parrish, D.D., Rieder, H.E., Schnell, J.L., Tilmes, S., Wild, O., Zhang, L., Ziemke, J.R., Brandt, J., Delcloo, A., Doherty, R.M., Geels, C., Hegglin, M.I., Hu, L., Im, U., Kumar, R., Luhar, A., Murray, L., Plummer, D., Rodriguez, J., Saiz-Lopez, A., Schultz, M.G.,

2027   Woodhouse, M.T. and Zeng, G. Tropospheric Ozone Assessment Report: Assessment
2028   of global-scale model performance for global and regional ozone distributions,
2029   variability, and trends, Elem Sci Anth, 6(1), p.10. DOI: 10.1525/elementa.265, 2018.

2030   Zeng, G., Morgenstern, O., Braesicke, P., Pyle, J.A.: Impact of stratospheric ozone recovery
2031   on tropospheric ozone and its budget: impact of ozone recovery on tropospheric
2032   ozone. Geophys. Res. Lett. 37, n/a-n/a. https://doi.org/10.1029/ 2010GL042812,
2033   2010.

2034   Zhang, X., Yin, Y., van der A, R., Lapierre, J. L., Chen, Q., Kuang, X., Yan, S., Chen, J., He,
2035   C., and Shi, R.: Estimates of lightning NO_x production based on high-resolution OMI
2036 NO_2 retrievals over the continental US, Atmos. Meas. Tech., 13, 1709–1734,
2037   https://doi.org/10.5194/amt-13-1709-2020, 2020 .

2038   Zhang, L., T. Wang, Q. Zhang, J. Zheng, Z. Xu, and Lv, M.: Potential sources of nitrous acid
2039   (HONO) and their impacts on ozone: A WRF-Chem study in a polluted subtropical
2040   region, J. Geophys. Res. Atmos., 121, 3645–3662, doi:10.1002/2015JD024468, 2016.

2041   Zheng, B.; Chevallier, F.; Yin, Y.; Ciais, P.; Fortems-Cheiney, A.; Deeter, M.N.; Parker,
2042   R.J.; Wang, Y.; Worden, H.M.; Zhao, Y. Global atmospheric carbon monoxide
2043   budget 2000-2017 inferred from multi-species atmospheric inversions. Earth Sys. Sci.
2044   Data, 11, 1411–1436, https://doi.org/10.5194/essd-11-1411-2019, 2019.